Jagiellonian University

Faculty of Physics, Astronomy and Applied Computer Science

Nonuniform condensates in the phase diagram of the strongly interacting matter

Tomasz L. Partyka

PhD thesis prepared under the supervision of
dr hab. Mariusz Sadzikowski
in the Particle Theory Department

— Kraków, 2011 —

Acknowledgments

I would like to express worm gratitude to my Supervisor. His commitment, support and scientific inspiration, through all these years, made the thesis possible.

Contents

Chapter 1

Introduction

The phase diagram of the strongly interacting matter is one of the central subjects in modern physics. The aim of exploring the phase structure of the strongly interacting matter is to determine how is the matter organized under extreme conditions. At a distance scale of the order of femtometer, the dominant interaction is the strong force, and the theory describing strong interactions is the Quantum Chromodynamics (QCD). Extreme energy densities, corresponding to the femtometer distance scale, can be achieved by increasing either the temperature or baryon density. Therefore, these two quantities span the space of the QCD phase diagram. Studying of the properties of matter, at such high baryon densities and temperatures, is not only a pure academic discussion. On this basis, one can reveal the history of evolution of the Universe or describe the structure of the neutron star core.

Since the very beginning of the QCD era, both theoretical and experimental efforts have been taken to explore the phase structure of matter under extreme conditions. Until today, the best investigated part of the phase diagram of the strongly interacting matter, is the region of zero baryon density and high temperature. At this region, lattice QCD computations give most of the results. As QCD becomes weakly coupled, zero baryon density - high temperature region, can be treated by the perturbative QCD calculations. At the same time, this part of the strongly interacting matter phase diagram, is well explored by the ultra-relativistic heavy ion colisions. On the other hand, at asymptoticly high baryon density - zero temperature region, direct weak-coupling calculations allow the understanding of properties of the strongly interacting matter. In this part of the QCD phase diagram, the ground state of the system is expected to be the so-called color flavor locked (CFL) phase of color superconductivity. However, this QCD limit is beyond the man-made laboratories.

None of the above treatments can be adopted in the baryon density range of the order of several times nuclear matter density. Lattice simulations suffer from the famous sign problem. At non-zero baryon chemical potential fermion determinant gets complex and straightforward Monte Carlo sampling loses its effectiveness. Simultaneously, QCD coupling constant leaves perturbative regime, and weak-coupling methods are not possible. As a result, the region of moderate densities and temperatures is the less known part of

the QCD phase diagram. Nontheless, there is an expectation that this intermediate region can reveal us some essential phenomena. Most of all, existence of many different phases is expected. Among those, the Larkin-Ovchinnikov-Fulde-Ferrell phase of color superconductivity or spatially nonunifrom chiral condensate, are very good examples. Secondly, transitions from the hadronic to chirally symmetric and from the confined to deconfined phases of matter, are presumably separated in this area. It is thus important to understand the relationship between these two transitions.

Our current theoretical approach to the moderate baryon density range of the QCD phase diagram is based on the interplay between the general arguments and the effective model calculations. Extrapolation of the QCD results in the large number of colors or asymptotic density limits may also shed light on this part of the QCD phase diagram. Among the effective models, the Nambu Jona-Lasinio (NJL) theory is the widely accepted and mostly used in the analysis of the phase diagram. It describes the spontaneous brake down of chiral symmetry and enables us to study the competition between the chiral and diquark condensates. However, the NJL model has a clear deficiency. In this model, the non-local color current interaction is reduced to the point like interaction with an effective coupling constant. As a consequence, the effect of color confinement is beyond the NJL model description. In order to describe both the spontaneous breakdown of chiral symmetry and color confinement, the Polyakov loop extended NJL (PNJL) model was proposed as an extension of the original NJL theory. In the PNJL model, the background gluon field is introduced, and the expectation value of the Polyakov loop can be an indicator of a transition from the confined into the deconfined phases of matter.

From the experimental perspective, the phase diagram of the strongly interacting matter is still insufficiently explored. On the one hand, the strong evidence of the onset of deconfinement, that have been observed at the RHIC and CERN SPS, is the long-awaited confirmation of the deconfined quark-gluon matter. The another promising result of the heavy-ion collision experiments is the chemical freeze-out curve, that is the primary landmark for mapping the QCD phase diagram. But on the other hand, the lack of a direct experimental data in the moderate baryon density region is an obvious difficulty. This is so, because exploration of the moderate baryon densities region corresponds to the collisions of heavy ions with energies lower than those planned for the RHIC or the LHC. Hopefully, the near coming progress in the experimental knowledge is expected. Two experiments designated to cover the region of the QCD phase diagram where the critical point is presumably located are already in progress. These are the NA61/SHINE at SPS and the Beam Energy Scan at RHIC. The Compressed Baryonic Matter experiment at FAIR and the future NICA/MPD project at JINR will also investigate the highly compressed nuclear matter.

In this thesis we focus on the concept of the spatially nonuniform chiral condensate. As moderate density region of the QCD phase diagram is unaccessible with *ab initio* calculations, inhomogeneous phase is usually studied within effective models. We use the Nambu Jona-Lasinio and Polyakov NJL models. Results of the effective models are subjected to uncertainties, exemplarily due to the choice of parameters. This observation became the one motivation of our study. We ask the technical but important question of

how does the QCD phase diagram is affected by the fine details of the NJL and PNJL models. The another motivation is to extend our analysis on some physical effects that definitely influence the inhomogeneous chiral phase. We discuss the effects due to the non-zero bare mass of quark, we also point out on the dependence of the effective four-quark coupling with temperature.

The outline of this work is organized as follows:

In chapter 2 we provide an introductory overview of the issue of the strongly interacting matter phase diagram. In this context we point out the role of existence of the spatially inhomogeneous chiral condensate.

In chapter 3 the dependence of the NJL model results with respect to the different regularization schemes is discussed. The influence of the 2SC color superconducting phase is also considered in this analysis. Calculations were done at zero temperature and in the chiral limit.

In chapter 4 we study the influence of the non-zero current quark mass on the spatially nonuniform chiral condensate. Within the framework of the NJL model, the first order correction to the grand thermodynamic potential, due to the non-zero quark current mass, is evaluated. The role of the 2SC color superconducting phase is also considered, and the results are presented both for the 3d cut-off and Schwinger regularization schemes.

In chapter 5 within the framework of the Polyakov loop extended NJL theory, the phase structure of the strongly interacting matter in the temperature - baryon density plane is investigated. It is shown that existence of the spatially inhomogeneous ground state is consistent with the PNJL model at the mean field level. Conclusion is that the nonuniform chiral phase can be interpreted as a special realization of a so-called quarkyonic matter.

Chapter 2

Phase diagram of the strongly interacting matter

2.1 Phase diagram overview

The matter under external conditions, such as temperature or pressure, can exist in different phases. These various phases of matter, differ with each other by physical properties and internal symmetries. Depending on the distance scale at which we examine the organization of matter, different interactions turn out to be crucial for understanding of matter properties. At the astrophysical scale, it is the gravitational force that captures matter into the planets and stars and determines their motion. At the everyday life scale and below, until the atomic scale, the electromagnetic interaction binds atoms and forms intermolecular bonds. We are familiar with the condensed matter phase diagrams, on which, regions where matter exhibits various states are marked by a phase coexistence lines. However, at sufficiently high temperature, any substance undergoes a transition into a state called plasma. In the plasma, molecules dissociate to form a gas of individual ions and electrons.

By an analogy, the natural question arises, what happens if the temperature will continue to grow. One of the first who addressed this problem was Rolph Hagedorn. He came to a conclusion of the existence of the limiting temperature [1]. With the framework of the statistical bootstrap model, Hagedorn concluded, that with growing energy of a system, this is the number of particles that increases, but the temperature becomes constant. Soon after, Hagedorn paradox was resolved. People realized that hadrons have internal structure built up from point-like quarks and gluons [2]. At this scale, the dominant interaction is the color force. With the onset of the QCD era, the existence of a new state of matter, the quark-gluon plasma, was postulated. Nevertheless, the concept of limiting temperature remained as an estimation of the transition temperature to the quark-gluon plasma. Moreover, exponential growth of the number of hadronic states with mass, predicted by Hagedorn, is confirmed by the experimental data [3]. At that time people understood, that squeezing of matter leads to a similar effect. At sufficiently high densities, individual nucleons begin to overlap losing their individuality. Again, the

dominant degrees of freedom becomes quarks, and the dominant force becomes the strong interaction. But yet, this limit is not the same with raising the temperature at zero baryon density. Nucleons exhibit repulsive force at short distances what makes the difference [4].

The history of the phase diagram of the strongly interacting matter dates back to those days. The very first conceptual phase diagram was sketched by Cabibbo and Parisi in 1975 [5]. On those diagram, the hadron sector was separated from the quark-gluon sector by the second order transition curve. With time, the understanding of the phase diagram improved. At first, people began to consider the possibility that the so-called deconfinement transition can exhibit different properties depending on the baryon density. Baym argumented that at densities above the nuclear matter density, deconfinement transition is of the first order. While, at higher temperatures and smaller densities limit, it is of the second order. Further, the question arose about the relationship between the deconfinement transition and the moment of chiral symmetry restoration. In Ref. [6] the more elaborated form of the the phase diagram of the strongly interacting matter appeared (Fig.2.1). In this diagram. deconfinement transition always precedes the chiral symmetry restoration. Another novel phenomenon in Fig.2.1 is the existence of the pion condensation.

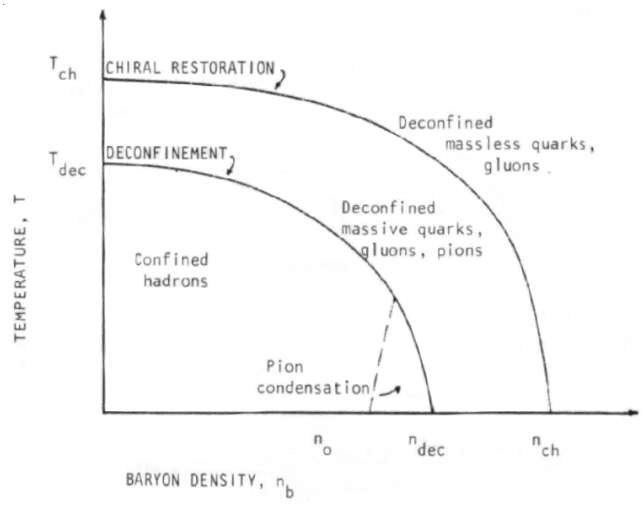

Figure 2.1: The phase diagram of the strongly interacting matter in the temperature - baryon density plane, taken from Ref. [6].

Afterwards, early lattice QCD simulations indicated that both transitions coincide, at least, at zero baryon density [7]. Also at that time, the another characteristic property of the QCD phase diagram was postulated. At a sufficiently high baryon density and low temperature quarks are expected to form a Fermi liquid. With an analogy to the Cooper pairing of electrons, the pairing between quarks is possible [8]. Since the color superconducting gap was estimated to be of the order of 10-100 MeV [9, 10], this phase of the quark matter became compelling. Only recently, presented above and historically established division of the phase diagram, has been disturbed. McLerran and Pisarski postulated existence of a so-called quarkyonic matter [11]. At high baryon densities the

Fermi sea of quarks is well formed, but at the same time, color is confined and excitations above the Fermi level are of the colorless baryons. This is the characteristic property of this novel phase of matter.

Still conjectured, but most updated form of the QCD phase diagram, is shown in Fig. 2.2.

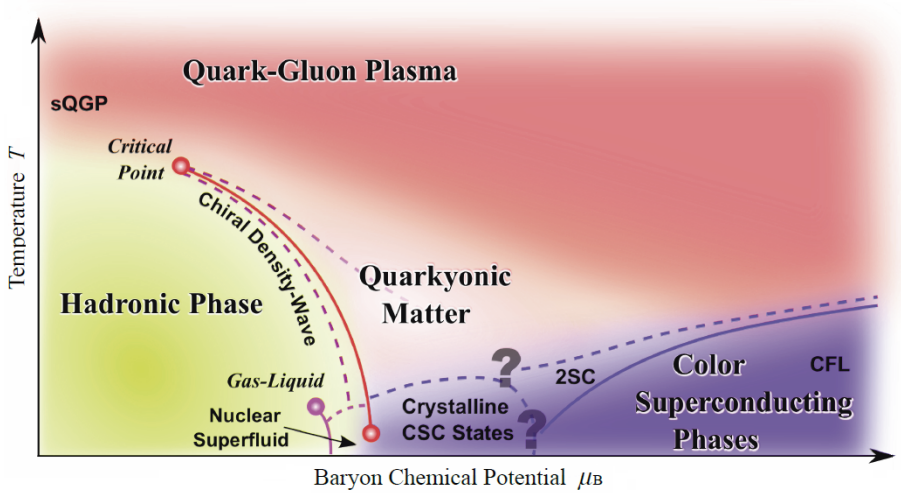

Figure 2.2: The conjectured phase diagram of QCD; Figure is taken from Ref. [12].

2.2 Moderate density region

In the context of the present study, the most relevant region of the QCD phase diagram, is the regime of moderate densities and low temperatures. By the term "moderate density" we refer to the region of baryon density of the order of several times larger than nuclear density $\rho_0 \approx 0.16/fm^3$. This estimation comes from the fact, that transition from the nuclear into the quark matter phase is expected to occur when baryons begin to overlap. The critical baryon density resulting from the model of percolation of (hard-core) spheres is $\rho_{QM} \approx 0.93/fm^3$ [13]. Baryon chemical potential corresponding to this transition can be calculated within different models what give $\mu_B \sim 1100 - 1500\,\mathrm{MeV}$ [14].

The moderate density region is interesting because this is the only part of the strongly interacting matter phase diagram (apart from the nuclear matter) that probably finds its realization in nature, in compact stars. Although the early Universe passed through the quark matter phase, but the question is, whether today one can observe any signs of this early stage of the Universe evolution. In contrary, neutron stars are the well known and intensively studied objects. The basic observation for the neutron star is their frequency of rotation. One can also measure the mass and the spectrum of thermal radiation. The process of cooling of the neutron star is also affected by the quark matter core (e.g. [15]).

If one incorporates the properties of the quark matter into the compact star description, astrophysical observations can verify such a model. Until today, astrophysical data are not sufficient to discriminate between the nuclear and the quark matter models. As mentioned previously, the novel heavy ion collision experiments would provide us with the improved insight into the physics of this part of the QCD phase diagram. However, these experiments are planned to cover the temperature range of order tens MeV, while temperature inside the compact star is below 1 MeV. Consequently, direct verification of the zero temperature predictions can only be achieved by the astrophysical observations.

As *ab initio* calculations are limited, one has to rely on the phenomenological models and general arguments. In particular, the high symmetry groups involved in the description of strong interactions, suggest the existence of many types of phases in the moderate density region. Analysis of the QCD in the large number of colors or asymptotic density limits can also be a hint towards the moderate density region. By such argumentation, the two important phenomena was postulated. These are the color superconductivity and the chiral density waves.

2.3 Color superconductivity

The phenomenon of color superconductivity was originally predicted at infinite baryon density. At this limit, QCD coupling becomes weak and quark matter can be described as a Fermi liquid. Asymptotically free quarks pair together at the edge of a Fermi surface. Consequently, the standard Bardeen-Cooper-Schrieffer (BCS) [16] mechanism leads to the formation of a diquark condensate. We recall that unlike superconductivity in metals, attractive interaction between quarks is a fundamental property of the color force. At asymptotic baryon densities, where one gluon-exchange dominates, quarks pair in a so-called color flavor locked (CFL) pattern [9]. Color and chiral symmetries are broken to the diagonal subgroup $SU(3)_{c+V}$ and the CFL phase is invariant under the synchronous color and vector transformations. The above reasoning changes at moderate density region. The reason is that the split between the Fermi surfaces of different quark flavors is getting more distinctive. BCS condensation is energetically favoreable until this difference is smaller than the value of superconducting gap. The current mass of the strange quark is of the order of magnitude higher than masses of quarks u and d. Due to this fact, the new pattern of condensation arises. In this so-called 2SC (two flavor color superconductivity) phase, only the two light quarks participate in condensation, leaving the strange quark unpaired. 2SC channel is asymmetric in the color and flavor spaces and is a spin singlet state. The 2SC scalar diquark condensate can be descreibed as below [17]

$$< \Psi_i^\alpha C\gamma_5 \Psi_j^\beta > \sim \Delta_{2SC}\epsilon_{ij3}\epsilon^{\alpha\beta 3}$$

where C is the charge conjugation matrix, Δ_{2SC} is the superconducting gap, and α, i refer to the color and flavor indices respectively. In the present study we discuss the phenomenologically relevant densities, and so, we consider only the 2SC pattern of color superconductivity.

2.4 Chiral density waves

Chiral symmetry is broken by the non-zero vacuum expectation value of the quark-antiquark pair. Restoration of the chiral symmetry happens when a quark chemical potential exceed the value of the constituent quark mass. At such density, the Fermi sea of quarks is formed. The energy cost needed to excite the quark-antiquark pair is higher than the binding energy of such a pair. This is the standard scenario of the phase diagram of the strongly interacting matter at zero temperature.

In the presence of the Fermi sea, the chiral symmetry can be broken by a quark-quark hole excitation. The particle-hole pairs from the opposite sites of the Fermi surface create a condensate with the non-zero total momentum. The mechanism that may leads to the existence of such a standing chiral density wave is in close analogy with the solid-state physics phenomena. The one is the so-called Peierles instability, mechanism which leads to the standing density wave of charge (CDW) [18, 19]. The ground state of the low-dimensional metals is unstable against the creation of a periodic modulation of a charge density in the conduction band. Due to the electron phonon interaction, this is accompanied by the distortion of ions in the lattice. As a result, the energy gap emerges, and effectively the energy of electrons is lowered. The stability of such a ground state depends on the relation between the gain of the electron kinetic energy, and the energy cost needed for the lattice distortion. Similar mechanism may lead to the existence of the standing density wave of spins (SDW) [20, 21, 22]. Electrons with opposite spins create two charge density waves out of phase. The total charge density is uniform, but the magnetization changes periodically. The kinetic energy of electrons is lowered again due to the emergence of the energy gap, and Coulomb repulsion between electrons generates energy loss. In general, standing density waves are typical for the one dimensional systems. The specific shape of the Fermi surface causes that many electron-hole pairs from the opposite sides of the Fermi surface can be excited. The total momentum of such a pair is equal $2k_F$ (k_F Fermi momentum). For the higher dimensional systems, the existence of density waves is less probable.

In the context of the quark matter, the instability of the Fermi surface leading to the chiral density waves was postulated in the large number of colors limit [23]. The periodic spatial modulation of the quark condensate was investigated. In the $N_c \to \infty$ limit, and at high baryon density, chiral density wave ground state turn to be favored over the CFL condensate. However, analysis for the large, but finite N_c, proved that the region of the above mentioned instability is restricted to the finite interval of baryon chemical potential [24].

In the present study, we want to focus on the so-called dual standing chiral density waves [25, 26, 27]. Both chiral condensate in the scalar and pseudo scalar channels undergo spatial modulation with the wave vector $\vec{q}$

$$\langle \bar{\psi}\psi \rangle \sim \cos(\vec{q}\cdot\vec{x}), \quad \langle \bar{\psi} i\gamma_5 \tau^a \psi \rangle \sim \sin(\vec{q}\cdot\vec{x}),$$

but the magnitude of the chiral condensate is spatially uniform. The same field configuration correspond to the inhomogeneous pion condensate within the Quark Meson model

[28, 29, 34, 35]. The stability of the dual chiral density wave (DCDW) ground state is also governed by the two competitive processes. On the one hand, the energy spectrum is modified due to the presence of the DCDW. Quark spectrum separates into the two branches

$$E_{\pm} = \sqrt{\vec{k}^2 + M^2 + \frac{\vec{q}^{\,2}}{4} \pm \sqrt{(\vec{q}\cdot\vec{k})^2 + M^2\,\vec{q}^{\,2}}}\,.$$

Deformation of the Fermi surface due to the density wave with the vector $\vec{q}$ of order $2k_F$ is energetically favourable. On the other hand, the vacuum contribution to the free energy of the system is modified by an additional positive term proportional to $f_\pi^2\vec{q}^{\,2}$ (f_π pion decay constatnt). Within the QM model, this term has a clear interpretation as a kinetic energy of the meson fields [29]. These two processes determine whether the DCDW is likely to appear. Finally, the question arises, if one can experimentally verify the existence of the chiral density waves in quark matter. The one experimental hint is, that in the presence of the dual chiral density waves, the system possesses the non-zero total magnetization [35, 36]. Consequently, the observable strong magnetic field of the compact stars can presumably originate in the properties of the inhomogeneous quark matter.

2.5 Nambu Jona-Lasinio model

The fundamental theory which describes strong interactions between the elementary constituents of matter, quarks and gluons, is the Quantum Chromodynamics (QCD). In the large momentum or equivalently small distance scale regimes, because of the asymptotic freedom, the strong coupling constant becomes small and the complete mathematical techniques of perturbative calculations can be applied. However, as mentioned earlier, at moderate baryon densities region, the strong coupling constant remains large. Lagrangian density is well defined, but one can not solve the QCD to gain interesting information. The need of formulation of a mathematically less complicated effective model of strong interactions is clear. Such simplified theory should still preserve the most relevant properties of the QCD. The complexity of QCD equations originates in the nonabelian gauge group that governs the strong interactions. In the hadronic sector, one can approximate the non-local color current interaction by the point like four fermion vertex with the effective coupling constant [30]

$$\mathcal{L}_{int} = -g_c(\overline{\psi}\gamma_\mu\lambda^A\psi)^2.$$

Due to this simplification, the original local color symmetry is replaced by the global $SU(3)_c$ color symmetry and the phenomenon of color confinement can not be described. Here is the starting point of the Nambu Jona-Lasinio (NJL) type theories (however, we recall that the NJL model was originally developed as a theory of nucleons [31, 32]). Fierz transformation of the above color current interaction produces a set of interaction terms, both in the quark-antiquark and quark-quark channels. In this work, we do not consider

the all possible channels, but restrict to the scalar, pseudoscalar mesons, and scalar diquarks. The NJL Lagrangian in its relevant form is given by a formula [33]

$$\mathcal{L}_{NJL} = \overline{\psi}(i\gamma^{\nu}\partial_{\nu} - m)\psi + G\left[(\overline{\psi}\psi)^2 + (\overline{\psi}i\gamma_5\vec{\tau}\psi)^2\right] + G'[(i\overline{\psi}_C\gamma_5\tau_2\lambda^A\psi)(i\overline{\psi}\gamma_5\tau_2\lambda^A\psi_C)],$$

where ψ is the quark field, the vector $\vec{\tau}$ is the isospin vector of Pauli matrices. The effective coupling constant G describes the interaction that is responsible for the creation of a quark-antiquark condensate, G' describes the interaction that is responsible for the creation of a diquark condensate. The NJL model was constructed to preserve the fundamental symmetries that are observed in nature, and that are symmetries of the QCD Lagrangian. In its two flavor version, the overall symmetry group of the NJL model is $\mathrm{SU}(3)_c \otimes \mathrm{SU}_V(2) \otimes \mathrm{SU}_A(2) \otimes \mathrm{U}_V(1)$. Spontaneous breakdown of the $\mathrm{SU}_A(2)$ axial vector symmetry generates the constituent quark mass and give the meson π triplet.

Chapter 3

Nonuniform chiral condensate at zero temperature in different regularization schemes

In this chapter we ask a technical but important question of the regularization dependence of the phase diagram of strongly interacting matter, which contains the nonuniform chiral condensate. Our calculations are based on the NJL model at zero temperature limit. NJL local coupling constant G has a dimension MeV^{-2}, and thus, the NJL model is an effective non-renormalizable theory. In this approach, different regularization schemes define different models. Thereby, it is important to check if the results are qualitatively independent of the choice of regulator, and what is their dependence at the quantitative level. Similar analysis was performed in the case of a single nonuniform chiral phase in Ref. [34].

Most of the results presented in this chapter have been published in Ref. [48].

3.1 Regularization of the Nambu Joan-Lasinio model

The prior question that emerges is whether any of possible regularization schemes is especially dedicated to the Nambu Joan-Lasinio model. Firstly, the physical restriction we impose on regulator is that minimization of regularized total energy should give rise to the gap equation [33]. We do not explicitly check this restriction, but, it is confirmed by numerical results for the all discussed methods. Secondly, we examine spatially nonuniform phase. Thereby, the quasi-particle spectrum is anisotropic. In turn, the regularizator determines the upper energy limit of applicability of a given theory. Consequently, some authors claim [26, 37] that the intuitive 3d cut-off regularization is not appropriate in the above context. 3d cut-off procedure restricts the value of three dimensional momentum to the uniform sphere $\vec{k}^2 \leq \Lambda$. They suggest, that Schwinger (proper time) scheme is more relevant, as it effectively restricts energy spectrum - not momenta. However, revealing further results of our analysis, in the Schwinger scheme, the another problems appear.

For instance, quark constituent mass in the proper time scheme is equal only 200 MeV, which is below the phenomenologically expected value of around 300 MeV. Therefore, we decided to check the phase diagram against both the 3d cut-off and Schwinger scheme. To extend our analysis we examine also the two other regularizations: 4d cut-off (four momentum cut-off in Euclidean space) and Pauli-Villars (PV).

We consider the phase diagram at finite density, which includes the chiral uniform (Ch), chiral nonuniform (NCh), 2SC color superconducting phase and the plasma of free quarks [38]. Grand thermodynamic potential of the NJL model, at zero temperature limit, has a form [38, 39]

$$\Omega_0 = \frac{M^2}{4G} + \frac{|\Delta|^2}{4G'} + 2\sum_{s=\pm}\int_{E_s\leq\mu}\frac{d^3k}{(2\pi)^3}(E_s-\mu) - 2\sum_{s=\pm}\int\frac{d^3k}{(2\pi)^3}\left(E_s+\sum_{i=\pm}E^{\Delta}_{i,s}\right), \tag{3.1.1}$$

where

$$E^{\Delta}_{\pm,s} = \sqrt{(\mu\pm E_s)^2+|\Delta|^2},\;\; E_{\pm} = \sqrt{\vec{k}^2+M^2+\frac{\vec{q}^{\,2}}{4}\pm\sqrt{(\vec{q}\cdot\vec{k})^2+M^2\vec{q}^{\,2}}}\,. \tag{3.1.2}$$

The last integral in equation (3.1.1) is divergent. Before we introduce different regularization schemes, let us convert this equation into another form, which much better suits our purposes and better underlines the physics of the problem. To reach our goal we translate equation (3.1.1) into the new form

$$\begin{aligned}\Omega_0 &= \frac{M^2}{4G}+\frac{|\Delta|^2}{4G'} - 2\sum_{s=\pm}\sum_{i=\pm}\int\frac{d^3k}{(2\pi)^3}\left[\left(E^{\Delta}_{i,s}-E^{\Delta}_{i,0}\right)+\left(E^{\Delta=0}_{i,0}-E_s\right)\right]\\ &+ 2\sum_{s=\pm}\int_{E_s\leq\mu}\frac{d^3k}{(2\pi)^3}(E_s-\mu) - 4\sum_{i=\pm}\int\frac{d^3k}{(2\pi)^3}\left(E^{\Delta}_{i,0}-E^{\Delta=0}_{i,0}\right)\\ &- 6\sum_{s=\pm}\int\frac{d^3k}{(2\pi)^3}E_s\,,\end{aligned} \tag{3.1.3}$$

where

$$E^{\Delta}_{\pm,0} = \sqrt{(\mu\pm E_0)^2+|\Delta|^2},\;\; E_0=\sqrt{\vec{k}^2+M^2}\,. \tag{3.1.4}$$

The first two integrals (3.1.3) give finite contributions and only the last two are divergent. Let us note that in the absence of the color superconducting state the next to the last term vanishes and the only divergent contribution follows from the infinite Dirac sea integral. Additionally the last two integrals depend, the first one on Δ and the other one on wave vector $\vec{q}$ only. This separation is very convenient for the regularization procedure.

In the next step we expand the last term of equation (3.1.3) in powers of the wave vector $\vec{q}$. It is known that the parameter at the second order is related to the pion decay constant f_π [28, 29, 35, 40]

$$-6\sum_{s=\pm}\int\frac{d^3k}{(2\pi)^3}E_s \approx -12\int\frac{d^3k}{(2\pi)^3}E_0+\frac{M^2f_\pi^2\,\vec{q}^{\,2}}{2M_0^2}\,, \tag{3.1.5}$$

where M_0 is the constituent quark mass at zero density. The formula for the pion decay constant depends on the regularization and is known from the earlier literature (e.g. [33]).

Finally, the extracted divergent contribution to the thermodynamic potential Ω_0 (3.1.3) is of the form

$$\Omega_{div}=-4\sum_{i=\pm}\int\frac{d^3k}{(2\pi)^3}\left(E_{i,0}^{\Delta}-E_{i,0}^{\Delta=0}\right)-12\int\frac{d^3k}{(2\pi)^3}E_0\,. \tag{3.1.6}$$

3.1.1 Divergent contribution in different regularizations

3.1.1.1 3d cut-off regularization

In this scheme, cut-off parameter Λ restricts the value of three dimensional momentum ($\vec{k}^{\,2}\leq\Lambda$). The regularized contribution takes the form

$$\Omega_{div}^{3d}=-4\sum_{i=\pm}\int^{\Lambda}\frac{d^3k}{(2\pi)^3}\left(E_{i,0}^{\Delta}-E_{i,0}^{\Delta=0}\right)-12\int^{\Lambda}\frac{d^3k}{(2\pi)^3}E_0\,. \tag{3.1.7}$$

3.1.1.2 4d cut-off regularization

In this scheme, cut-off parameter Λ restricts the value of four-momentum in Euclidean space ($k_E^2=\vec{k}^{\,2}+k_4^2\leq\Lambda$). Using the auxiliary formula that holds for $A,B\in\Re$

$$|A|-|B|=\int\frac{dk_4}{2\pi}\ln\frac{k_4^2+A^2}{k_4^2+B^2} \tag{3.1.8}$$

we replace the integrals over three-momentum by these over four-momentum, and regularized contribution takes the form

$$\Omega_{div}^{4d}=-8\int^{\Lambda}\frac{d^4k_E}{(2\pi)^4}\ln\frac{k_4^2+\frac{1}{4}(\sum_{i=\pm}E_{i,0}^{\Delta})^2}{k_4^2+\frac{1}{4}(\sum_{i=\pm}E_{i,0}^{\Delta=0})^2}-12\int^{\Lambda}\frac{d^4k_E}{(2\pi)^4}\ln(k_4^2+E_0^2)\,, \tag{3.1.9}$$

where $d^4k_E=dk_4d^3k$.

3.1.1.3 Schwinger regularization

In this scheme, the cut-off parameter Λ restricts the value of proper time ($\tau\geq1/\Lambda^2$). We base on the representation of divergent contributions in the form of logarithms and use the formula for $A,B\in\Re^+$

$$\ln\frac{A}{B}=\int_0^{\infty}\frac{d\tau}{\tau}[\exp(-\tau\,B)-\exp(-\tau\,A)]\,. \tag{3.1.10}$$

The obtained regularized expression for the potential is of the form

$$\begin{aligned}\Omega^S_{div} &= 8\int\frac{d^4k_E}{(2\pi)^4}\int_{1/\Lambda^2}^{\infty}\frac{d\tau}{\tau}\left\{\exp\left[\tau\left(-k_4^2-\frac{1}{4}(\sum_{i=\pm}E^{\Delta}_{i,0})^2\right)\right]\right.\\ &- \left.\exp\left[\tau\left(-k_4^2-\frac{1}{4}(\sum_{i=\pm}E^{\Delta=0}_{i,0})^2\right)\right]\right\}\\ &+ 12\int\frac{d^4k_E}{(2\pi)^4}\int_{1/\Lambda^2}^{\infty}\frac{d\tau}{\tau}\left\{\exp\left[\tau\left(-k_4^2-E_0^2\right)\right]\right\}\,. \end{aligned} \tag{3.1.11}$$

Now, if one integrate over dk_4, Ω^S_{div} takes a form

$$\begin{aligned}\Omega^S_{div} &= \frac{8}{\sqrt{2}}\int\frac{d^3k}{(2\pi)^{3.5}}\int_{1/\Lambda^2}^{\infty}\frac{d\tau}{\tau^{1.5}}\left\{\exp\left[-\tau\left(\frac{1}{4}(\sum_{i=\pm}E^{\Delta}_{i,0})^2\right)\right]\right.\\ &- \left.\exp\left[-\tau\left(\frac{1}{4}(\sum_{i=\pm}E^{\Delta=0}_{i,0})^2\right)\right]\right\}\\ &+ \frac{12}{\sqrt{2}}\int\frac{d^3k}{(2\pi)^{3.5}}\int_{1/\Lambda^2}^{\infty}\frac{d\tau}{\tau^{1.5}}\left\{\exp\left[-\tau\left(E_0^2\right)\right]\right\}\,. \end{aligned} \tag{3.1.12}$$

It can be seen, that however integrals are over the full three dimensional momentum space, the exponential factors suppress the energy contributions at higher momenta.

3.1.1.4 Pauli-Villars regularization

This is the most tricky scheme of regularization. At first we introduce an arbitrary number of coupling constants C_α and mass regulators M_α. After this procedure, divergent part of the grand thermodynamic potential (3.1.6) transforms into

$$\Omega_{div}(M,|\Delta|,q)\longrightarrow\sum_\alpha C_\alpha\Omega_{div}(M_\alpha,|\Delta|,q)\,. \tag{3.1.13}$$

In the next step we regularize potential by a 3-dim cut-off regulator Λ.

$$\sum_\alpha C_\alpha\Omega_{div}(M_\alpha,|\Delta|,q)\longrightarrow\sum_\alpha C_\alpha\Omega^{3d}_{div}(M_\alpha,|\Delta|,q,\Lambda)\,. \tag{3.1.14}$$

Finally we expand the thermodynamic potential around the large value of parameter Λ and impose a condition that final result should be finite and independent on regulator Λ.

$$\sum_\alpha C_\alpha\Omega^{3d}_{div}(M_\alpha,|\Delta|,q,\Lambda)\xrightarrow{\Lambda\to\infty\,\cap\,\Omega^{PV}_{div}=finite}\Omega^{PV}_{div}\,. \tag{3.1.15}$$

To satisfy above conditions we derive equations on C_α and M_α, minimaly one has to introduce three additional parameters C_α and M_α respectively

$$1+\sum_{\alpha=1}^{3}C_\alpha=0\,;\quad M^2+\sum_{\alpha=1}^{3}C_\alpha M_\alpha^2=0\,;\quad M^4+\sum_{\alpha=1}^{3}C_\alpha M_\alpha^4=0\,. \tag{3.1.16}$$

Set of equations (3.1.16) is solved by the formula:

$$C_1 = -3,\ C_2 = 3,\ C_3 = -1,\ M_1^2 = M^2+\Lambda^2,\ M_2^2 = M^2+2\Lambda^2,\ M_3^2 = M^2+3\Lambda^2\,, \quad (3.1.17)$$

where Λ is a new free parameter that value will be set by fitting hadron sector properties.

Eventually, the final expression for the divergent part of the thermodynamic potential in this scheme reads

$$\begin{aligned}\Omega_{div}^{PV} &= \frac{3}{8\pi^2}\sum_{\alpha=1}^{3} C_\alpha M_\alpha^4 \ln\frac{M^2}{M_\alpha^2} + \frac{1}{\pi^2}\left(\frac{|\Delta|^4}{4} - |\Delta|^2\mu^2\right)\sum_{\alpha=1}^{3} C_\alpha \ln\frac{M^2+|\Delta|^2}{M_\alpha^2+|\Delta|^2} \\ &+ \frac{|\Delta|^2}{2\pi^2}\sum_{\alpha=1}^{3} C_\alpha M_\alpha^2 \ln\frac{M^2+|\Delta|^2}{M_\alpha^2+|\Delta|^2} + \frac{1}{4\pi^2}\sum_{\alpha=1}^{3} C_\alpha M_\alpha^4 \left(\ln\frac{M^2+|\Delta|^2}{M_\alpha^2+|\Delta|^2} - \ln\frac{M^2}{M_\alpha^2}\right).\end{aligned} \quad (3.1.18)$$

One can directly present which terms of the grand thermodynamic potential Ω_{div} transform into the Pauli-Villars regularized expressions. These are:

$$-12\int^{\Lambda}\frac{d^3k}{(2\pi)^3}E_0 \ \xrightarrow{PV}\ \frac{3}{8\pi^2}\sum_{\alpha=1}^{3} C_\alpha M_\alpha^4 \ln\frac{M^2}{M_\alpha^2}\,, \quad (3.1.19)$$

$$4\sum_{i=\pm}\int\frac{d^3k}{(2\pi)^3}E_{i,0}^{\Delta=0} \ \xrightarrow{PV}\ -\frac{1}{4\pi^2}\sum_{\alpha=1}^{3} C_\alpha M_\alpha^4 \ln\frac{M^2}{M_\alpha^2}\,, \quad (3.1.20)$$

$$\begin{aligned}-4\sum_{i=\pm}\int\frac{d^3k}{(2\pi)^3}E_{i,0}^{\Delta} \ &\xrightarrow{PV}\ \frac{1}{\pi^2}\left(\frac{|\Delta|^4}{4} - |\Delta|^2\mu^2\right)\sum_{\alpha=1}^{3} C_\alpha \ln\frac{M^2+|\Delta|^2}{M_\alpha^2+|\Delta|^2} \\ &+\frac{|\Delta|^2}{2\pi^2}\sum_{\alpha=1}^{3} C_\alpha M_\alpha^2 \ln\frac{M^2+|\Delta|^2}{M_\alpha^2+|\Delta|^2} + \frac{1}{4\pi^2}\sum_{\alpha=1}^{3} C_\alpha M_\alpha^4 \ln\frac{M^2+|\Delta|^2}{M_\alpha^2+|\Delta|^2}\,.\end{aligned} \quad (3.1.21)$$

3.1.2 Parameters of the Nambu Jona-Lasinio model

Once we have chosen the specified method of regularization of infinite integrals, there are still three parameters to determine. These are: effective coupling constant in the quark-antiquark channel G, effective coupling constant in the quark-quark channel G' and regularization parameter Λ. The values of G and Λ can be determined by matching the hadron sector properties. Following Ref. [33], G and Λ are fixed by two physical quantities: pion decay constant $f_\pi = 93$ MeV and the quark condensate density $\langle\bar{u}u\rangle = \langle\bar{d}d\rangle = -(250\text{ MeV})^3$. These quantities are functions of M_0 (constituent quark mass at zero baryon density) and Λ, and can be calculated in the framework of the NJL model. Now using the self-consistency condition, $M_0 = -4G\langle\bar{u}u\rangle$ (we discuss massless quarks), that links G and Λ with M_0, we finally get the values of G and Λ.

In different regularization schemes, one has:

3.1.2.1 3d cut-off regularization

- quark condensate density

$$\langle \bar{u}u \rangle = -6M_0 \int^{\Lambda} \frac{d^3k}{(2\pi)^3} \frac{1}{E_0} \tag{3.1.22}$$

- pion decay constant

$$f_\pi^2 = 3M_0^2 \int^{\Lambda} \frac{d^3k}{(2\pi)^3} \frac{1}{E_0^3} \tag{3.1.23}$$

3.1.2.2 4d cut-off regularization

- quark condensate density

$$\langle \bar{u}u \rangle = -12M_0 \int^{\Lambda} \frac{d^4k_E}{(2\pi)^4} \frac{1}{E_0^2 + k_4^2} \tag{3.1.24}$$

- pion decay constant

$$f_\pi^2 = 12M_0^2 \int^{\Lambda} \frac{d^4k_E}{(2\pi)^4} \frac{1}{(E_0^2 + k_4^2)^2} \tag{3.1.25}$$

3.1.2.3 Schwinger regularization

- quark condensate density

$$\langle \bar{u}u \rangle = -\frac{3}{4\pi^2} M_0 \int_{1/\Lambda^2}^{\infty} \frac{d\tau}{\tau^2} \exp[-\tau M_0^2] \tag{3.1.26}$$

- pion decay constant

$$f_\pi^2 = \frac{3}{4\pi^2} M_0^2 \int_{1/\Lambda^2}^{\infty} \frac{d\tau}{\tau} \exp[-\tau M_0^2] \tag{3.1.27}$$

3.1.2.4 Pauli-Villars regularization

- quark condensate density

$$\langle \bar{u}u \rangle = -6M_0 \int^{\Lambda} \frac{d^3k}{(2\pi)^3} \frac{1}{E_0} \quad \stackrel{PV}{\longrightarrow}$$

$$M_0 \sum_\alpha \left[-\frac{3}{2\pi^2} C_\alpha \Lambda^2 - \frac{3}{4\pi^2} C_\alpha M_\alpha^2 \ln \frac{M_\alpha^2}{\Lambda^2} - \frac{3}{4\pi^2} (1 - \ln 4) C_\alpha M_\alpha^2 \right] + O(1/\Lambda^2)\,, \tag{3.1.28}$$

and with the conditions (3.1.16) we get

$$\langle \bar{u}u \rangle = \frac{3}{4\pi^2} M_0 \sum_{\alpha=1}^{3} C_\alpha M_\alpha^2 \ln \frac{M_0^2}{M_\alpha^2} \tag{3.1.29}$$

- pion decay constant

$$f_\pi^2 = 3M_0^2 \int^{\Lambda} \frac{d^3k}{(2\pi)^3} \frac{1}{E_0^3} \xrightarrow{PV} M_0^2 \sum_\alpha \left[-\frac{3}{4\pi^2} C_\alpha \ln \frac{M_\alpha^2}{\Lambda^2} - \frac{3}{2\pi^2}(1 - \ln 2) C_\alpha \right] + O(1/\Lambda^2)$$

and with the conditions (3.1.16) we get

$$f_\pi^2 = \frac{3}{4\pi^2} M_0^2 \sum_{\alpha=1}^{3} C_\alpha \ln \frac{M_0^2}{M_\alpha^2} \tag{3.1.30}$$

The values of G and Λ for each regularization scheme are given in Table 3.1.

	S	PV	4d	3d
Λ	1.086	1.12	1.015	0.635
$G\Lambda^2$	3.78	4.47	3.93	2.2
M_0	0.2	0.22	0.238	0.33

Table 3.1: Numerical values of the regularization parameter Λ in GeV and dimensionless quantity $G\Lambda^2$ for different regularization schemes. In the last row, the value of the quark constituent mass at zero density M_0 is given in GeV.

3.1.2.5 Coupling constant G'

Strength of the quark-antiquark interaction was given by fitting vacuum properties. It appears that one can not perform similar procedure with the quark-quark channel because effective coupling G' can not be related to any known physical quantity. One can try to deduce the value of G' from the value of G. Starting from underlying interaction of the type

$$\mathcal{L}_{int} = -g_c(\overline{\psi}\gamma_\mu \lambda^A \psi)^2 \,, \tag{3.1.31}$$

and performing a Fierz transformation, the authors of Ref. [41] obtained a relation $G' = 0.75\, G$. Consequently for the presentation of the results we keep $G' = 0.75\, G$. The strength of the quark-quark interaction influences the value of the 2SC color superconducting gap Δ, which in turn influences the range of the nonuniform chiral phase at zero temperature [38]. Thereby, we firstly show the results for $G' = 0$, against this background, the influence of the color superconducting phase can be better illustrated.

3.2 Results and discussion

We minimize the thermodynamic potential

$$\Omega_0 = \frac{M^2}{4G} + \frac{|\Delta|^2}{4G'} + \frac{M^2 f_\pi^2 \vec{q}^{\,2}}{2M_0^2} - 2\sum_{s=\pm}\sum_{i=\pm}\int \frac{d^3k}{(2\pi)^3}\left(E_{i,s}^{\Delta} - E_{i,0}^{\Delta} + E_{i,0}^{\Delta=0} - E_s\right)$$
$$+ 2\sum_{s=\pm}\int_{E_s\leq\mu}\frac{d^3k}{(2\pi)^3}(E_s-\mu) + \Omega_{div}^{scheme} \qquad (3.2.1)$$

with respect to the constituent quark mass M, aboslute value of wave vector $\vec{q}$ and gap parameter Δ, as a function of chemical potential. The last term of equation (3.2.1) depends on the regularization scheme, as was described in the previous section.

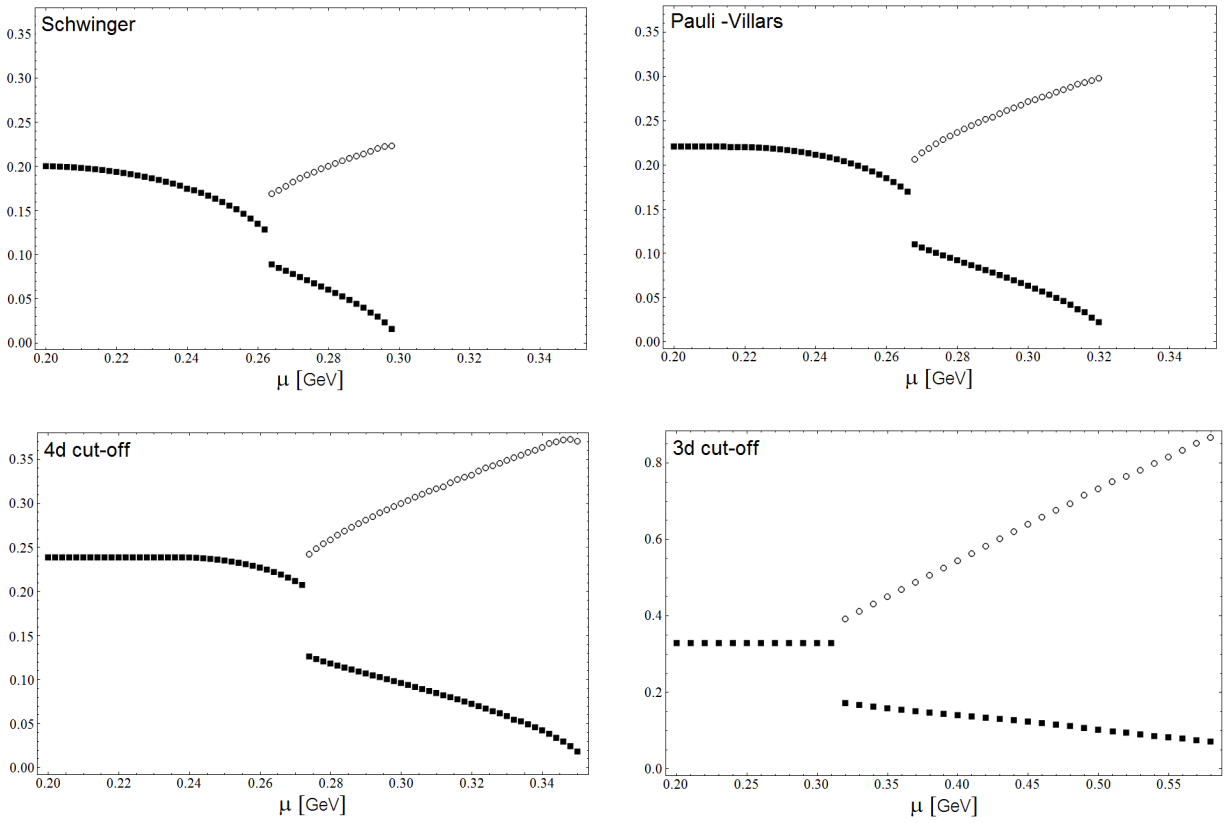

Figure 3.1: Dependence of quark constituent mass M (solid points) and absolute value of wave vector $\vec{q}$ (open points), as a function of quark chemical potential (all in GeV unites), at zero temperature, in different regularization schemes.

3.2.1 G' equal zero

In Fig.3.1, we present phase diagrams for all discussed methods of regularization. Because we set $G' = 0$, there is no 2SC color superconducting phase. With the above constrain, situation is easier to study and some general observations can be found. This is in contrast to the case when $\Delta \neq 0$ and one can mostly rely on numerical results.

Most of all, the region of nonuniform chiral phase exists on each diagram and the orders of phase transitions are the same for different regulators. Considering further Fig.3.1, it is sufficient to concentrate on the simplified version of the grand thermodynamic potential

$$\Omega_0^{\Delta=0} = \frac{M^2}{4G} - 12\sum_{s=\pm}\int\frac{d^3k}{(2\pi)^3}E_0 + \frac{M^2 f_\pi^2 \vec{q}^{\,2}}{2M_0^2} + 6\sum_{s=\pm}\int_{E_s\leq\mu}\frac{d^3k}{(2\pi)^3}(E_s - \mu)\,. \qquad (3.2.2)$$

In the range of quark chemical potential from zero up to some μ_{c1} (its value is of the order of M_0 and depends on regularization scheme) system stays at minimum corresponding to the chiral uniform phase. This minimum is governed by the chiral symmetry breaking part of the thermodynamic potential (mass term plus Dirac sea contribution). In this region, Fermi sea effectively does not contribute to the potential $\Omega_0^{\Delta=0}$. Plot of chiral symmetry breaking terms as a function of constituent mass M for different regularization schemes is shown in Fig.3.2. We will return to this plot later.

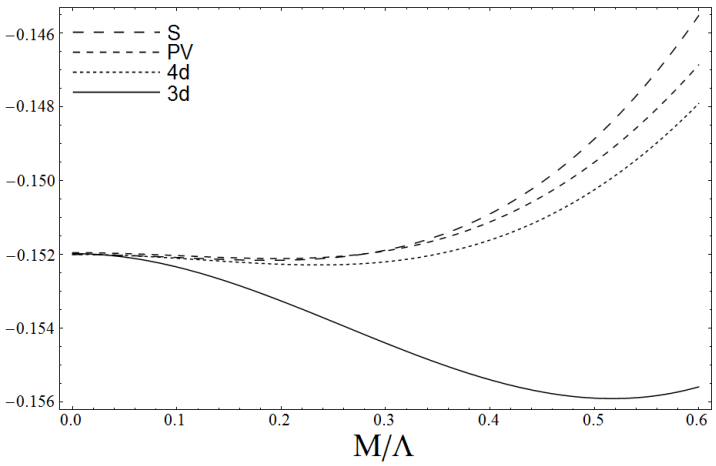

Figure 3.2: Mass term plus Dirac sea contribution (dimensionless units) of the grand thermodynamic potential (3.2.2) in different regularization schemes: 3d cut-off (thick line); 4d cut-off (short-dashed line); Pauli-Villars (middle-dashed line); Schwinger (long-dashed line); as a function of the constituent mass M (in the unites of cut-off Λ).

Around $\mu = \mu_{c1}$, the value of M begins to lower, system leaves its previous minimum, and the negative contribution due to the Fermi sea starts to grow. If one consider only uniform phase, this is the moment of restoration of the chiral symmetry. However, spatially nonuniform chiral condensate gives another possibility. On the one hand, non-zero q

value effectively weakens minimum corresponding to the uniform chiral phase and moves it towards lower values of the constituent mass M. On the other hand, because of non-zero q, Fermi surface is deformed. Consequently, Fermi sea gives negative contribution already at relatively large values of M. These two effects compete with each other. With growing μ, absolute value of vector q also increases. At some value of q, minimum corresponding to the broken chiral symmetry disappears. This happens around $\mu = \mu_{c2}$, there is a transition into the chirally symmetric phase.

Above description agrees with the numerical results. Inhomogeneous phase appears with accordance to the constituent mass sequence. The lowest $\mu_{c1} = 263$ MeV is in the Schwinger scheme ($M_0 = 200$ MeV), higher is in the Pauli-Villars ($M_0 = 220$ MeV) and in the 4d cut-off ($M_0 = 238$ MeV). The highest $\mu_{c1} = 320$ MeV is in the 3d cut-off regularization ($M_0 = 330$ MeV). The moment of disappearance of the nonuniform phase follows the opposite order. This observation can be understand on the basis of Fig.3.2. Minimum corresponding to the uniform chiral phase, as a function of mass M, is the weakest in the Schwinger scheme. Consequently, growing value of vector q destroys this minimum as the first. In turn, the deepest minimum is in the 3d cut-off scheme, and nonuniform phase persists in this scheme up to $\mu_{c2} = 580$ MeV. Values of the critical chemical potentials of phase transitions are given in Table 3.2.

μ_c	S	PV	4d	3d
Ch/NCh	0.263	0.268	0.274	0.320
NCh/QM	0.298	0.320	0.350	0.580

Table 3.2: Numerical values of critical chemical potentials μ_c in GeV, for different regularization schemes. Uniform chiral into the nonuniform chiral phase transition (Ch/NCh). Nonuniform chiral phase into the quark matter transition (NCh/QM).

3.2.2 $G' = 0.75\, G$

The values of constituent mass, wave vector and gap parameter, as a function of chemical potential, in different regularization schemes, are given in Figures 3.3 - 3.5. As can be seen, similarily as for $G' = 0$, there is a common pattern of phase transitions. From uniform to nonuniform chiral phase and then to superconducting phase. All transitions are of the first order and existence of the nonuniform phase is independent of considered regularization scheme. However, strength of the transitions depends on the regularization scheme. This is particularly visible in Fig.3.3.

Some quantitative features change with the scheme. One can find that schemes cluster in two groups, which one can call "relativistic" schemes (S, PV, 4d) and 3d cut-off. However, let us note that the distinction between relativistic and non-relativistic schemes has no deep meaning because the thermodynamic system singles out one reference frame.

Comparing the quantitative results, we consider values of constituent mass, wave vector, gap parameter, critical chemical potential, and strength of thefirst order phase transitions.

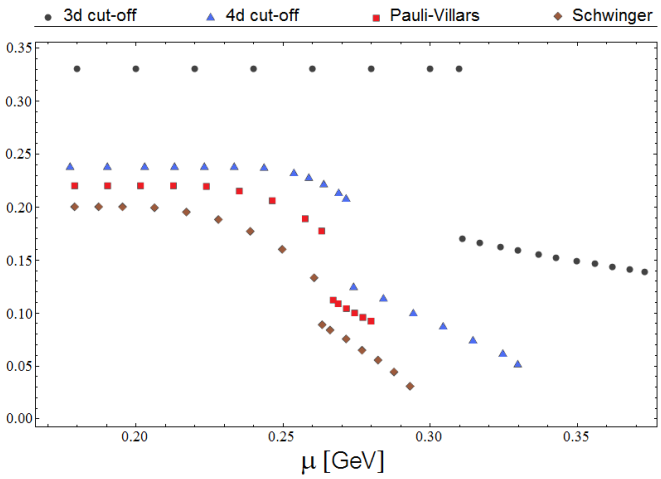

Figure 3.3: The constituent mass M, as a function of quark chemical potential μ, in different regularization schemes in GeV units.

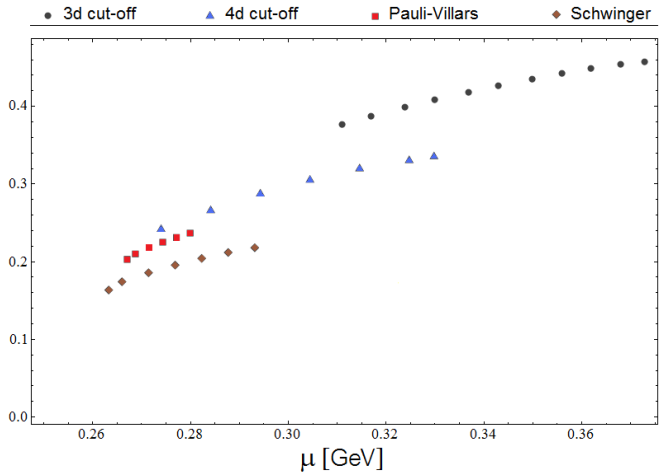

Figure 3.4: The value of wave vector q, as a function of quark chemical potential μ, in the different regularization schemes in GeV units. The values of μ for non-zero q describe the range of existence of the spatially nonuniform chiral phase.

The position of transition from the uniform to the nonuniform chiral phase is the most resistant against the choice of regularization scheme. First critical potential changes within the range of 5 per cent for relativistic schemes, while in the case of 3d within 18 per cent. The same as for $G' = 0$, the sequence of μ_{c1} is consistent with the values

of constituent quark mass at zero density. As one can see, non-zero gap parameter Δ does not affect the position of μ_{c1} (Ch/NCh) for the so-called relativistic schemes, but in the 3d cu-off, first critical chemical potential decreases slightly from 320 to 311 MeV. The position of second transition, changes within the range of 19 per cent for relativistic schemes, including the 3d cut-off within 34 per cent. In comparison with the previously discussed situation ($G' = 0$), 2SC color superconducting phase restricts the region of spatially nonuniform phase from the upper values of chemical potential. In the 3d cut-off scheme, the position of μ_{c2} decreases significantly from 580 MeV to 373 MeV. In the other regularizations this effect is less visible, however, in the Pauli-Villars scheme, dominance of the 2SC phase is so strong, that NCh phase is restricted to the interval of only 13 MeV width. Because of this, in opposite to the case of $G' = 0$, position of the second transition is earlier in the PV scheme than in the Schwinger method. Influence of the coupling constant G' is understandable because larger G' strengthens diquark interaction which dominates over quark - antiquark interaction. In the Pauli-Villars scheme, there is no region of coexistence of NCh and 2SC phases. As can be seen in Fig.3.5, the value of gap Δ is of the same order as in the 3d cut-off scheme. Consequently, in the PV scheme, above $G' = 0.83G$ the nonuniform chiral phase vanishes, and phase transition to the color superconducting phase at $\mu_{c2} = 0.26$ GeV takes place directly from the uniform chiral phase. However, this value of critical chemical potential is rather low which questions the physical sensibility to set $G' = 0.83\ G$ in the PV scheme.

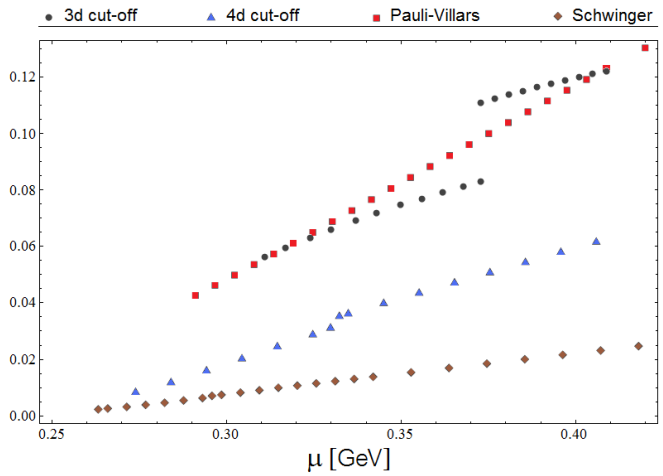

Figure 3.5: The gap parameter Δ as a function of quark chemical potential μ, in different regularization schemes in GeV units.

The range of variability of the value of mass M for the S, PV and 4d schemes is about 20 per cent at μ equal to zero and is about 60 per cent at chemical potentials corresponding to the Ch/NCh transition. Likewise, the range of variability of the wave vector q is 50 per cent at chemical potentials corresponding to the Ch/NCh transition. Similar comparison at NCh/QM transition is meaningless because of the large differences between the NCh/QM critical potentials. The dependence of parameters M and q on

the quark chemical potential is the same in different regularizations. With increasing chemical potential, the value of q is growing and the M value is declining. Relatively the least correlated is the dependence of gap parameter Δ. However, independently of the regularization choice, the value of gap Δ increases with increasing μ. The values of critical chemical potentials of the phase transitions are given in Table 3.3.

μ_c	S	PV	4d	3d
Ch/NCh	0.263	0.268	0.274	0.311
NCh/2SC	0.296	0.281	0.330	0.373

Table 3.3: Numerical values of the critical chemical potentials μ_c in GeV. Uniform into the nonuniform chiral phase transition (Ch/NCh) and nonuniform chiral into the superconducting phase transition (NCh/2SC), for different regularization schemes. In the S, 4d, 3d schemes the 2SC phase appears already at Ch/NCh phase transition and both phases coexist, but, the value of the gap parameter is relatively low in the coexistence region. In the PV scheme, 2SC phase appears at the NCh/2SC phase transition.

The strength of phase transition depends on regularization scheme. The strongest phase transitions are in the 3d cut-off, the weakest in the Schwinger proper time regularization. In the case of transition to the 2SC phase, the jump of the color superconducting gap ranges from 28 MeV in the 3d cut-off to only 1 MeV in the Schwinger regularization. There is still a possibility of coexistence between the chiral and superconducting phases. Coexistence occurs in the all schemes with the exception of Pauli-Villars. Any conclusion which follows from this phenomenon is thus model dependent.

3.3 Conclusions

We have studied the nonuniform chiral phase in the Nambu Jona-Lasinio model in different regularization schemes. We confirm that the qualitative features of the phase diagram are independent of considered regularization scheme. The generic phase diagram in the 4d cut-off regularization (including the 2SC phase) is shown in Fig.3.6.

The quantitative results (values of constituent mass, wave vector, critical chemical potential) match satisfactorily within "relativistic" schemes. Results obtained with the 3d cut-off differ widely from the previous. Above observation is well-justified by the dependence of the chiral symmetry breaking term, as a function of constituent mass (Fig.3.2). It is worth to recall, that Quark Meson model ([65]) gives similar results to the 3d cut-off regularized NJL model. This argument favours seemingly trivial three-dimensional momentum cut-off.

Additionally, gap parameter Δ, as well as the magnitude of the jump in the gap parameter, shows the clear dependence on the choice of regularization scheme. Differences

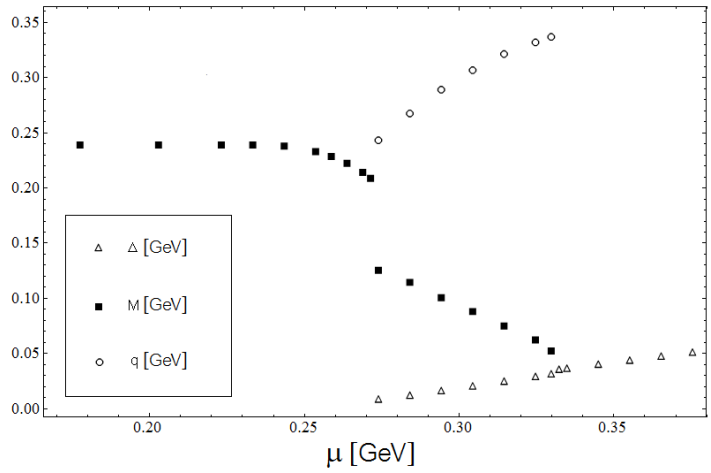

Figure 3.6: The phase diagram at one plot in 4d cut-off regularization scheme (in GeV units).

appear not only between the "relativistic" and 3d cut-off schemes but also within the set of "relativistic" regularizations. These findings tell us that one can set the magnitude of the gap parameter in the MeV scale but its precise value in the large extand is an unknown quantity. From the other hand, the general qualitative pattern that the gap parameter increases with increasing value of the chemical potential μ is independent on the choice of regularization scheme.

The size of spatially nonuniform phase depends on the relative strength of G' and G coupling constants. The larger G' constant, the shorter the range of nonuniform phase. This conclusion is also independent of the regularization scheme.

We also find that in the Pauli-Villars scheme, in contrast to the other schemes, there is no coexistence region of the nonuniform and 2SC phases. Thus, such a coexistence remains an open question.

There is no general argument which scheme better suits the task of the phase diagram analysis. Neither the relativistic approach (thermodynamic systems singles out prefered reference frame) nor gauge independence (the NJL model is not a gauge theory) favor any scheme in the present considerations. Schwinger regularization gives effectively a constrain on the energy spectrum and not on the momenta. In this sense, if quasi-particle spectrum is anisotropic, it appears to be more appropriate. On the other hand, Schwinger scheme gives the smallest quark constituent mass of the order of 200 MeV. On can partially get around this problem. We fit the NJL model parameters to the value of quark condensate density and to the value of pion decay constant. Because the value of quark condensate density is known with large uncertainty [42], there is some freedom in the parameter fit. It turns, that for $\langle \bar{u}u \rangle \approx -(200\text{MeV})^3$, constituent quark mass at zero density is already above 260 MeV. We will turn back to above discussion in the next chapters of this work.

Finally, let us stress that our analysis does not prove that the spatially nonuniform chiral phase exists. Above all, we did our study in the chiral limit, when current quark

masses are equal zero. This simplification is due to the technical problems that originate when one calculate the grand thermodynamic potential in the presence of the spatially nonuniform ansatz together with the non-zero current quark mass. The attempt to discuss spatially nonuniform condensate, not only in the chiral limit, will be taken in the chapter 4. Nevertheless, the strong result of our analysis is that the main features of the phase diagram, which includes nonuniform phase, are robust against the choice of regularization scheme.

Chapter 4

Influence of the non-zero current quark mass on the nonuniform chiral and 2SC color superconducting phases

The main goal of this chapter is to analyze, within the framework of the NJL model, the influence of the non-zero current quark mass on existence of the nonuniform chiral phase. In the previous chapter, we have studied the system at zero temperature limit. We arrived at the result, that independently on the regularization method, there exists a finite range of quark chemical potential, where spatially inhomogeneous chiral condensate dominates. It follows from the previous chapter, that coexistence of the 2SC color superconducting and chiral phases is preferable in this limit. Consequently, in the present chapter we include also the possibility of a diquark condensation. Nevertheless, aforementioned results was obtained in the chiral limit. That is why, natural consequence is to extend our previous analysis on the influence of the non-zero quark current mass.

Most of the results presented in this chapter have been published in Ref. [44].

4.1 Evaluation of the grand thermodynamic potential

The starting point is the Nambu Jona-Lasinio Euclidean action

$$\begin{aligned} \mathcal{S} &= \int_0^\beta d\tau \int d^3x \left(\bar{\psi}(i\gamma^\nu \partial_\nu + \mu\gamma^0 - m)\psi + G\left[(\bar{\psi}\psi)^2 + (\bar{\psi} i\gamma_5 \vec{\tau}\psi)^2\right] \right. \\ &+ \left. G'(\bar{\psi}_c i\gamma_5 \tau_2 \lambda^A \psi)(\bar{\psi} i\gamma_5 \tau_2 \lambda^A \psi_c) \right), \end{aligned} \tag{4.1.1}$$

where ψ is the quark field, $\psi_c = C\bar{\psi}^T$ is the conjugate field and μ is the quark chemical potential. The vector $\vec{\tau}$ is the isospin vector of Pauli matrices and λ^A, $A = 2, 5, 7$ are three color antisymmetric $SU(3)$ group generators.

After the Hubbard Stratanovich transformation, that introduces effective bosonic degrees of freedom, one obtains

$$\mathcal{S}_{HS} = \frac{1}{2}\int_0^\beta d\tau \int d^3x \left(\bar{\psi}(i\gamma^\nu \partial_\nu + \mu\gamma^0 - m + \sigma + i\gamma_5 \vec{\pi}\cdot\vec{\tau}) \right.$$
$$\left. + \bar{\psi}_c(i\gamma^\nu \partial_\nu - \mu\gamma^0 - m + \sigma + i\gamma_5 \vec{\pi}\cdot\vec{\tau})\psi_c + \Delta_A \bar{\psi}_c i\gamma_5\tau_2\lambda^A\psi + \Delta_A^* \bar{\psi} i\gamma_5\tau_2\lambda^A\psi_c - \frac{\sigma^2}{2G} - \frac{\vec{\pi}^2}{2G} - \frac{|\Delta|^2}{2G'} \right). \tag{4.1.2}$$

Partition function has a form

$$Z = \int \mathcal{D}\bar{\psi}\mathcal{D}\psi\mathcal{D}\bar{\psi}_c\mathcal{D}\psi_c\mathcal{D}\sigma\mathcal{D}\,\vec{\pi}\mathcal{D}\Delta_A\mathcal{D}\Delta_A^* \exp\{\mathcal{S}_{\mathcal{HS}}\}\,. \tag{4.1.3}$$

Next, we introduce a mean field ansatz

$$\begin{aligned} &\sigma = 2G\langle\bar{\psi}\psi\rangle = -M\cos\vec{q}\cdot\vec{x}\,, \quad \pi^a = 2G\langle\bar{\psi}i\gamma_5\tau^a\psi\rangle = -\delta_{a3}M\sin\vec{q}\cdot\vec{x}\,, \\ &\Delta^A = 2G'\langle\bar{\psi}i\gamma_5\tau_2\lambda^A\psi_c\rangle = \delta_{A2}\,\Delta\,, \end{aligned} \tag{4.1.4}$$

and perform a chiral rotation at quark fileds

$$\psi = \sqrt{U}\psi', \;\; \sqrt{U} = \exp\{-i\gamma_5\tau_3\vec{q}\cdot\,\vec{x}\}\,. \tag{4.1.5}$$

Than, after the introduction of Nambu-Gorkov basis $\chi^T = (\psi, \psi_c)$ [43], the mean-field partition function takes a form

$$Z_{MF} = \int \mathcal{D}\overline{\chi}\mathcal{D}\chi \exp\{\mathcal{S}_{\mathcal{MF}}\}\,, \tag{4.1.6}$$

where

$$\mathcal{S}_{MF} = \frac{1}{2}\int_0^\beta \int d^3x \left[\,\overline{\chi}\,S^{-1}\chi - \frac{M^2}{2G} - \frac{|\Delta|^2}{2G'}\right]. \tag{4.1.7}$$

To determine the ground state of the system we calculate the grand thermodynamic potential

$$\Omega_{MF} = -\frac{T}{V} \ln \{Z_{MF}\} \,. \tag{4.1.8}$$

After performing integrals over the fermion fields we finally get the expression

$$\Omega_{MF} = \frac{M^2}{4G} + \frac{|\Delta|^2}{4G'} - \frac{T}{2V} \ln \left\{ \det \left\{ S^{-1} \right\} \right\} \,, \tag{4.1.9}$$

where determinant is to be taken over the Nambu-Gorkov, Dirac, color, flavor and space-time indices. The matrix of the operator S^{-1} in the Nambu-Gorkov space has a form

$$S^{-1} = \left[\begin{array}{cc} i\gamma^\nu(\partial_\nu - \frac{1}{2} i\gamma_5\tau_3 q_\nu) + \mu\gamma^0 - M - m\, e^{-i\gamma_5\tau_3 \vec{q}\cdot\vec{x}} & i\gamma_5\tau_2\lambda_2\Delta^* \\ i\gamma_5\tau_2\lambda_2\Delta & i\gamma^\nu(\partial_\nu - \frac{1}{2} i\gamma_5\tau_3 q_\nu) - \mu\gamma^0 - M - m\, e^{-i\gamma_5\tau_3 \vec{q}\cdot\vec{x}} \end{array} \right] . \tag{4.1.10}$$

4.1.1 Decomposition of the Ω_{MF}

For the non-zero values of current quark mass, operator S^{-1} (4.1.10) depends explicitly on a space coordinate $\vec{x}$. That is why, the straightforward calculation of determinant in equation (4.1.9) is impossible. As a consequence, most of the studies on the nonuniform chiral phases, within the framework of the NJL model, are done in the chiral limit. Only recently, the author of Refs. [45, 46] have proposed a method that allows to consider the influence of the non-zero current quark mass. The main idea is to expand the expression for the potential Ω_{MF} in a series of the current quark mass m. We follow this approach, however, in our analysis we incorporate also the 2SC color superconducting phase. The first step is to decompose operator S^{-1} into the parts dependent and independent on the mass m

$$S^{-1} = S_0^{-1} - V_m \,, \tag{4.1.11}$$

where

$$S_0^{-1} = \left[\begin{array}{cc} i\gamma^\nu(\partial_\nu - \frac{1}{2} i\gamma_5\tau_3 q_\nu) + \mu\gamma^0 - M_t & i\gamma_5\tau_2\lambda_2\Delta^* \\ i\gamma_5\tau_2\lambda_2\Delta & i\gamma_\nu(\partial_\nu - \frac{1}{2} i\gamma_5\tau_3 q_\nu) - \mu\gamma^0 - M_t \end{array} \right] , \tag{4.1.12}$$

$$V_m = \left[\begin{array}{cc} m\left\{\exp(-i\gamma_5\tau_3\vec{q}\cdot\vec{x}) - 1\right\} & 0 \\ 0 & m\left\{\exp(-i\gamma_5\tau_3\vec{q}\cdot\vec{x}) - 1\right\} \end{array} \right] , \tag{4.1.13}$$

$$M_t = M + m\,. \tag{4.1.14}$$

Expanding the grand termodynamic potential (4.1.9) up to the terms of order V_m, we decompose Ω_{MF} into the two parts [45]

$$\Omega_{MF} = \Omega_0 + \delta\Omega + \mathcal{O}(V_m^2)\,, \tag{4.1.15}$$

$$\Omega_0 = \frac{(M_t - m)^2}{4G} + \frac{|\Delta|^2}{4G'} - \frac{T}{2V}\ln\left\{\int \mathcal{D}\overline{\chi}\mathcal{D}\chi\ \exp\left(\int_0^\beta \int d^3x\ \overline{\chi}\, S_0^{-1}\chi\right)\right\}, \tag{4.1.16}$$

$$\delta\Omega = \frac{T}{2V}\,\frac{\int \mathcal{D}\overline{\chi}\mathcal{D}\chi\ \left\{\int_0^\beta \int d^3x\ \overline{\chi}\, V_m\chi\right\}\exp\left\{\int_0^\beta \int d^3x\ \overline{\chi}\, S_0^{-1}\chi\right\}}{\int \mathcal{D}\overline{\chi}\mathcal{D}\chi\ \exp\left\{\int_0^\beta \int d^3x\ \overline{\chi}\, S_0^{-1}\chi\right\}}\,. \tag{4.1.17}$$

Using the standard method one can calculate the thermodynamic potential Ω_0 [38]

$$\begin{aligned}
\Omega_0 \;=\;& \frac{(M_t - m)^2}{4G} + \frac{|\Delta|^2}{4G'} + 2\sum_{s=\pm}\int_{E_s\le\mu}\frac{d^3k}{(2\pi)^3}(E_s - \mu) - 2\sum_{s=\pm}\int\frac{d^3k}{(2\pi)^3}\left(E_s + \sum_{i=\pm}E^\Delta_{i,s}\right)\\
-\;& \sum_{s=\pm}4T\int\frac{d^3k}{(2\pi)^3}\left[\ln\left(1+\exp\left(-\frac{E^\Delta_{+,s}}{T}\right)\right) + \ln\left(1+\exp\left(-\frac{E^\Delta_{-,s}}{T}\right)\right)\right]\\
-\;& \sum_{s=\pm}2T\int\frac{d^3k}{(2\pi)^3}\left[\ln\left(1+\exp\left(-\frac{(Es+\mu)}{T}\right)\right) + \ln\left(1+\exp\left(-\frac{|Es-\mu|}{T}\right)\right)\right],
\end{aligned} \tag{4.1.18}$$

where

$$E^\Delta_{\pm,s} = \sqrt{(\mu \pm E_s)^2 + |\Delta|^2}\,,\quad E_\pm = \sqrt{\vec{k}^2 + M_t^2 + \frac{\vec{q}^{\,2}}{4} \pm \sqrt{(\,\vec{q}\cdot\vec{k})^2 + M_t^2\,\vec{q}^{\,2}}}\,. \tag{4.1.19}$$

We explicitly separated equation (4.1.18) into the zero temperature contribution (first line) and the finite temperature contribution (second and third lines). Temperature dependent contribution is finite, while zero temperature contribution contains divergent integrals and the regularization procedure is needed. In the previous chapter we discussed in detailed the method of regularization of the zero temperature term of the potential Ω_0.

Term $\delta\Omega$ (4.1.17) can be calculated with the help of standard integral over Grassmann variables

$$\frac{\int \mathcal{D}\overline{\chi}\mathcal{D}\chi\ \left\{\int_0^\beta \int d^3x\ \overline{\chi}\,\chi\right\}\exp\left\{\int_0^\beta \int d^3x\ \overline{\chi}\, S_0^{-1}\chi\right\}}{\int \mathcal{D}\overline{\chi}\mathcal{D}\chi\ \exp\left\{\int_0^\beta \int d^3x\ \overline{\chi}\, S_0^{-1}\chi\right\}} = \mathrm{tr}\,\{S_0\}\ . \tag{4.1.20}$$

Now, one can rewrite V_m in the more convenient form

$$V_m = \begin{bmatrix} m\left\{\cos\left(\vec{q}\cdot\vec{x}\right) - i\gamma_5\tau_3\sin\left(\vec{q}\cdot\vec{x}\right) - 1\right\} & 0 \\ 0 & m\left\{\cos\left(\vec{q}\cdot\vec{x}\right) - i\gamma_5\tau_3\sin\left(\vec{q}\cdot\vec{x}\right) - 1\right\} \end{bmatrix}. \tag{4.1.21}$$

Matrix τ_3 (third Pauli matrix) mixes two flavours, thus part of V_m proportinal to τ_3 does not contribute to the right hand side of the equation (4.1.17). Expanding cosine in the power series, equation (4.1.17) can be reduced to the form

$$\delta\Omega = \frac{T}{2V}\,\frac{\int \mathcal{D}\overline{\chi}\mathcal{D}\chi\ \left\{\int_0^\beta\int d^3x\ \left(1 - \frac{(\vec{q}\cdot\vec{x})^2}{2\,!} + \frac{(\vec{q}\cdot\vec{x})^4}{4\,!} - (...) - 1\right)\overline{\chi}\,\chi\right\}\exp\left\{\int_0^\beta\int d^3x\ \overline{\chi}\,S_0^{-1}\chi\right\}}{\int \mathcal{D}\overline{\chi}\mathcal{D}\chi\ \exp\left\{\int_0^\beta\int d^3x\ \overline{\chi}\,S_0^{-1}\chi\right\}}. \tag{4.1.22}$$

Next, we follow the scheme

$$\begin{aligned}
&\frac{\int \mathcal{D}\overline{\chi}\mathcal{D}\chi\ \left\{\int_0^\beta\int d^3x\ \frac{(\vec{q}\cdot\vec{x})^j}{j\,!}\overline{\chi}\,\chi\right\}\exp\left\{\int_0^\beta\int d^3x\ \overline{\chi}\,S_0^{-1}\chi\right\}}{\int \mathcal{D}\overline{\chi}\mathcal{D}\chi\ \exp\left\{\int_0^\beta\int d^3x\ \overline{\chi}\,S_0^{-1}\chi\right\}} = \mathrm{tr}\left\{\frac{(\,\vec{q}\,\cdot\,\vec{x}\,)^j}{j\,!}\,S_0\right\} \\
&= \frac{T}{V}\int_0^\beta d\tau\int d^3x\sum_{\vec{k}_1,\,\vec{k}_2}\sum_{n_1,n_2}\mathrm{tr}\left\{\frac{(\,\vec{q}\,\cdot\,\vec{x}\,)^j}{j\,!}\,e^{-i(\omega_{n_1}-\omega_{n_2})\tau}\,e^{i(\vec{k}_1-\vec{k}_2)\cdot\vec{x}}\,S_0(\omega_{n_1},\,\vec{k}_1;\omega_{n_2},\,\vec{k}_2)\right\} \\
&= \sum_{\vec{k},n}\left\{\frac{(q^jL^{j+1})/(2^j)}{(j+1)\,!}\,S_0(\omega_n,\,\vec{k})\right\},
\end{aligned} \tag{4.1.23}$$

where without loss of generality, we assumed wave vector $\vec{q}$ parallel to one of the axis. Parameter L denotes the space dimension in one direction. The result can be partially collected in a sine, and finally we get

$$\delta\Omega = \frac{1}{2}\,m\,T\left\{\frac{\sin\left\{(qL)/\,2\right\}}{(qL)/\,2} - 1\right\}\sum_{n=-\infty}^{n=+\infty}\int\frac{d^3k}{(2\pi)^3}\ \mathrm{tr}\left\{S_0(\omega_n,\,\vec{k})\right\}. \tag{4.1.24}$$

As one can expected, first order correction to the Ω_{MF}, due to the non-zero current quark mass, does not vanish only for the non-zero values of wave vector $\vec{q}$. In the thermodynamic limit, dependence on L can be neglected, and after the evaluation of the Matsubara sum,

that is quite complicated and more detailed study can be found at the next sections, we obtain

$$\begin{aligned}
\delta\Omega &= -4m\sum_{s=\pm}\int\frac{d^3k}{(2\pi)^3}\Bigg[-\frac{1}{2}\left(\frac{\partial(E_s+E^{\Delta}_{+,s})}{\partial M_t}\right)\left(1+\exp\left\{-\beta E^{\Delta}_{+,s}\right\}\right)^{-1} \\
&- \frac{1}{2}\left(\frac{\partial(E_s-E^{\Delta}_{+,s})}{\partial M_t}\right)\left(1+\exp\left\{\beta E^{\Delta}_{+,s}\right\}\right)^{-1} + \frac{1}{2}\left(\frac{\partial(E_s-E^{\Delta}_{-,s})}{\partial M_t}\right)\left(1+\exp\left\{-\beta E^{\Delta}_{-,s}\right\}\right)^{-1} \\
&+ \frac{1}{2}\left(\frac{\partial(E_s+E^{\Delta}_{-,s})}{\partial M_t}\right)\left(1+\exp\left\{\beta E^{\Delta}_{-,s}\right\}\right)^{-1}\Bigg] \\
&- 2m\sum_{s=\pm}\int\frac{d^3k}{(2\pi)^3}\Bigg[-\left(\frac{\partial E_s}{\partial M_t}\right)\left(1+\exp\left\{-\beta(E_s+\mu)\right\}\right)^{-1} \\
&+ \left(\frac{\partial E_s}{\partial M_t}\right)\left(1+\exp\left\{\beta(E_s-\mu)\right\}\right)^{-1}\Bigg].
\end{aligned} \tag{4.1.25}$$

4.1.2 Evaluation of the $\delta\Omega$

We have to evaluate the expression

$$\delta\Omega = -\frac{1}{2}\,m\,T\sum_{n=-\infty}^{n=+\infty}\int\frac{d^3k}{(2\pi)^3}\ \mathrm{tr}\left\{S_0(\omega_n,\,\vec{k})\right\}\,, \tag{4.1.26}$$

where trace is to be taken over the Nambu-Gorkov, color and flavor indices, and the sum is to be taken over the Matsubara frequencies ω_n. We work in the momentum-frequency basis that is introduced according to the following rule

$$\psi(x) = \sqrt{V}\sqrt{T}\sum_n\int\frac{d^3k}{(2\pi)^3}\exp\left\{-i(\omega_n\tau-\vec{k}\cdot\,\vec{x})\right\}\psi(k),\quad k=(i\omega_n,-\vec{k}),\quad \omega_n = 2\pi T(n+\frac{1}{2}\,). \tag{4.1.27}$$

The matrix form of the operator S_0^{-1} in the Nambu-Gorkov space, in the momentum-frequency basis reads

$$S_0^{-1} = \left[\begin{array}{cc} \gamma^0(k_0+\mu)-\gamma^i k_i+\frac{1}{2}\gamma_5\tau_3\gamma^i q_i - M_t & i\gamma_5\tau_2\lambda_2\Delta^* \\ i\gamma_5\tau_2\lambda_2\Delta & \gamma^0(k_0-\mu)-\gamma^i k_i+\frac{1}{2}\gamma_5\tau_3\gamma^i q_i - M_t] \end{array}\right]. \tag{4.1.28}$$

4.1.3 Evaluation of the trace of operator S_0

The operaor S_0 is given by its inverese form of (4.1.28). That is why, to evaluate the $\mathrm{tr}\,\{S_0\}$, we have to find the matrix form of this operator. However, because we only calculate a trace of S_0, it is enough to find diagonal elements of this operator. Moreover, because matrix λ_2 mixes only two colors, operator S_0^{-1} decomposes into the two block-diagonal matrices in color space. We concentrate on this block-diagonal part of S_0^{-1} that contains gap parameter Δ, we name it as $S^{-1}_{0,\,32\times32}$. In the color space its matrix form is

$$S^{-1}_{0,\,32\times32} = \left[\begin{array}{cc} A & B \\ C & D \end{array}\right], \tag{4.1.29}$$

where in the Nambu-Gorkov and flavor spaces

$$A = D = \left[\begin{array}{cccc} \gamma^\nu K_\nu^+ + \frac{1}{2}\gamma_5\gamma^i q_i - M_t & 0 & 0 & 0 \\ 0 & \gamma^\nu K_\nu^- + \frac{1}{2}\gamma_5\gamma^i q_i - M_t & 0 & 0 \\ 0 & 0 & \gamma^\nu K_\nu^+ - \frac{1}{2}\gamma_5\gamma^i q_i - M_t & 0 \\ 0 & 0 & 0 & \gamma^\nu K_\nu^- - \frac{1}{2}\gamma_5\gamma^i q_i - M_t \end{array}\right], \tag{4.1.30}$$

$$B = -C = \left[\begin{array}{cccc} 0 & 0 & 0 & -i\gamma_5\Delta^* \\ 0 & 0 & -i\gamma_5\Delta & 0 \\ 0 & i\gamma_5\Delta^* & 0 & 0 \\ i\gamma_5\Delta & 0 & 0 & 0 \end{array}\right]. \tag{4.1.31}$$

With the help of known identity

$$\left[\begin{array}{cc} A & B \\ C & D \end{array}\right]^{-1} = \left[\begin{array}{cc} (A - B\,D^{-1}C)^{-1} & (C - DB^{-1}A)^{-1} \\ (B - A\,C^{-1}D)^{-1} & (D - CA^{-1}B)^{-1} \end{array}\right], \tag{4.1.32}$$

and after doing similar calculations also for the block-diagonal part of S_0^{-1} that does not depend on Δ, we finally obtain the result for diagonal elements of the operator S_0 in the momentum-frequency basis

$$\begin{aligned} S_{0_{\vartheta\beta\xi}} &= \gamma^0\left((\delta_2^\beta\delta_1^{3-\beta} + \delta_1^\beta\delta_2^{3-\beta})\,|\Delta|^2\Big(-\big(k_0 + (-1)^\xi\mu\big) + \gamma^0\left(\vec{k}\cdot\vec{\gamma} - M_t + (-1)^\vartheta\,\frac{q}{2}\gamma_5\gamma^3\right)\Big)^{-1}\right. \\ &+ \left.\big(k_0 - (-1)^\xi\mu\big) + \gamma^0\left(\vec{k}\cdot\vec{\gamma} - M_t + (-1)^\vartheta\,\frac{q}{2}\gamma_5\gamma^3\right)\right)^{-1}, \end{aligned} \tag{4.1.33}$$

where indices ϑ, ξ refere respectively to the flavor and Nambu-Gorkov space and are equal 1, 2. Index β refers to the color space and takes the values 1, 2, 3. At this stage we are prepared to perform the trace of the operator S_0 over the whole set of indices. One can calculate this trace in the eigenbasis (in Dirac space) that diagonalize the matrix

$$\gamma^0 \left(\vec{k} \cdot \vec{\gamma} - M_t \pm \frac{q}{2} \gamma_5 \gamma^3 \right) \tag{4.1.34}$$

The eigenvalues of (4.1.34) to the eigenvectors ψ_i are $\lambda_i = \pm E_\pm$ (4.1.19). In this eigenbasis calculated trace has a form

$$\begin{aligned} &\mathrm{tr}\,\{S_0\} \quad = \\ &\sum_{\vartheta,\xi=1}^{2} \sum_{\beta=1}^{3} \sum_{i=1}^{4} \psi_i^\dagger \gamma^0 \psi_i \left((\delta_2^\beta \delta_1^{3-\beta} + \delta_1^\beta \delta_2^{3-\beta}) \, |\Delta|^2 \left(-k_0 - (-1)^\xi \mu + \lambda_i \right)^{-1} + \left(k_0 - (-1)^\xi \mu + \lambda_i \right) \right)^{-1}. \end{aligned} \tag{4.1.35}$$

Finally we get the expression

$$\begin{aligned} &\mathrm{tr}\,\{S_0\} \quad = \\ &-2 \left(4\, M_t \, \frac{E_+^2 - \vec{k}^{\,2} - M_t^2 + \frac{q^2}{4}}{2(E_+^2 - E_-^2)} \right) \left[2 \left(-\frac{1}{E_+} \frac{k_0 - \mu + E_+}{(k_0 - E^\Delta_{-,+})(k_0 + E^\Delta_{-,+})} \right.\right. \\ &+ \frac{1}{E_+} \frac{k_0 - \mu - E_+}{(k_0 - E^\Delta_{+,+})(k_0 + E^\Delta_{+,+})} - \frac{1}{E_+} \frac{k_0 + \mu + E_+}{(k_0 - E^\Delta_{+,+})(k_0 + E^\Delta_{+,+})} + \frac{1}{E_+} \frac{k_0 + \mu - E_+}{(k_0 - E^\Delta_{-,+})(k_0 + E^\Delta_{-,+})} \Big) \\ &\left. + \left(-\frac{1}{E_+} \frac{1}{(k_0 - \mu - E_+)} + \frac{1}{E_+} \frac{1}{(k_0 - \mu + E_+)} - \frac{1}{E_+} \frac{1}{(k_0 + \mu - E_+)} + \frac{1}{E_+} \frac{1}{(k_0 + \mu + E_+)} \right) \right] \\ &+2 \left(4\, M_t \, \frac{E_-^2 - \vec{k}^{\,2} - M_t^2 + \frac{q^2}{4}}{2(E_+^2 - E_-^2)} \right) \left[2 \left(-\frac{1}{E_-} \frac{k_0 - \mu + E_-}{(k_0 - E^\Delta_{-,-})(k_0 + E^\Delta_{-,-})} \right.\right. \\ &+ \frac{1}{E_-} \frac{k_0 - \mu - E_-}{(k_0 - E^\Delta_{+,-})(k_0 + E^\Delta_{+,-})} - \frac{1}{E_-} \frac{k_0 + \mu + E_-}{(k_0 - E^\Delta_{+,-})(k_0 + E^\Delta_{+,-})} + \frac{1}{E_-} \frac{k_0 + \mu - E_-}{(k_0 - E^\Delta_{-,-})(k_0 + E^\Delta_{-,-})} \Big) \\ &+ \left(-\frac{1}{E_-} \frac{1}{(k_0 - \mu - E_-)} + \frac{1}{E_-} \frac{1}{(k_0 - \mu + E_-)} \right. \\ &\left.\left. - \frac{1}{E_-} \frac{1}{(k_0 + \mu - E_-)} + \frac{1}{E_-} \frac{1}{(k_0 + \mu + E_-)} \right) \right]. \end{aligned} \tag{4.1.36}$$

4.1.4 Evaluation of the Matsubara summation

At this stage we are ready to perform the sum over the Matsubara frequencies ω_n. This infinite sum can be rewritten as the contour integral. We discuss this method in an example, choosing one element from the expression (4.1.36),

$$T\sum_{n=-\infty}^{n=+\infty}\left\{-\frac{1}{E_s}\frac{1}{(k_0-\mu-E_s)}\right\}\Bigg|_{k_0=T(2n+1)\pi i}= \\ -\frac{1}{2\pi i}\left\{\int_{-i\infty+\epsilon}^{i\infty+\epsilon}\frac{-1}{E_s}\frac{1}{(k_0-\mu-E_s)}\frac{1}{e^{\beta k_0}+1}dk_0+\int_{i\infty-\epsilon}^{-i\infty-\epsilon}\frac{-1}{E_s}\frac{1}{(k_0-\mu-E_s)}\frac{1}{e^{\beta k_0}+1}dk_0\right\}. \tag{4.1.37}$$

The integration contour is presented in Fig.4.1 (left panel), inside this contour, the singular points are exactly at $k_0 = T(2n+1)\pi i$. Next, in order to evaluate the two integrals on

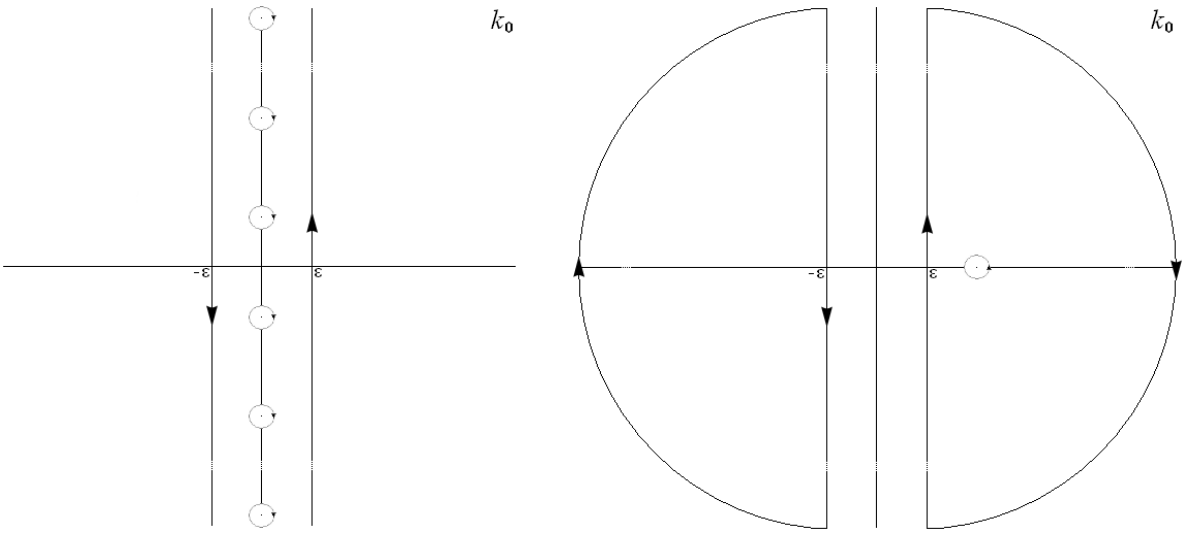

Figure 4.1: Integration contours, in the complex plane, that are needed to evaluate expression (4.1.37). The direction of integration and positions of singular points are shown schematically.

the right hand side of the equation (4.1.37) the integration contours are chosed such as it is presented in the right panel of Fig.4.1. The integral on the right semi circle vanishes, while integral on the left semi circle gives the result $-1/2E_s$. Finally, the sum (4.1.37) is

$$T\sum_{n=-\infty}^{n=+\infty}\left\{-\frac{1}{E_s}\frac{1}{(k_0-\mu-E_s)}\right\}\Bigg|_{k_0=T(2n+1)\pi i}= \\ -\frac{1}{E_s}\frac{1}{(e^{\beta(E_s+\mu)}+1)}+\frac{1}{2E_s}=\frac{1}{E_s}\frac{1}{(e^{-\beta(E_s+\mu)}+1)}-\frac{1}{2E_s}\,. \tag{4.1.38}$$

The next observation is that elements of the $\mathrm{tr}\,\{S_0\}$ can be grouped in pairs, one term for particles and one for antiparticles. This leads to the cancelation of terms proportional to $1/E_s$

$$T\sum_{n=-\infty}^{n=+\infty}\left\{-\frac{1}{E_s}\frac{1}{(k_0-\mu-E_s)}+\frac{1}{E_s}\frac{1}{(k_0+\mu+E_s)}\right\}\Bigg|_{k_0=T(2n+1)\pi i}=\frac{2}{E_s}\,\frac{1}{(e^{-\beta(E_s+\mu)}+1)}\,. \tag{4.1.39}$$

Finally, the subsequent elements of tha Matsubara sum (4.1.36) have the forms:

$$\begin{aligned}&T\sum_{n=-\infty}^{n=+\infty}\sum_{s=\pm}2\left(2\,M_t\,\frac{E_s^2-\vec{k}^{\,2}-M_t^2+\frac{q^2}{4}}{(E_+^2-E_-^2)}\right)(-s)\left\{-\frac{1}{E_s}\frac{1}{(k_0-\mu-E_s)}+\frac{1}{E_s}\frac{1}{(k_0+\mu+E_s)}\right\}\Bigg|_{k_0=T(2n+1)\pi i}\\&=2\sum_{s=\pm}\left(2\,M_t\,\frac{E_s^2-\vec{k}^{\,2}-M_t^2+\frac{q^2}{4}}{E_s\,(E_+^2-E_-^2)}\right)(-s)\,\frac{2}{(e^{-\beta(E_s+\mu)}+1)}\,,\end{aligned} \tag{4.1.40}$$

$$\begin{aligned}&T\sum_{n=-\infty}^{n=+\infty}\sum_{s=\pm}2\left(2\,M_t\,\frac{E_s^2-\vec{k}^{\,2}-M_t^2+\frac{q^2}{4}}{(E_+^2-E_-^2)}\right)(-s)\left\{\frac{1}{E_s}\frac{1}{(k_0-\mu+E_s)}-\frac{1}{E_s}\frac{1}{(k_0+\mu-E_s)}\right\}\Bigg|_{k_0=T(2n+1)\pi i}\\&=-2\sum_{s=\pm}\left(2\,M_t\,\frac{E_s^2-\vec{k}^{\,2}-M_t^2+\frac{q^2}{4}}{E_s\,(E_+^2-E_-^2)}\right)(-s)\,\frac{2}{(e^{\beta(E_s-\mu)}+1)}\,,\end{aligned} \tag{4.1.41}$$

$$\begin{aligned}&T\sum_{n=-\infty}^{n=+\infty}\sum_{s=\pm}4\left(2\,M_t\,\frac{E_s^2-\vec{k}^{\,2}-M_t^2+\frac{q^2}{4}}{(E_+^2-E_-^2)}\right)(-s)\Bigg\{\frac{1}{E_s}\frac{k_0-\mu-E_s}{(k_0-E^{\Delta}_{+,s})(k_0+E^{\Delta}_{+,s})}\\&\qquad-\frac{1}{E_s}\frac{k_0+\mu+E_s}{(k_0-E^{\Delta}_{+,s})(k_0+E^{\Delta}_{+,s})}\Bigg\}\Bigg|_{k_0=T(2n+1)\pi i}\\&=4\sum_{s=\pm}\Bigg[\left(2\,M_t\,\frac{E_s^2-\vec{k}^{\,2}-M_t^2+\frac{q^2}{4}}{E_s\,(E_+^2-E_-^2)}\,\frac{(E^{\Delta}_{+,s}+\mu+E_s)}{2E^{\Delta}_{+,s}}\right)(-s)\,\frac{2}{(e^{-\beta E^{\Delta}_{+,s}}+1)}\\&\qquad+\left(2\,M_t\,\frac{E_s^2-\vec{k}^{\,2}-M_t^2+\frac{q^2}{4}}{E_s\,(E_+^2-E_-^2)}\,\frac{(E^{\Delta}_{+,s}-\mu-E_s)}{2E^{\Delta}_{+,s}}\right)(-s)\,\frac{2}{(e^{\beta E^{\Delta}_{+,s}}+1)}\Bigg],\end{aligned} \tag{4.1.42}$$

$$
\begin{aligned}
T\sum_{n=-\infty}^{n=+\infty}\sum_{s=\pm} 4\left(2\,M_t\,\frac{E_s^2-\vec{k}^{\,2}-M_t^2+\frac{q^2}{4}}{(E_+^2-E_-^2)}\right)(-s)\Big\{-\frac{1}{E_s}\frac{k_0-\mu+E_s}{(k_0-E^{\Delta}_{-,s})(k_0+E^{\Delta}_{-,s})} \\
+\quad\frac{1}{E_s}\frac{k_0+\mu-E_s}{(k_0-E^{\Delta}_{-,s})(k_0+E^{\Delta}_{-,s})}\Big\}\Big|_{k_0=T(2n+1)\pi i} \\
=-4\sum_{s=\pm}\Bigg[\left(2\,M_t\,\frac{E_s^2-\vec{k}^{\,2}-M_t^2+\frac{q^2}{4}}{E_s\,(E_+^2-E_-^2)}\,\frac{(E^{\Delta}_{-,s}-\mu+E_s)}{2E^{\Delta}_{-,s}}\right)(-s)\,\frac{2}{(e^{\beta E^{\Delta}_{-,s}}+1)} \\
+\left(2\,M_t\,\frac{E_s^2-\vec{k}^{\,2}-M_t^2+\frac{q^2}{4}}{E_s\,(E_+^2-E_-^2)}\,\frac{(E^{\Delta}_{-,s}+\mu-E_s)}{2E^{\Delta}_{-,s}}\right)(-s)\,\frac{2}{(e^{-\beta E^{\Delta}_{-,s}}+1)}\Bigg].
\end{aligned}
\tag{4.1.43}
$$

With the help of auxiliary formulas

$$
2\,M_t\,(-s)\,\frac{E_s^2-\vec{k}^{\,2}-M_t^2+\frac{q^2}{4}}{E_s(E_+^2-E_-^2)}=-\frac{\partial E_s}{\partial M_t}\,,
\tag{4.1.44}
$$

$$
2\,M_t\,(-s)\,\frac{E_s^2-\vec{k}^{\,2}-M_t^2+\frac{q^2}{4}}{E_s\,(E_+^2-E_-^2)}\,\frac{(E^{\Delta}_{\pm,s}\pm\mu+E_s)}{2E^{\Delta}_{\pm,s}}=-\frac{1}{2}\frac{\partial E_s}{\partial M_t}-\frac{1}{2}\frac{\partial E^{\Delta}_{\pm,s}}{\partial M_t}\,,
\tag{4.1.45}
$$

$$
2\,M_t\,(-s)\,\frac{E_s^2-\vec{k}^{\,2}-M_t^2+\frac{q^2}{4}}{E_s\,(E_+^2-E_-^2)}\,\frac{(E^{\Delta}_{\pm,s}\mp\mu-E_s)}{2E^{\Delta}_{\pm,s}}=-\frac{1}{2}\frac{\partial E_s}{\partial M_t}+\frac{1}{2}\frac{\partial E^{\Delta}_{\pm,s}}{\partial M_t}\,,
\tag{4.1.46}
$$

we finally obtain the simplified result for the $\delta\Omega$ (4.1.25).

4.2 Regularization procedure

The Nambu Jona-Lasinio model is a nonrenormalizable theory and in the previous chapter the dependence on regularization scheme was discussed. The most evident quantitative differences of the results are between the 3d cut-off and Schwinger regularizations. Consequently, for the presentation of results of the present chapter we decided to choose these two schemes.

4.2.1 Regularization of the Ω_0

The temperature dependent part of the Ω_0 (4.1.18) is finite, but the zero temperature limit of the potential Ω_0 contains divergent terms. Ω_0 can be rewritten in a more convenient form, where only the last two integrals are divergent. Consequently, regularization of the thermodynamic potential Ω_0 proceeds exactly as was described in the section (3.1).

4.2.2 Regularization of the $\delta\Omega$

The infinite contribution to the $\delta\Omega$ (4.1.25) comes from the following terms

$$\sum_{s=\pm}\int\frac{d^3k}{(2\pi)^3}\left[-\frac{1}{2}\left(\frac{\partial(E_s+E^{\Delta}_{+,s})}{\partial M_t}\right)\left(1+\exp\left\{-\beta E^{\Delta}_{+,s}\right\}\right)^{-1}\right.$$
$$\left.+\frac{1}{2}\left(\frac{\partial(E_s-E^{\Delta}_{-,s})}{\partial M_t}\right)\left(1+\exp\left\{-\beta E^{\Delta}_{-,s}\right\}\right)^{-1}\right], \tag{4.2.1}$$

and

$$\sum_{s=\pm}\int\frac{d^3k}{(2\pi)^3}\left[-\left(\frac{\partial E_s}{\partial M_t}\right)\left(1+\exp\left\{-\beta(E_s+\mu)\right\}\right)^{-1}\right]. \tag{4.2.2}$$

- **3d cut-off regularization**
  We regularize divergent integrals by introducing a three dimensional momentum cut-off Λ, ($\vec{k}^{\,2}\leq\Lambda$). We must notice that the integration limit is kept equal Λ also in the finite, temperature dependent part of the potential Ω_0 (4.1.18). Adoption of this convenction is not without the influence on the results.

- **Schwinger proper time regularization**
  This method is more subtle [26]. The infinite terms contain factors of a type $(1+\exp\left\{-\beta E^{\Delta}_{\pm,s}\right\})^{-1}$. With the momentum tending to infinity, above mentioned factors tends to 1. That is why, the simple method to deal with above divergences is to add and substract the same infinite integral, which finally is regularized within the Schwinger scheme. Using this method, integral (4.2.2) can be rearranged into

$$\sum_{s=\pm}\int\frac{d^3k}{(2\pi)^3}\left[-\left(\frac{\partial E_s}{\partial M_t}\right)\left(\left(1+\exp\left\{-\beta(E_s+\mu)\right\}\right)^{-1}-1\right)\right]$$
$$+\sum_{s=\pm}\int\frac{d^3k}{(2\pi)^3}\left[-\left(\frac{\partial E_s}{\partial M_t}\right)\right]. \tag{4.2.3}$$

The first integral of equation (4.2.3) is finite, while the last one can be regularized within the Schwinger scheme

$$\sum_{s=\pm}\int\frac{d^3k}{(2\pi)^3}\left[-\left(\frac{\partial E_s}{\partial M_t}\right)\right]=-\sum_{s=\pm}\frac{\partial}{\partial M_t}\int\frac{d^3k}{(2\pi)^3}\,E_s\,. \tag{4.2.4}$$

With the help of results of the previous chapter (3.1.1.3) we get

$$-\sum_{s=\pm}\frac{\partial}{\partial M_t}\int\frac{d^3k}{(2\pi)^3}\,E_s=\sum_{s=\pm}\frac{\partial}{\partial M_t}\int\frac{d^4k_E}{(2\pi)^4}\int_{1/\Lambda^2}^{\infty}\frac{d\tau}{\tau}\left\{\exp\left[-\tau(k_4^2+E_s^2)\right]\right\}. \quad (4.2.5)$$

Integral (4.2.1) can be rewritten in a similar manner as integral (4.2.2), however, there is a subtle point about this procedure. At first, we transform the upper line of the equation (4.2.1) into

$$\sum_{s=\pm}\int\frac{d^3k}{(2\pi)^3}\left[-\frac{1}{2}\left(\frac{\partial(E_s+E^{\Delta}_{+,s})}{\partial M_t}\right)\left(\left(1+\exp\left\{-\beta E^{\Delta}_{+,s}\right\}\right)^{-1}-1\right)-\frac{1}{2}\left(\frac{\partial(E_s+E^{\Delta}_{+,s})}{\partial M_t}\right)\right]. \quad (4.2.6)$$

However, in the limit $\Delta\to 0$, the grand thermodynamic potential (4.1.25) must transforms into the potential calculated for $\Delta = 0$. This may sounds trivially, but in fact, due to the regularization scheme, it is not so obvious (aforementioned problem is not present in the 3d cut-off scheme, where all integrals are treated equally by a cut-off Λ). In order to fulfill the above condition we added and substracted the same term (last term in the lower line of equation 4.2.7).

$$\begin{aligned}&\sum_{s=\pm}\int\frac{d^3k}{(2\pi)^3}\left[-\frac{1}{2}\left(\frac{\partial(E_s+E^{\Delta}_{+,s})}{\partial M_t}\right)\left(\left(1+\exp\left\{-\beta E^{\Delta}_{+,s}\right\}\right)^{-1}-1\right)\right.\\&\left.-\frac{1}{2}\left(\frac{\partial\left(E_s+E^{\Delta}_{+,s}-2E_s-|\Delta|\frac{\partial E^{\Delta}_{+,s}}{\partial|\Delta|}\right)}{\partial M_t}\right)-\frac{1}{2}\left(\frac{\partial\left(2E_s+|\Delta|\frac{\partial E^{\Delta}_{+,s}}{\partial|\Delta|}\right)}{\partial M_t}\right)\right].\end{aligned} \quad (4.2.7)$$

Now, only the last integral is infinite, while two others are finite. With the help of results of the previous chapter (3.1.1.3) we get

$$\begin{aligned}&-\frac{1}{2}\sum_{s=\pm}\int\frac{d^3k}{(2\pi)^3}\frac{\partial\left(2E_s+|\Delta|\frac{\partial E^{\Delta}_{+,s}}{\partial|\Delta|}\right)}{\partial M_t}=-\frac{1}{2}\frac{\partial}{\partial M_t}\sum_{s=\pm}\int\frac{d^3k}{(2\pi)^3}\left(2E_s+|\Delta|\frac{\partial E^{\Delta}_{+,s}}{\partial|\Delta|}\right)\\&=\sum_{s=\pm}\frac{\partial}{\partial M_t}\int\frac{d^4k_E}{(2\pi)^4}\int_{1/\Lambda^2}^{\infty}\frac{d\tau}{\tau}\left\{\exp\left[-\tau(k_4^2+E_s^2)\right]\right\}\\&+\sum_{s=\pm}\frac{|\Delta|}{2}\frac{\partial}{\partial M_t}\frac{\partial}{\partial|\Delta|}\int\frac{d^4k_E}{(2\pi)^4}\int_{1/\Lambda^2}^{\infty}\frac{d\tau}{\tau}\left\{\exp\left[-\tau(k_4^2+(E^{\Delta}_{+,s})^2)\right]\right\}.\end{aligned} \quad (4.2.8)$$

One can then check that, in the limit when $\Delta\to 0$, the equation (4.2.8) reproduces the

equation (4.2.5). In the same manner we rewrite the lower line of equation (4.2.1).

$$
\begin{aligned}
&\sum_{s=\pm}\int\frac{d^3k}{(2\pi)^3}\left[\frac{1}{2}\left(\frac{\partial(E_s-E^{\Delta}_{-,s})}{\partial M_t}\right)\left(\left(1+\exp\left\{-\beta E^{\Delta}_{-,s}\right\}\right)^{-1}-1\right)\right.\\
&\left.+\frac{1}{2}\left(\frac{\partial(E_s-E^{\Delta}_{-,s})}{\partial M_t}\right)\right]\\
=\;&\sum_{s=\pm}\int\frac{d^3k}{(2\pi)^3}\left[\frac{1}{2}\left(\frac{\partial(E_s-E^{\Delta}_{-,s})}{\partial M_t}\right)\left(\left(1+\exp\left\{-\beta E^{\Delta}_{-,s}\right\}\right)^{-1}-1\right)\right.\\
&\left.+\frac{1}{2}\left(\frac{\partial\left(E_s-E^{\Delta}_{-,s}+|\Delta|\frac{\partial E^{\Delta}_{-,s}}{\partial|\Delta|}\right)}{\partial M_t}\right)-\frac{1}{2}\left(\frac{\partial\left(|\Delta|\frac{\partial E^{\Delta}_{-,s}}{\partial|\Delta|}\right)}{\partial M_t}\right)\right]\\
=\;&\sum_{s=\pm}\int\frac{d^3k}{(2\pi)^3}\left[\frac{1}{2}\left(\frac{\partial(E_s-E^{\Delta}_{-,s})}{\partial M_t}\right)\left(\left(1+\exp\left\{-\beta E^{\Delta}_{-,s}\right\}\right)^{-1}-1\right)\right.\\
&\left.+\frac{1}{2}\left(\frac{\partial\left(E_s-E^{\Delta}_{-,s}+|\Delta|\frac{\partial E^{\Delta}_{-,s}}{\partial|\Delta|}\right)}{\partial M_t}\right)\right]\\
&+\sum_{s=\pm}\frac{|\Delta|}{2}\frac{\partial}{\partial M_t}\frac{\partial}{\partial|\Delta|}\int\frac{d^4k_E}{(2\pi)^4}\int_{1/\Lambda^2}^{\infty}\frac{d\tau}{\tau}\left\{\exp\left[-\tau(k_4^2+(E^{\Delta}_{-,s})^2)\right]\right\}.
\end{aligned}
\tag{4.2.9}
$$

Finally, equation (4.2.3) with (4.2.5), equation (4.2.7) with (4.2.8) and equation (4.2.9) give regularized contribution to $\delta\Omega$.

4.3 Results

The parameters of the NJL model are G, G', Λ and the bare mass m. As we shall see, the particular choice of the above mentioned parameters can have a decisive influence on the conclusions following from the NJL model. The physical quantities in the vacuum that are used to fix G, Λ and m are: $f_\pi = 93$ MeV, $m_\pi = 135$ MeV and $<\bar{u}u>=<\bar{d}d>= -(250\,\mathrm{MeV})^3$. In comparison to the chiral limit, one has to reproduce also the mass of the pion m_π. We use the Gell-Mann-Oakes-Renner formula

$$
m_\pi^2\, f_\pi^2 = \frac{m\, M_t}{2G}\,, \tag{4.3.1}
$$

which toogether with the previously introduced relationships (3.1.2) allow us to establish the NJL model parameters (Table 4.1). Newly obtained parameters differ slightly form these obtained before (Table 4.2), but this change is not meaningful for the final results of the model.

We decided to present our results for the two different sets of parameters. Because of the large uncertainty in the value of quark condensate density, it can be assumed that

$\frac{1}{2} < \bar{q}q >$ is within the range $-(250 \pm 50\,\mathrm{MeV})^3$ [42]. Consequently, cut-off Λ can be chosen arbitrarily, and only coupling G and bare mass m are fitted to reproduce the pion decay constant and the pion mass. Comparison of the results for different parameters is especially instructive in the Schwinger scheme. As was mentioned in the previous chapter, if quark condensate density is set to be $-(250\,\mathrm{MeV})^3$, the constituent quark mass M_0 in the Schwinger regularization is equal only 200 MeV. Thereby, one can try to choose parameters in a way, that M_0 takes more reasonable value, and see how this affects the results. To make the discussion clear, we define the parameters of type 1 (when the value of $< \bar{q}q >$ is taken into consideration) and of type 2 (when the value of $< \bar{q}q >$ is neglected). The fitted parameters are collected in the Tables 4.1, 4.2, where also the value of constituent quark mass in the vacuum M_0 is given.

	3d	S
Λ	0.653	1.086
$G\Lambda^2$	2.1	3.68
M_0	0.313	0.2
m	0.005	0.0049
$(-\frac{1}{2} < \bar{q}q >)^{\frac{1}{3}}$	0.25	0.25

Table 4.1: Numerical values of the regularization parameters in GeV (type 1)

	3d	S
Λ	0.619	0.635
$G\Lambda^2$	2.24	7.53
M_0	0.35	0.38
m	0.0053	0.0153
$(-\frac{1}{2} < \bar{q}q >)^{\frac{1}{3}}$	0.245	0.17

Table 4.2: Numerical values of the regularization parameters in GeV (type 2)

Our goal is to resolve whether the region of spatially inhomogeneous chiral phase occurs in the NJL model for $m \neq 0$. However, this depends also on the value of coupling constant G', which can not be related to any known physical quantity. The obvious observation is that the larger is the value of G' the lower is the value of potential Ω_{MF} at the minimum corresponding to the color superconducting phase. We set $G' = 0.5\,G$, it is a lower bound for the coupling constant G' considered among the literature [47]. Thanks to the above choice, we do not exclude the possibility of existence of the mixed NCh/2SC region (that is preferable in the chiral limit). Simultaneously, we do not favor the existence of the diquark condensate over the chiral condensate. With fixed parameters G, G', Λ and

m, the thermodynamical potential Ω_{MF} (4.1.9) is a function of $M_t, q, |\Delta|$, quark chemical potential μ and temperature T. We begin our analysis in the zero temperature limit. For a given μ and T we numerically determine the global minimum of potential Ω_{MF} with respect to the free parameters. We restrict our analysis to the region of μ, where numerically obtained mass M_t is greater than the quark current mass m.

4.3.1 3d cut-off regularization

4.3.1.1 Type 1 parameters

In Fig.4.2, dependences of M_t, q and $|\Delta|$ on μ, at $T = 0$ are shown. The spatially inhomogeneous quark phase exists. There is a global minimum corresponding to mixed phase of the nonuniform chiral condensate (NCh) and 2SC color superconductor. At zero temperature, in the interval of μ from 0.322 GeV to 0.420 GeV, its value is slightly lower than the value of local minimum corresponding to mixed phase of the 2SC superconductor and uniform chiral (Ch) phase (Fig.4.2). As one can expected [38], non-zero temperature does not favor the nonuniform condensate. Phase diagram in the μ - T plane is shown in Fig.4.3. For temperatures between 0 and 20 MeV, the interval of existence of the inhomogeneous phase is practically constant, but the region of coexistence of the NCh and 2SC phases is getting smaller with growing temperature (Figs.4.3, 4.4). Above $T = 16$ MeV, the spatially inhomogeneous quark condensate exists, but without the diquark condensate. Further with growing temperature, region in which the NCh phase is a global minimum systematically decreases.

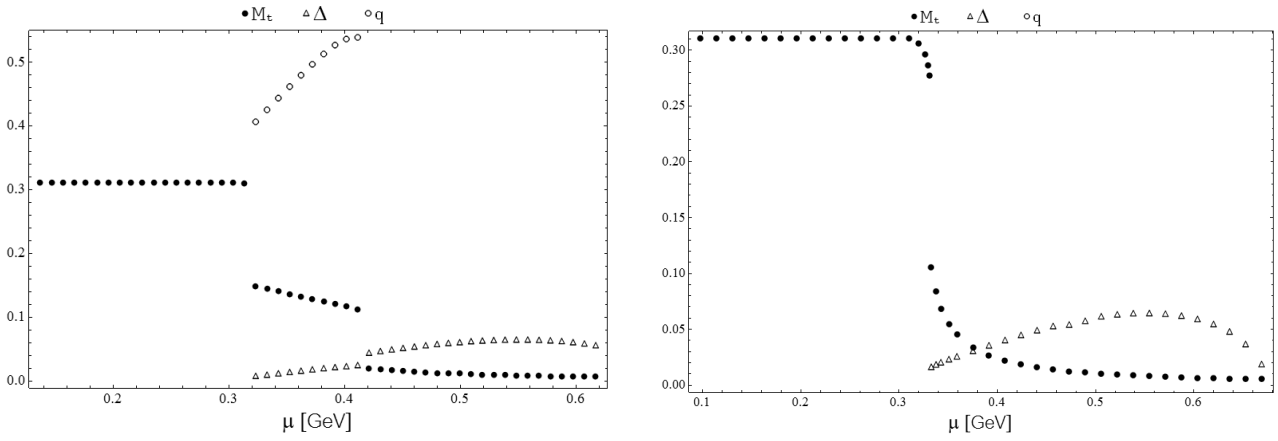

Figure 4.2: The values of M_t, q and Δ in the 3d cut-off regularization scheme for $T = 0$ (GeV units). In the left panel, the global minimum related to the mixed phase NCh/2SC is plotted. In the right panel, the local minimum related to the mixed phase Ch/2SC is plotted (type 1 parameters).

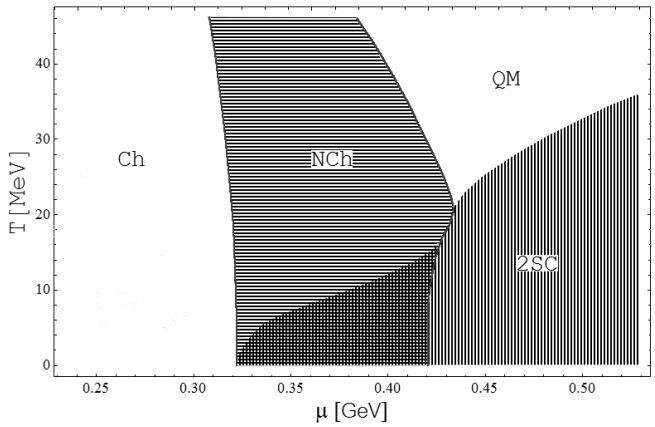

Figure 4.3: The phase diagram in the μ - T plane (3d cut-off, type 1 parameters).

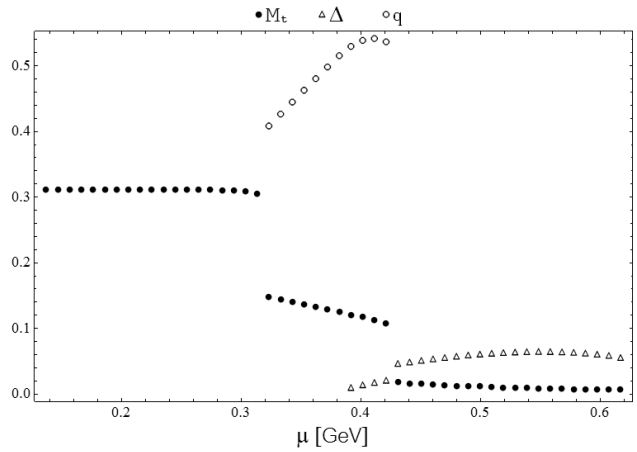

Figure 4.4: The values of M_t, q and Δ in the 3d cut-off regularization scheme for $T = 0.011$ (GeV units, type 1 parameters).

4.3.1.2 Type 2 parameters

The large uncertainty range for the quark condensate density allows us to shift the value of Λ. Moving Λ above the previous value (653 MeV) results in a decrease of the value of coupling constant G. For the lower values of G, minimum associated to the NCh phase is getting more shallow, that case will also be discussed later. Hence, we will rather reduce the value of Λ. On the other hand, Λ is an upper boundary for the energy scale, so the possible interval for the values of Λ is narrow. We set $G\Lambda^2 = 2.44$, $\Lambda = 619$ MeV, $M_0 = 350$ MeV and $m = 5.3$ MeV. With this choice of parameters, $(-\frac{1}{2} < \bar{q}q >)^{\frac{1}{3}} = 245$ MeV and it is still within the experimental range for the value of quark condensate density. Fig.4.5 presents the dependences of M_t, q and $|\Delta|$ on μ at $T = 0$. The spatially inhomogeneous quark phase exists in a region of μ from 340 to 440

MeV. In that region, the 2SC color superconducting phase coexists with the NCh phase. As one can expected, with growing T, above mentioned region is getting narrower and the value of color superconducting order parameter $|\Delta|$ is decreasing (Fig.4.6). Above $T = 20$ MeV there is no mixed region of the NCh/2SC phase.

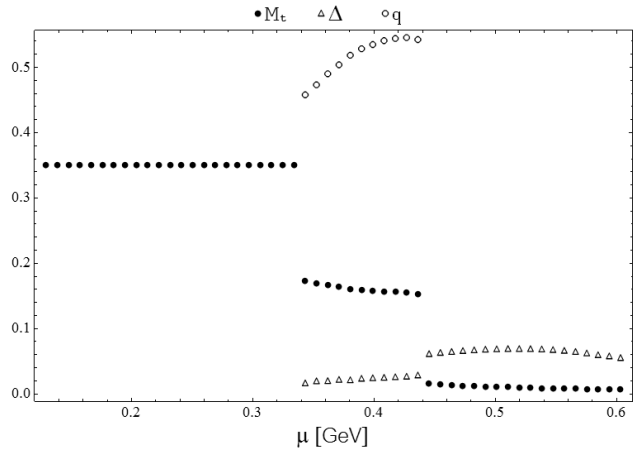

Figure 4.5: The values of M_t, q and Δ in the 3d cut-off regularization scheme for $T = 0$ (GeV units). The global minimum related to the mixed phase NCh/2SC is plotted (type 2 parameters).

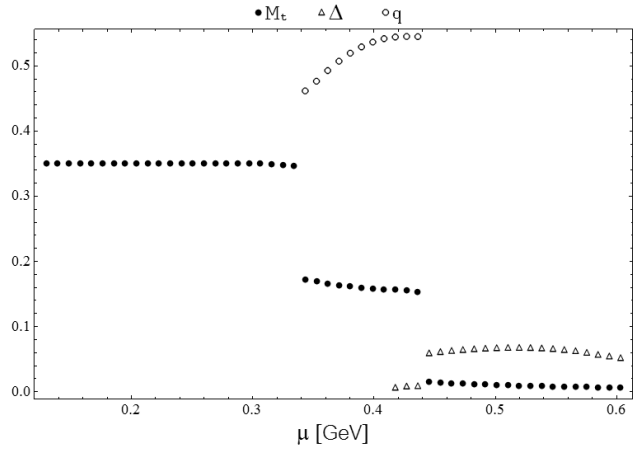

Figure 4.6: The values of M_t, q and Δ in the 3d cut-off regularization scheme for $T = 0.016$ (GeV units). The global minimum related to the nonuniform chiral solution is plotted (type 2 parameters).

4.3.2 Schwinger regularization

4.3.2.1 Type 1 parameters

In the proper time scheme at $T = 0$, the mixed phase of the NCh and 2SC phases is only a local minimum, and the values of the vector q corresponding to that local minimum are unphysical (q is considerably greater than the Λ scale). In Fig.4.7, there are presented dependences of M_t and $|\Delta|$ on μ at $T = 0$. In this regularization scheme, the values of $|\Delta|$ are of the order of magnitude smaller than in the cut-off scheme. That fact was already observed [48], we also mention on it in the previous chapter. With growing temperature, diquark condensate melts very quickly, and already for the values of temperature above 5 MeV, the color superconducting phase vanishes. But yet, the most intriguing observation is, that even at $T = 0$, we notice a smooth dependence of M_t on a chemical potential. M_t decreases from its vacuum value, across the narrow range of the rapid variability, down to the value of around 5 MeV. This is not what one can expected. The existence of the critical point in the phase diagram of the strongly interacting matter force that transition from the hadronic sector to the color superconducting region should be of the first order. Whereas, we find a smooth crossover. Above observation indicate, that NJL model within the 3d cut-off scheme reproduce the expected physics in a more reasonable manner than within the Schwinger method.

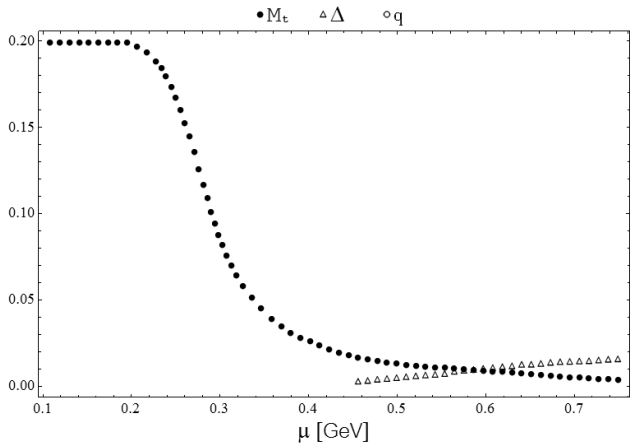

Figure 4.7: The values of M_t and Δ in the Schwinger regularization scheme for $T = 0$ (GeV units, type 1 parameters).

4.3.2.2 Type 2 parameters

The limit values of the NJL parameters for which $(-\frac{1}{2} < \bar{q}q >)^{\frac{1}{3}} > 200$ MeV are: $G\Lambda^2 = 4.58$, $\Lambda = 760$ MeV and $m = 12.6$ MeV. However, at these limit values, the spatially nonuniform chiral phase still does not exist. Guided by the findings of [45], we set $G\Lambda^2 = 7.53$, $\Lambda = 635$ MeV, $M_0 = 380$ MeV and $m = 15.3$ MeV. With this choice of

parameters, $(-\frac{1}{2} < \bar{q}q >)^{\frac{1}{3}} = 170$ MeV and it is already beyond the experimental range for the value of quark condensate density. Moreover, the current quark mass is three times greater than the expected value of order 5 MeV. As can be seen in Fig.4.8, the mixed region of the nonuniform chiral/2SC superconductor appears at $\mu = 355$ MeV. Above the value of quark chemical potential equal 450 MeV, the value of wave vector q is greater than Λ. Therefore, above these limit, discussed model is unphysical.

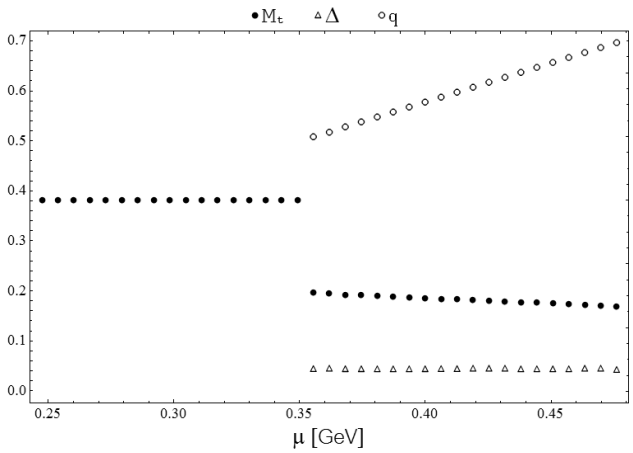

Figure 4.8: The values of M_t, q and Δ in the Schwinger regularization scheme for $T = 0$ (GeV units, type 2 parameters). $G\Lambda^2$=7.53, Λ=0.635 GeV, m=0.0153 GeV.

4.3.3 Discussion

To compare the behavior of potential Ω_{MF} (4.1.15) in different regularizations and at the different choice of parameters, we take the factor Λ^4 ahead of the Ω_{MF} and then we work with the dimensionless quantities. The $\delta\Omega$ (4.1.25) contribution to the thermodynamic potential is proportional to the ratio m/Λ. When the value of q is non-zero, $\delta\Omega$ is positive and therefore, the value of Ω_{MF} is higher than the value of Ω_0. As a consequence, $\delta\Omega$ works against the existence of the NCh phase.

One may ask a question, why so small mass m (in comparison with the other energy scales) has a significant influence on the Ω_{MF}. In the 3d cut-off scheme with the parameters of type 1 the ratio m/Λ equals 0.0076 and with type 2 $m/\Lambda = 0.0085$. Similarly in the proper time scheme, with the parameters of type 1 the ratio m/Λ equals 0.0045 and with type 2 $m/\Lambda = 0.024$. It appears, that the differences between the values of Ω_0 at the global minima corresponding to the NCh/2SC phase and the values of Ω_0 at the local minima corresponding to the uniform chiral phase are also of the order of few percent. Even so small mass m can moves the global minimum.

There is also another puzzle. Why does the inhomogeneous ground state seem to exist more likely for higher current masses (type 2 vs. type 1 parameters). Parameters of the NJL model are linked with each other. It turns, that larger m results in larger coupling constant G. With increasing G, the distance between the value of Ω_0 at global minimum

corresponding to the NCh/2SC phase and the value of Ω_0 at minimum corresponding to the uniform chiral phase increases also. Consequently, despite the growth of $\delta\Omega$ (with increasing m), the split between the minima of Ω_0 is getting more distinctive. In Fig.4.9 we compare the behavior of the values of entire potential Ω_{MF} at minima corresponding to the NCh/2SC and Ch/2SC solutions, as a function of mass m in the 3d cut-off scheme ($\mu = 360$ MeV). The vacuum value of M_0 exceeds 400 MeV when the value of current mass m is above 5.45 MeV. On the other hand, below the current mass value of around 4.7 MeV the nonuniform solution disappears.

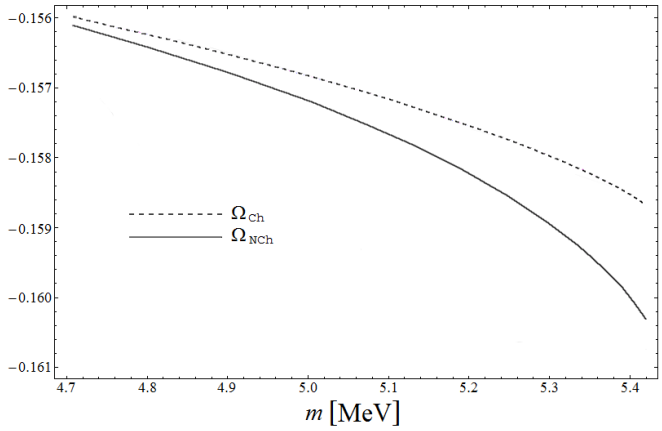

Figure 4.9: The values of Ω at minima corresponding to the NCh/2SC phase (gray line) and to the Ch/2SC phase (dashed line), as a function of mass m at $\mu = 360$ MeV (3d cut-off scheme, type 1 parameters)

4.4 Conclusions

We have shown, that the possibility of existence of the nonuniform chiral phase depends significantly on the choice of parameters and type of the regularization scheme. Our calculations indicates, that in the 3d cut-off regularization scheme, the mixed region of the NCh and 2SC phases exists for a broad set of parameters. However, in the Schwinger regularization scheme, if parameters are set to the vacuum values of f_π, m_π and $< \bar{q}q >$, then, the mixed region of the NCh and 2SC phases does not exist. In the moderate baryon density region, there is a local minimum corresponding to the NCh and 2SC phases, but the ground state is the chiral uniform phase. If we release the constrain on parameters coming from the value of $< \bar{q}q >$, then, the NCh solution might be an absolute minimum of the thermodynamical potential in the moderate baryon density region. However, with this choice of parameters, not only the $< \bar{q}q >$, but also the mass m, do not reproduce their physical values.

The result, irrespective of the choice of parameters and regularization method, is that if at some chemical potential (at $T = 0$) there is a minimum associated to the

NCh/2SC phase, its value is lower than the value of a minimum associated to the spatially inhomogeneous quark condensate with $|\Delta|$ equal to zero. Because we chose $G'= 0.5\ G$, that is a lower bound for the estimated value of the coupling G', it can be assumed, that if the NCh condensate exists at zero temperature, it exists together with the diquark condensate. With growing temperature, diquark condensate starts up at higher μ, and the region of coexistence of the NCh and 2SC phases eventually disappears.

In summary, our findings do not settle the possible existence of the spatially nonuniform chiral condensate. Both methods of regularization give different results. Nevertheless we can conclude, that within the 3d cut-off scheme, the physical quantities are easily reproduced. While, within the Schwinger scheme, there are some problems with it. Additionally, in the Schwinger scheme with parameters of type 1, transition from the chirally uniform to the color superconducting phase is a smooth crossover (at $T = 0$). This makes the Schwinger scheme results questioned.

Chapter 5

Chiral density waves in the quarkyonic matter

The issue of the fifth chapter is the analysis of the strongly interacting matter phase diagram within the Polyakov Nambu Jona-Lasinio (PNJL) model. We begin with the short introduction into the PNJL theory (5.1). To show an important sensitiveness of the PNJL model on the choice of parameters, we investigate a relationship between the critical temperatures of chiral and deconfinement transitions, both at zero quark chemical potential (5.2.2) and in the moderate density region (5.2.4). In the section (5.3) we refer to a very recent concept, namely, to the existence of the quarkyonic matter sector in the QCD phase diagram. In this context, the spatially inhomogeneous phase of the chiral density waves is discussed.

Most of the results presented in this chapter have been published in Ref. [68], some of the results can be found in Ref. [69].

5.1 Polyakov Nambu Jona-Lasinio model

In the seventies of the XX century, the model of hadrons, as being composed of more fundamental quarks and gluons, was already accepted. With this novel approach, the new perspective had been oppened. When the system evolves from the sector, where quarks and gluons are combined to form colorless hadrons, to the region where individual hadrons overlap, and quarks can move freely in the large volume, a significant change in the number of effective degrees of freedom gives a strong indication of the phase transition. In this section we focus on this so-called deconfinement transition. In the following paragraphs, we limit ourselves to the effects resulting from growing temperature. The effects due to the growing baryon density are the issue of section (5.3).

5.1.1 Polyakov loop and deconfinement transition

The primary questions, that arise when considering phase boundaries are: the question of the nature of the phase transition, and the question of the quantity, that can serves as the order parameter. In the context of QCD, the nature of deconfinement transition depends on the relation between the number of flavors N_f and the number of colors N_c. For the pure gauge SU(N_c) theory it is established, that deconfinement transition is of the second order for $N_c = 2$ [49] and of the first order for $N_c \geq 3$ [50, 51]. The free energy of the system scales as order one in the glueball sector and as order N_c^2 in the deconfined plasma. Thus, in the limit when N_c goes up to an infinity, the free energy itself can be the order parameter of the deconfinement transition. Naturally, in the physically relevant situation $N_c = 3$. However it turns out, that for the SU(3) gauge theory, there is a quantity, that vanishes in the confined phase and takes non-zero value in the deconfined sector. This is the thermal expectation value of the traced Polyakov loop

$$\langle \Phi(\vec{x}) \rangle = \langle tr_c L(\vec{x})/N_c \rangle \,, \quad L(\vec{x}) = \mathcal{P} \exp\left(i \int_0^\beta d\tau A_4(\vec{x}, \tau) \right), \tag{5.1.1}$$

where $\mathcal{P}$ is the path ordering, A_4 is the temporal component of the color gauge field in the fundamental representation and trace is taken over color indices. The traced Polyakov loop can be viewed as an creation operator for an infinitely heavy quark at position $\vec{x}$. Consequently, the thermal expectation value of the Polyakov loop is linked to the free energy (F_q) of such a quark [52]

$$\langle \Phi(\vec{x}) \rangle = \exp\left(-\beta F_q\right). \tag{5.1.2}$$

Below some critical temperature, when F_q diverges, $\langle \Phi(\vec{x}) \rangle$ is equal zero. Above this temperature, the expectation value of $\Phi(\vec{x})$ is non-zero. Because the free energy of a quark-antiquark pair separated by an infinite distance is equal $2F_q$, the free energy of a static quark is a sign of confinement [52]. One can indicate the symmetry underlying the behavior of the Polyakov loop. The pure glue SU(3) theory is invariant not only under the gauge transformations that are periodic in time, but also under the gauge transformations that are periodic up to the element of the center of SU(3) group. The existence of this non-trivial local gauge transformations is the reflection of the global $\mathbf{Z}_3$ symmetry of the euclidean Yang-Mills action (for a more detailed discussion see paragraph 5.1.1.1). On the other hand, the traced Polyakov loop transforms under aforementioned gauge symmetries as

$$\Phi(\vec{x}) \to z\Phi(\vec{x}), \tag{5.1.3}$$

where z belongs to the center of $\mathbf{Z}_3$ group. Thus, in the deconfined phase, the center symmetry is spontaneously broken.

The incorporation of quark fields as dynamical degrees of freedom significantly affects the description of the deconfinement transition. Quarks as beeing fermions, obey the anti-periodic boundary condition

$$\Psi(\vec{x},0) = -\Psi(\vec{x},\beta). \tag{5.1.4}$$

It turns, that maintenance of an anti-periodic boundary conditions is in contradiction to the local invariance under gauge transformations, that are periodic up to the element of the center of the SU(3) group. Due to the quark fields, the global $\mathbf{Z}_3$ symmetry is explicitly broken and the quark free energy (F_q) is always non-vanishing. As a consequence, the thermal expectation value of the traced Polyakov loop is no longer an exact order parameter of the deconfinemnet. We expect, that in the presence of quarks, deconfinemnet turns into a rapid crossover and that the clear definition of a critical temperature is impossible. However, according to the lattice calculations, the thermal expectation value of the traced Polyakov loop can still be useful as an effective indicator of the deconfinemnet crossover.

5.1.1.1 Z_3 center symmetry

QCD Lagrangian is invariant under local transformations $\omega(x)$ such that $\omega(x)$ is a smooth function of x and that for every x, $\omega(x) \in$ SU(3). Evaluating the QCD partition function within the finite temperature field theory formalism, we impose boundary conditions on fermion and gauge boson fields [53]

$$\begin{aligned} \Psi(\vec{x},\tau) &= -\Psi(\vec{x},\tau+\beta) \\ A_\mu(\vec{x},\tau) &= A_\mu(\vec{x},\tau+\beta). \end{aligned} \tag{5.1.5}$$

Equations (5.1.5) constrain the possible gauge transformations. Indeed, taking into account that quark and gluon fileds transform under gauge symmetries with respect to the formulas

$$\begin{aligned} &\Psi^{'}(\vec{x},\tau) = \omega(\vec{x},\tau)\Psi(\vec{x},\tau) \\ &A^{'}_\mu(\vec{x},\tau) = \omega(\vec{x},\tau)A_\mu(\vec{x},\tau)\omega^{-1}(\vec{x},\tau) + i(\partial_\mu\omega(\vec{x},\tau))\omega^{-1}(\vec{x},\tau), \end{aligned} \tag{5.1.6}$$

one can check that boundary conditions (5.1.5) are fulfilled by periodic gauge transformations $\omega(\vec{x},\tau) = \omega(\vec{x},\tau+\beta)$. However, we can consider gauge transformations that are periodic up to the center element $z \in \mathbf{Z}_3$:

$$z\,\omega(\vec{x},\tau) = \omega(\vec{x},\tau+\beta). \tag{5.1.7}$$

Periodic boundary conditions for gauge fields are still satisfied untill $z \in \mathbf{Z}_3$:

$$\begin{aligned} &A^{'}_\mu(\vec{x},\tau+\beta) = z\,(\omega(\vec{x},\tau)A_\mu(\vec{x},\tau)\omega^{-1}(\vec{x},\tau) + i(\partial_\mu\omega(\vec{x},\tau))\omega^{-1}(\vec{x},\tau))\,z^{-1} \\ &= z\,A^{'}_\mu(\vec{x},\tau)\,z^{-1} = A^{'}_\mu(\vec{x},\tau). \end{aligned} \tag{5.1.8}$$

As a result, pure gauge SU(3) Lagrangian is invariant also under this class of gauge symmetries. Because the gauge transformation law for the Wilson line $L(\vec{x})$ is

$$L^{'}(\vec{x}) = \omega(\vec{x},\beta)L(\vec{x})\omega(\vec{x},0)^{-1}, \tag{5.1.9}$$

the Polyakov loop transforms in the following way

$$\Phi^{'}(\vec{x}) = z\,\Phi(\vec{x}). \tag{5.1.10}$$

Consequently, if the value of $\Phi(\vec{x})$ is non-vanishing, global $\mathbf{Z_3}$ symmetry is spontaneously broken. Let us notice that the anti-periodic boundary conditions hold for quark fields only if $z = 1$

$$\Psi^{'}(\vec{x}, \tau + \beta) = -z\,\omega(\vec{x}, \tau)\Psi(\vec{x}, \tau) = -z\,\Psi^{'}(\vec{x}, \tau). \tag{5.1.11}$$

5.1.2 Effective Polyakov potential and lattice results

The free energy of the pure Yang-Mills SU(N_c) theory scales (in the number of colors) as the zeroth power below the critical temperature and as the second power above the deconfinement transition. It turns, that the contribution of order N_c^2 is due to the condensation of the Polyakov loop. On that basis, Pisarski suggested to write a mean field theory [54] in which the free energy in the deconfined phase is controlled by an effective potential for the Polyakov loop. This potential (so-called Polyakov potential) is formed exclusively with the Polyakov loop degrees of freedom and it mimics the thermodynamic properties of the pure gauge theory. Because the original Yang-Mills SU(3) action is invariant under global $\mathbf{Z}_3$ symmetry, the effective potential should also preserves this symmetry. Until today, some different parametrizations of the Polyakov potential have been proposed. In the present work, the two of them appear.

The chronologically first is the parametrization based on a polynomial expansion [54]:

$$\mathcal{U}(\Phi, \bar{\Phi}, T) = T^4\left(-\frac{b_2(T)}{2}\Phi\bar{\Phi} - \frac{b_3}{6}(\Phi^3 + \bar{\Phi}^3) + \frac{b_4}{4}(\Phi\bar{\Phi})^2\right), \tag{5.1.12}$$

with parameters

$$b_2(T) = 6.75 - 1.95\left(\frac{T_0}{T}\right) + 2.625\left(\frac{T_0}{T}\right)^2 - 7.44\left(\frac{T_0}{T}\right)^3, \quad b_3 = 0.75, \quad b_4 = 7.5, \tag{5.1.13}$$

where Φ and $\bar{\Phi}$ are the traced Polyakov loop and its conjugate, critical temperature parameter T_0 is equal 270 MeV.

Another form of the Polyakov potentilal is motivated by the SU(3) Haar measure and was originally presented in Ref. [55]:

$$\mathcal{U}(\Phi, \bar{\Phi}, T) = T^4\left(-\frac{1}{2}a(T)\,\bar{\Phi}\Phi + b(T)\,\ln\left[1 - 6\,\bar{\Phi}\Phi + 4\left(\bar{\Phi}^3 + \Phi^3\right) - 3\left(\bar{\Phi}\Phi\right)^2\right]\right), \tag{5.1.14}$$

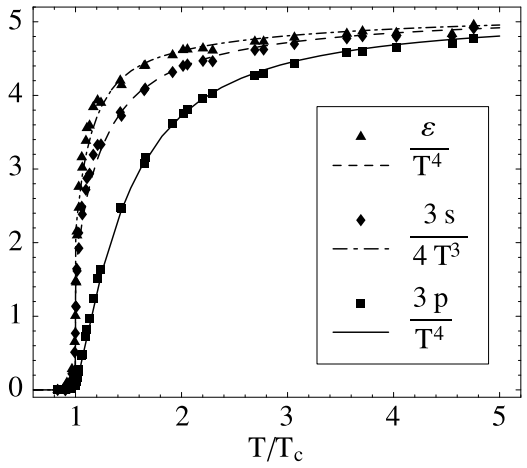

Figure 5.1: Lattice data representing scaled values of the energy density (triangles), entropy density (diamonds) and pressure (boxes) taken from Ref. [57], compared with the results of the Polyakov potential computations [56].

with parameters

$$a(T) = 3.51 - 2.47\left(\frac{T_0}{T}\right) + 15.2\left(\frac{T_0}{T}\right)^2, \quad b(T) = -1.75\left(\frac{T_0}{T}\right)^3. \tag{5.1.15}$$

Free parameters of the above potentials was deliberately fitted to reproduce the thermodynamic quantities of the SU(3) gauge theory obtained with the lattice calculations at zero baryon density. In Fig.5.1 the agreement between the results obtained with the second (logarithmic) potential (5.1.14) and the lattice results, taken from Ref. [57], is presented.

The Polyakov potential reflects also the behavior of the thermal expectation value of the traced Polyakov loop as an order parameter for the deconfinement transition. The thermal expectation value of the traced Polyakov loop is determined as a global minimum of the effective potential. With growing temperature, apart from the global minimum at $\Phi = 0$, the new minimum of the Polyakov potential appears. Above the critical temperature T_c, this new minimum becomes a global minimum and the expectation value of Φ becomes non-zero. There is a first order transition.

5.1.3 Coupling of the Polyakov loop to the quark field

It was pointed out in the previous chapters, that the phenomenon of quark confinement is missed in the NJL theory. Consequently, the moderate temperature predictions of this model are incomplete. In the present section, on the basis of the traced Polyakov loop properties, the method to extend the original NJL theory to describe both the chiral and deconfinement transitions is presented.

Thermal expectation values of the traced Polyakov loop and its conjugate are defined as

$$\langle\Phi(\vec{x})\rangle = \langle tr_c L(\vec{x})/N_c\rangle\,,\;\; \bar{\Phi}(\vec{x}) = \left\langle tr_c L(\vec{x})^\dagger/N_c\right\rangle,\;\; L(\vec{x}) = \mathcal{P}\exp\left(i\int_0^\beta d\tau A_4(\vec{x},\tau)\right). \tag{5.1.16}$$

From this moment, we work in the so-called Polyakov gauge [58]. This is a very convenient choice. In this gauge, the temporal component of the SU(3) color field $A_0 = -iA_4$ is diagonal in color space and time-independent. For the purpose of the PNJL model the simplifying assumption is that A_0 is also homogeneous in space. It follows, that the Polyakov loop takes a simple form

$$\langle\Phi\rangle = \langle tr_c L/3\rangle\,,\;\; \left\langle\bar{\Phi}\right\rangle = \left\langle tr_c L^\dagger/3\right\rangle,\;\; L = \exp\left(iA_4/T\right). \tag{5.1.17}$$

The PNJL Lagrangian is derived from the NJL type Lagrangian (in our case with two flavors and three colors). Interactions in the scalar and pseudoscalar channels are taken into account and the covariant derivative operator $D_\nu = \partial_\nu - iA_\nu(x)$, combines the quark field with the background color SU(3) gauge field $A_\nu(x)$. In the PNJL model, the only non-vanishing component of the gluon background field is its temporal (longitudinal) component, consequently transverse gluons are not contained in the PNJL theory. Because in the PNJL model, the background gluon filed is simplified, this model is expected to works up to the temperatures of order $2T_c$, above which, the transverse gluons is getting important [59]. In the present work, we concentrate on the regime of temperatures not higher than of order T_c, thus, above limitation does not alter our analysis. The PNJL Euclidean action, in the chiral limit, has a form

$$\begin{aligned}\mathcal{S} &= \int_0^\beta d\tau\int d^3x\,\Bigg[\frac{1}{2}\bar{\psi}\left(i\gamma^\nu\partial_\nu - iA_4\gamma^0 + \mu\gamma^0\right)\psi + \frac{1}{2}\bar{\psi}_c\left(i\gamma^\nu\partial_\nu + iA_4\gamma^0 - \mu\gamma^0\right)\psi_c \\ &+ G\left[(\bar{\psi}\psi)^2 + (\bar{\psi}i\gamma_5\vec{\tau}\psi)^2\right]\Bigg],\end{aligned} \tag{5.1.18}$$

where ψ is the quark field, μ is the quark chemical potential and $\psi_c = C\bar{\psi}^T$ is the charge conjugate field. The color and spinor indices are suppressed. Further calculations proceed the same as for the NJL model (chapter 4). After the Hubbard Stratanovich transformation we introduce the nonuniform ansatz. The grand thermodynamic potential in the mean field approximation can be calculated

$$\Omega_0 = -T\ln Z_{MF}. \tag{5.1.19}$$

$$\Omega_0 = \frac{M^2}{4G} - \frac{T}{2V}\ln\det{}_{D,c,NG,p}\left\{\frac{S^{-1}(i\omega_n,\vec{k})}{T}\right\}, \tag{5.1.20}$$

$$S^{-1}(i\omega_n,\vec{k}) = \left[\begin{array}{cc} \gamma^0(i\omega_n+\mu-iA_4)+\frac{1}{2}\gamma_5\tau_3 q^3\gamma^3 - M - \vec{\gamma}\cdot\vec{k} & 0 \\ 0 & \gamma^0(i\omega_n-\mu+iA_4)+\frac{1}{2}\gamma_5\tau_3 q^3\gamma^3 - M - \vec{\gamma}\cdot\vec{k}] \end{array} \right].$$

(5.1.21)

Determinant is to be taken over the Dirac, color, Nambu Gorkov and momentum-frequency spaces.

$$\begin{aligned} \Omega_0 &= \frac{M^2}{4G} - 6\sum_{s=\pm}\int\frac{d^3k}{(2\pi)^3}E_s \\ &- 2T\sum_{s=\pm}\mathrm{tr}_c\int\frac{d^3k}{(2\pi)^3}\left[\ln\left(1+L\exp^{-\frac{E_s+\mu}{T}}\right)+\ln\left(1+L^\dagger\exp^{-\frac{E_s-\mu}{T}}\right)\right], \end{aligned} \quad (5.1.22)$$

where

$$E_\pm = \sqrt{\vec{k}^2+M^2+\frac{\vec{q}^{\,2}}{4}\pm\sqrt{(\vec{q}\cdot\vec{k})^2+M^2\vec{q}^{\,2}}}\,. \quad (5.1.23)$$

Because in the Poloyakov gauge A_0 is diagonal, one can easily evaluate the above trace.

$$\begin{aligned} \Omega_0 &= \frac{M^2}{4G} - 6\sum_{s=\pm}\int\frac{d^3k}{(2\pi)^3}E_s \\ &- 2T\sum_{s=\pm}\int\frac{d^3k}{(2\pi)^3}\left[\ln\left(1+3(\Phi+\bar{\Phi}\exp^{-\frac{E_s+\mu}{T}})\exp^{-\frac{E_s+\mu}{T}}+\exp^{-3\frac{E_s+\mu}{T}}\right)\right] \\ &- 2T\sum_{s=\pm}\int\frac{d^3k}{(2\pi)^3}\left[\ln\left(1+3(\bar{\Phi}+\Phi\exp^{-\frac{E_s-\mu}{T}})\exp^{-\frac{E_s-\mu}{T}}+\exp^{-3\frac{E_s-\mu}{T}}\right)\right] \end{aligned} \quad (5.1.24)$$

Finally, the grand thermodynamic potential, expressed by the quark fileds and by the traced Polyakov loop degrees of freedom, is given as below:

$$\Omega_{PNJL} = \Omega_0 + \mathcal{U}(\Phi,\bar{\Phi},T), \quad (5.1.25)$$

where $\mathcal{U}$ is the effective Polyakov potential.

5.1.4 Comments

Individual phases are determined as a global minima of the potential Ω_{PNJL} (as a function of temperature and quark chemical potential). Fields M, q, Φ and $\bar{\Phi}$ are replaced by their expectation values $\langle M\rangle$, $\langle q\rangle$, $\langle\Phi\rangle$ and $\langle\bar{\Phi}\rangle$, taken at the minima of the Ω_{PNJL}. In principle, Φ and $\bar{\Phi}$ takes different values at the non-zero quark chemical potential. In early studies concerning PNJL model [56], Φ and $\bar{\Phi}$ were treated as independent quantities at

the minimization of the grand thermodynamic potential Ω_{PNJL}. The authors of Ref. [55] suggested, that aforementioned procedure overestimates the difference between $\langle\Phi\rangle$ and $\langle\bar{\Phi}\rangle$. The results of Ref. [60] revealed, that at the mean field level $\langle\Phi\rangle$=$\langle\bar{\Phi}\rangle$, and that the difference between them originates in the corrections to the mean filed approximation. The actual split between the expectation values of the traced Polyakov loop and its conjugate is smaller than expected and irrelevant for qualitative interpretations. That is why, for the the purpose of this work, we keep Φ equal to its conjugate $\bar{\Phi}$. The mean field equations derived form the Ω_{PNJL} are:

$$\frac{\partial\Omega_{PNJL}}{\partial M} = \frac{\partial\Omega_{PNJL}}{\partial\Phi} = \frac{\partial\Omega_{PNJL}}{\partial q} = 0. \tag{5.1.26}$$

5.2 Deconfinemnet and chiral transitions

Effective models allow us to study phenomena for which the description within the fundamental theory is much more complicated. Negative aspect of these models is that their results depend on the choice of parameters. Having above in mind, we devote this section to study the influence of the PNJL model details on the interplay between the deconfinement and chiral transitions.

5.2.1 Determination of the deconfinement and chiral transitions

5.2.1.1 Chiral transition

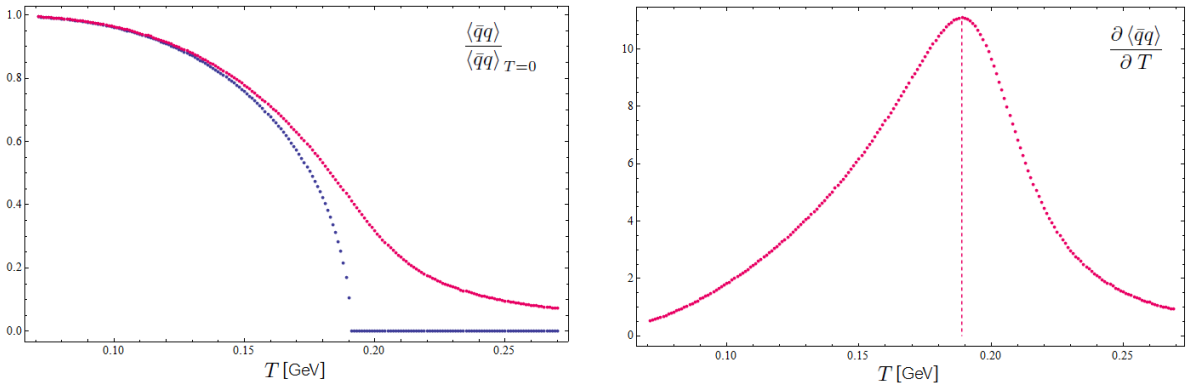

Figure 5.2: In the left panel, the value of the normalized chiral condensate is plotted as a fuction of a quark chemical potential (blue dots - $m = 0$; pink (upper) dots - $m \neq 0$). In the right panel, the value of the temperature derivative of a chiral condensate is visualized.

Primarily, we have to clarify how do we define the above mentioned transitions within the PNJL model. In general, the temperature of chiral symmetry restoration (within the

NJL model) depends on the bare qurak mass. If the bare quark mass is taken equal to zero, the chiral symmetry is an exact symmetry. The moment of the chiral transition is determined as temperature at which the value of the chiral condensate drops to zero. On the other hand, if we take the non-vanishing current quark mass, the chiral symmetry is only an approximate symmetry. The value of the chiral condensate is always nonzero. In this latter scenario, moment of the chiral transition is defined as temperature at which the derivative of the temperature dependence of the chiral condensate takes its maximum. In the left panel of Fig.5.2, the normalized chiral condensates are visualized for both $m = 0$ and $m \neq 0$ scenarios. The temperature derivative of the normalized chiral condensates is presented in the right panel of Fig.5.2. As can be seen in the following figure, the chiral transition temperature is approximately 190 MeV and coincides for both cases.

5.2.1.2 Deconfinement transition

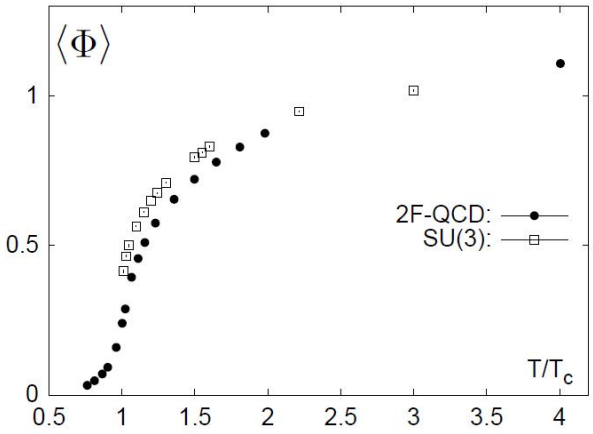

Figure 5.3: Lattice data representing the values of the traced Polyakov loop taken from Ref. [61] (solid points - two flavor QCD) and from Ref. [62] (open boxes - pure SU(3) theory).

For the pure SU(3) theory, the temperature expectation value of the traced Polyakov loop is an order parameter for deconfinement transition. At critical temperature, there is a first order transition where $\langle\Phi\rangle$ abruptly changes its value. However, in the presence of dynamical quarks, the temperature expectation value of the traced Polyakov loop behaves smoothly. Consequently, $\langle\Phi\rangle$ remains only an approximate indicator of the deconfinement crossover (see Fig. 5.3). As a consequence, the critical temperature of the deconfinement transition is defined as temperature at wchich derivative of $\langle\Phi\rangle$ takes its maximum.

5.2.2 Dependence on the model details at zero baryon density

5.2.2.1 3d cut-off regularization

Now we move to discuss the dependence of the PNJL model results with respect to the fine details of the model. It turns, that the positions of deconfinement and chiral transitions are not uniquely determined in the PNJL model. First of all, PNJL theory is a non-renormalizable theory, thereby, the regularization method must be chosen to clearly define the model. For the purpose of this study we use the 3d cut-off and the Schwinger proper time regularization schemes. All the parameters of the PNJL model are fitted to the hadronic sector, exactly as in the NJL theory. However, there is still a freedom of choice of the Polyakov loop potential. Finally, the thermodynamic potential Ω_{PNJL} (5.1.24) can be decomposed into the "vacuum" and "matter" terms. The "vacuum" contribution diverges, while the "matter" part (dependent on temperature) is finite and does not require regularization. Discussion of the NJL model in the limit $T \to \infty$ revealed that the consistent procedure is to regularize also the "matter" term [63]. Nevertheless, as one of the goals of this study is to investigate the parameter dependence of the NJL model, we examine also the case when the limit of integration in the temperature dependent term is infinity. Some studies indicate that this second approach can give a better agreement with the lattice results [64].

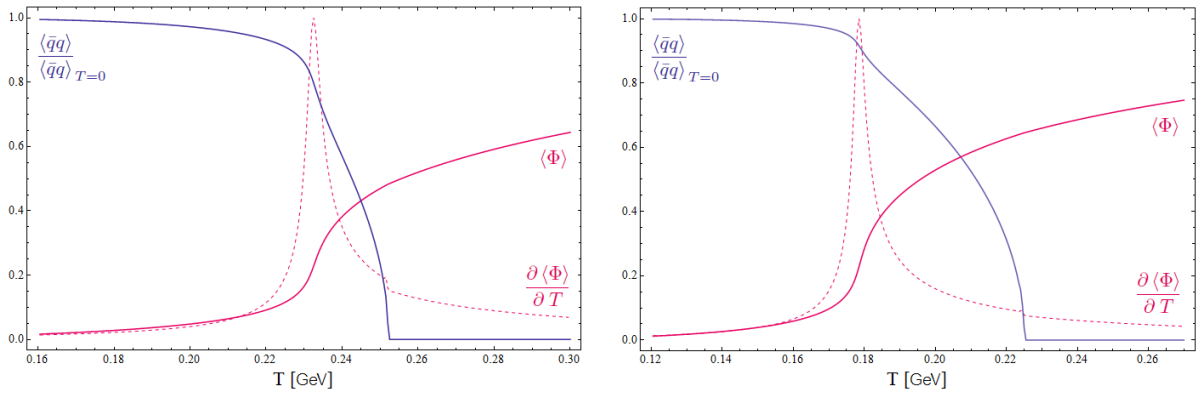

Figure 5.4: Left panel: 3d cut-off regularization, $T_0 = 270$ MeV, integration limit=Λ, logarithmic form of the Polyakov loop potential. Right panel: 3d cut-off regularization, $T_0 = 208$ MeV, integration limit=Λ, logarithmic form of the Polyakov loop potential.

The individual parametrization of the effective Polyakov loop potentials (5.1.12, 5.1.14) reproduce the lattcie data. Nevertheless, there is still an open space for the choice of the critical temperature parameter T_0. In early works, T_0 was fixed to be 270 MeV, as follows form the pure gauge theory. It turned however, that the temperature of deconfinement obtained in the PNJL model with $T_0 = 270$ MeV is much above the expected value. Color charge is screened in the presence of quark fields. Consequently, for the theory with $N_f > 0$, QCD energy scale is lower than in the pure SU(3) theory. On this basis, in

Ref.[65], the dependence of temperature T_0 on the number of flavors N_f was estimated

$$T_0 = T_\tau \exp^{-1/\alpha_0 b}, \quad \alpha_0 = 0.304, \quad T_\tau = 1.77\ GeV, \quad b = \frac{1}{6\pi}(11N_c - 2N_f). \qquad (5.2.1)$$

According to the above formula, for $N_f = 2$, $N_c = 3$ theory, $T_0 = 208$ MeV. In Fig.5.4, the outcomes of the PNJL model at $\mu = 0$, for $T_0 = 270$ MeV (left panel) and $T_0 = 208$ MeV (right panel) are presented. Due to the change of the parameter T_0, the resulting deconfinement temperature lowers from 0.23 GeV to 0.18 GeV, and the resulting chiral restoration temperature lowers from 0.25 GeV to 0.225 GeV. Consequently, the split between these temperatures broadens from 20 MeV to about 40 MeV.

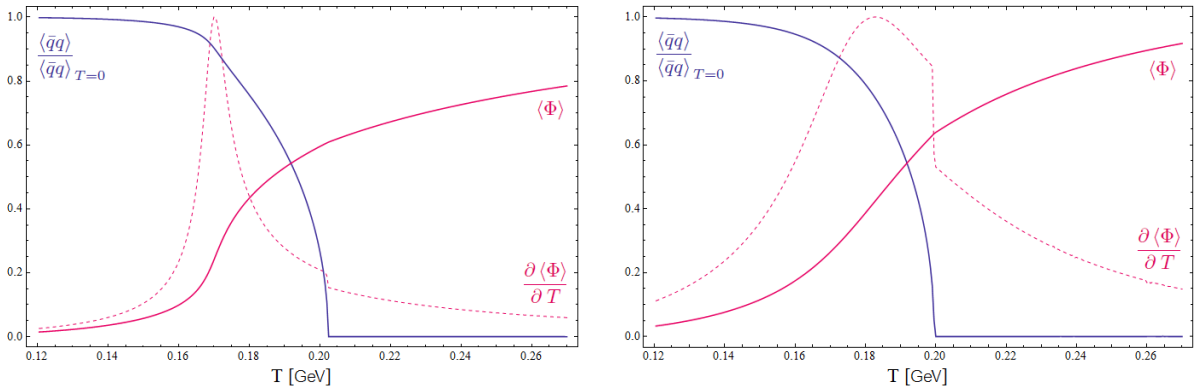

Figure 5.5: Left panel: 3d cut-off regularization, $T_0 = 208$ MeV, integration limit=∞, logarithmic form of the Polyakov loop potential. Right panel: 3d cut-off regularization, $T_0 = 208$ MeV, integration limit=∞, polynomial form of the Polyakov loop potential.

In the left panel of Fig.5.5, we present how does the change of the integration limit in the temperature dependent term of the potential Ω_{PNJL} (5.1.24) affects the PNJL model outcomes. In the comparison with the right panel of Fig.5.4, one finds that both transitions are at lower temperature, but simultaneously, they are closer to each other. This effect is understandable. The Polyakov loop variable and quark fields are coupled through the temperature dependent term of the potential Ω_{PNJL}. Because we integrate up to an infinity, this term has a greater influence on the position of a global minimum.

In the right panel of Fig.5.5, the results for the polynomial form of the Polyakov loop potential (5.1.12) are presented. Both temperatures are closer to each other than in the left panel of Fig.5.5. But yet, the maximum of the temperature dependence of $\langle\Phi\rangle$ is less clear, and the growth of $\langle\Phi\rangle$ in the region of a transition is less rapid. That is why, the definition of deconfinement transition (as a maximum of a temperature derivative of $\langle\Phi\rangle$) is more accurate for the logarithmic form of the Polyakov loop potential (5.1.14).

5.2.2.2 Schwinger regularization

In the Schwinger regularization scheme, the influence of the specific model details remains similar as for the 3d cut-off scheme. That is why we present only one diagram for this method of regularization. The exemplary dependence of the constituent mass and the traced Polyakov loop, as a function of temperature, is presented in Fig.5.6. However, if one compare Fig.5.6 with the left panel of Fig.5.5, the slight difference can be observed. In Fig.5.6 both the deconfinement and the chiral symmetry restoration transitions occur at lower temperature. Simultaneously, temperature interval between both these transitions is smaller for the Schwinger regularization. This effect is due to the fact that the Dirac sea contribution regularized with the Schwinger scheme has shallower minimum than when regularized with the 3d cut-off scheme (Fig.3.2). Consequently, chiral symmetry is restored at lower temperature.

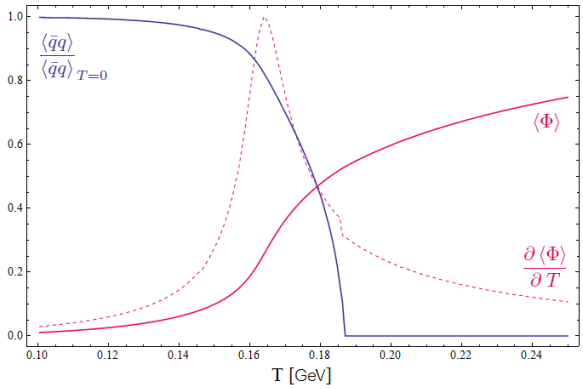

Figure 5.6: Dependences of the normalized chiral condensate and traced Polyakov loop, plotted as a fuction of temperature. Schwinger regularization, Polyakov loop potential parameter $T_0 = 208$ MeV, integration limit=∞, logarithmic form of the Polyakov loop potential.

5.2.3 Temperature dependence of coupling constant G

Theoretical relation between the phenomena of color confinement and spontaneous chiral symmetry breaking is still not sufficiently understood. Casher and Banks argument [66, 67] indicate, that at zero baryon chemical potential, color confinement automatically implies broken chiral symmetry. The PNJL model outcomes, presented in the previous subsection, are in agreement with Casher and Banks argumentation. However, QCD lattice computations [70] implies, that both transitions occur at near the same temperature, whereas, predictions based on the PNJL model indicate that both transitions are separated by the 10-30 MeV distance. The question arises, whether within the PNJL model, the agreement between the temperatures of chiral symmetry restoration and deconfinement transition can be achieved. The answer lies in the coupling constant G. It's value is usually fixed to the vacuum value. But in principle, effective coupling G is a function

of temperature and quark chemical potential. It contains contributions which follow from the integration of the gluonic degrees of freedom. At higher values of temperature, gluons interaction with quarks weakens, which in turn influences the effective four quark interaction in the same way. Thus the coupling G decreases with increasing temperature. We estimate this dependence by the Taylor expansion of G on T [68]

$$G(T) = G(1 - (T/T_c)) + G_c(T/T_c). \tag{5.2.2}$$

Empirical values of G_c and T_c result from the numerical determination of the critical temperature and depend on the choice of regularization.

- 3d cut-off regularization

$$G = 5.024\, GeV^{-2}, \quad G_c = 4.221\, GeV^{-2}, \quad T_c = 167\, MeV. \tag{5.2.3}$$

- Schwinger regularization

$$G = 3.205\, GeV^{-2}, \quad G_c = 2.985\, GeV^{-2}, \quad T_c = 167\, MeV. \tag{5.2.4}$$

With the $G(T)$ dependence on T through eq. (5.2.3), the chiral symmetry restores exactly at the critical temperature of deconfinement (Fig. 5.7). The discontinuity in the temperature derivative of $\langle\Phi\rangle$ at its maximum is due to the fact that quark bare mass is equal zero.

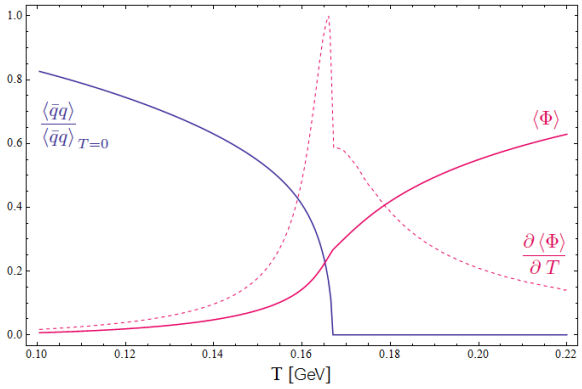

Figure 5.7: 3d cut-off regularization, $T_0 = 208$ MeV, integration limit=Λ, logarithmic form of the Polyakov loop potential, $G(T) = 5.024(1 - (T/167)) + 4.221(T/167)$ GeV^{-2}.

We can try to understand why lowering of G implies merging of both transitions. In this context, the results of the Polyakov Quark Meson (PQM) model may be instructive. The PQM model is dereived form the Quark Meson model with the full analogy to the PNJL theory. It turns, that the coincidence between discussed phase transitions is recovered in the PQM theory. Independently from any other differences, PQM and PNJL model leads to almost the same grand thermodynamic poteniatials. The difference lies

in the chiral symmetry breaking terms of the grand thermodynamic poteniatials. In the PNJL model, that is the Dirac sea contribution plus the constituent mass term (for $\vec{q} = 0$)

$$\frac{M^2}{4G} - 12 \int \frac{d^3k}{(2\pi)^3} E_0, \tag{5.2.5}$$

while in the PQM model, that is the mesonic potential

$$\frac{\lambda}{4}(\sigma^2 - \upsilon^2)^2, \; M = g\sigma. \tag{5.2.6}$$

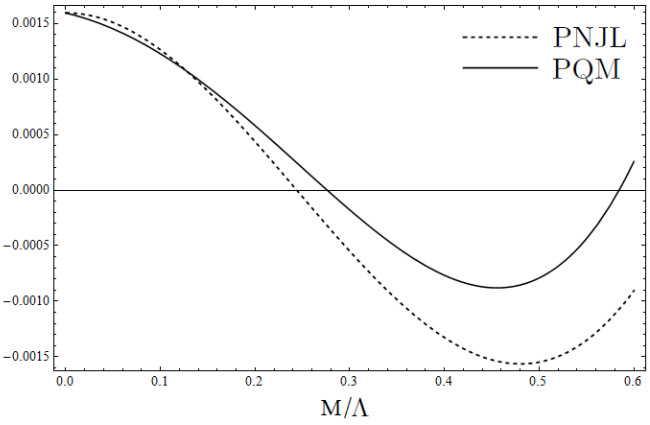

Figure 5.8: The chiral symmetry breaking term of the PNJL model (5.2.5) (in the 3d cu-off regularization) and the mesonic potential of the PQM model (5.2.6) are plotted as a function of a constituent quark mass.

In Fig. 5.8, the chiral symmetry breaking term of the PNJL model (in the 3d cu-off regularization) and the mesonic potential of the PQM model (with parameters: $g = 3.2$, $\lambda = 19.7$, $\upsilon = 87.6$ MeV) are plotted as a function of a constituent quark mass M. The crucial characteristic is the difference between the values of terms (5.2.5, 5.2.6) at their minima and at $M = 0$. This observation was made before in Ref. [40]. As can be seen in Fig.5.8, this difference is smaller for the PQM mesonic potential than for the equivalent term of the PNJL model. As a result, the temperature dependent part of the grand thermodynamic potential has a greater influence on the location of the global minimum in the PQM model. Because quarks are coupled to the Polyakov loop exactly by this temperature dependent part, coincidence between the chiral and deconfinement transitions is improved in the PQM model relative to the PNJL theory. This subtle effect can also be seen when comparing the left panel of Fig.5.5 with Fig.5.6.

Now, if we lower the value of the effective coupling G, the chiral symmetry breaking term of the PNJL model will get flatter, resembling the PQM model. Thus, the idea to assume G to be the function of temperature, that interpolates between its value G at zero temperature and its lower value G_c at critical temperature, finds its confirmation.

5.2.4 Deconfinement and chiral transitions at non-zero baryon density

Polyakov NJL model gives us the possibility to study both the chiral and deconfinement transitions. However, as one can find out in the section (5.2.2), at zero density, predictions of the PNJL theory strongly depend on the fine details of the model. The same situation persists at non-zero baryon chemical potential. At non-zero densities, apart from the all previously discussed details, there is also another effect. The question arises how does the deconfinement temperature depend on μ. According to the Casher's argument [66], deconfinement transition should always precedes the moment of chiral symmetry restoration. However, as is argued in Refs. [11, 71], this general argument does not need to be true at non-zero density. In fact, in the original PNJL model, the temperature parameter T_0 of the Polyakov loop potential (5.1.14) is constant. As a consequence, temperature of deconfinement is very slowly decreasing with growing quark chemical potential. At some μ, deconfinement transition line intersects with the chiral transition line. Such a situation is shown in the left panel of Fig.5.9.

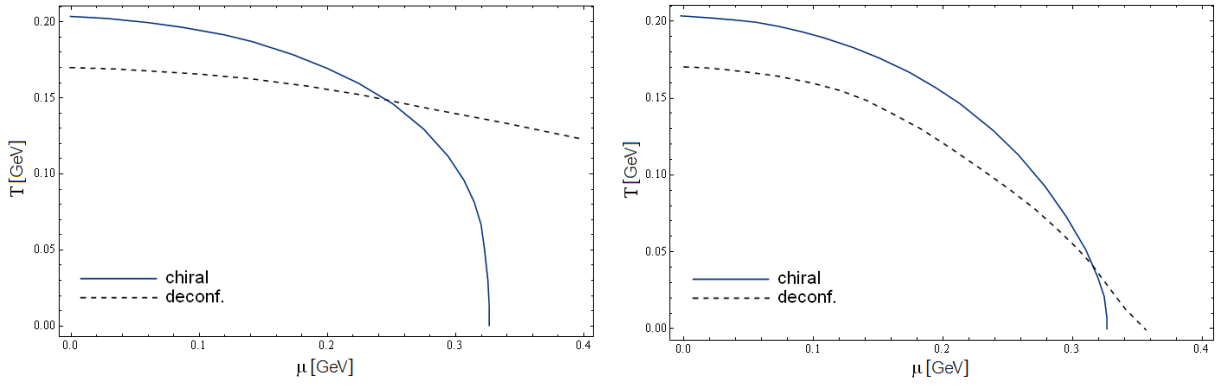

Figure 5.9: Left panel: 3d cut-off regularization, $T_0 = 208$ MeV, integration limit=∞, logarithmic form of the Polyakov loop potential. Right panel: 3d cut-off regularization, $T_0(\mu_B) = 208 \times (1 - 0.0278\left(\frac{\mu_B}{208}\right)^2)$ MeV, integration limit=∞, logarithmic form of the Polyakov loop potential.

Predictions of the PNJL model at non-zero densities can be confronted with the chemical freeze-out points (Fig.5.10). Chemical freeze-out points are obtained through the fit of the heavy-ion collision data and mark the moment when the abundances of different hadrons are already fixed. We recall that these points are not a raw experimental data and depend on the Thermal Statistical Model. Nontheless, chemical freeze-out curve in the (T, μ) plain is a practical hint for the QCD phase diagram. Various freeze-out criteria give different parametrizations of the these curve. For example, in Ref. [73] such a parametrization of the freeze-out curve has been given

$$T(\mu_B) \approx 0.17 - 0.13\mu_B^2 - 0.06\mu_B^4. \tag{5.2.7}$$

Since the Thermal Statistical Model allows us to fit the chemical freeze-out points, one

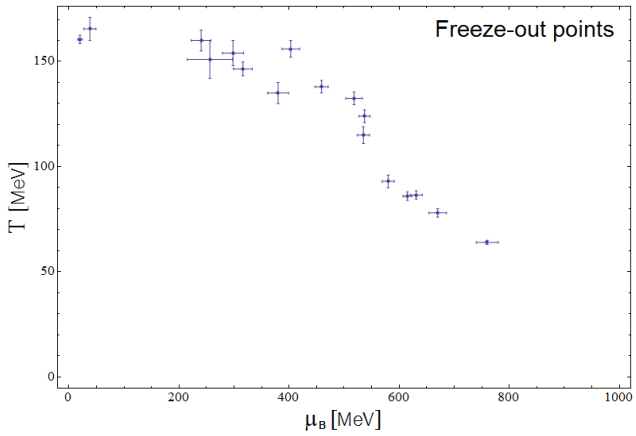

Figure 5.10: Chemical freeze-out points in the temperature - baryon chemical potential plane; experimental values taken from Ref. [74].

can use it to calculate the entropy density. Entropy is related to the number of degrees of freedon, consequently, the region in which there is a rapid growth in the entropy density, can be linked with the deconfinemnet transition. On that basis, in Ref. [75], the dependence of the Polyakov loop potential parameter T_0 on μ was estimated

$$T_0(\mu_B) = T_0 \times \left(1 - 0.0278 \left(\frac{\mu_B}{T_0} \right)^2 \right). \tag{5.2.8}$$

If the parametr T_0 is fixed to be 208 MeV, the slope of the dependence (5.2.8) is $-0.1336\mu_B^2$ and is reasonably consistent with (5.2.7). Incorporation of the formula (5.2.8) to the PNJL model leads to the significant change in the structure of the phase diagram. This is presented in the right panel of Fig.5.9. Indeed, deconfinement transition occurs at smaller temperature than chiral, and only above $\mu \approx 300$ MeV this sequence is reversed. Interestingly, simillar formula to the equations (5.2.7, 5.2.8) was introduced in Ref. [65], where argumentation based on the behaviour of the running coupling constant led to the formula

$$\begin{aligned} &T_0(\mu_B) = T_\tau \exp^{-1/\alpha_0 b(\mu)} \approx 0.208 - 0.105\mu_B^2, \\ &\alpha_0 = 0.304, \quad T_\tau = 1.77\ GeV, \quad b(\mu) = \frac{1}{6\pi}(11N_c - 2N_f) - \frac{16}{\pi} N_f \left(\frac{\mu}{T_\tau} \right)^2. \end{aligned} \tag{5.2.9}$$

It is difficult to decide which one from the two scenarios (Fig.5.9) is closer to reproduce the real physical situation. At low baryon densities, curvature of the deconfinement transition line, obtained from lattice computations, agrees with the chemical freeze-out curve. But at densities above $\mu_B \approx 400$ MeV, the chemical freeze-out points bent steeply down (Fig.5.10). Lattice computations do not settle whether the deconfinement boundary falls further with the similar curve as the freeze-out points or separates and changes slowly with growing chemical potential. Nevertheless, clear change of the slope of the chemical

freeze-out curve may indicate the presence of a new phenomenon. Such an interpretation is presented in Ref. [11]. In the large N_c limit, temperature of deconfinement is independent on μ and a new form of matter (so-called quarkyonic matter) is postulated to appear in the phase diagram of strongly interacting matter.

5.3 Chiral density waves in the context of quarkyonic matter

In this section we discuss the spatially nonuniform chiral condensate as a special realization of the quarkyonic matter. Such an approach can be adopted within the PNJL model. Before we move to the main theme, we sketch a short introduction. From this perspective, importance of the chiral density waves to the strongly interacting matter phase diagram, can be better illustrated.

5.3.1 Quarkyonic matter

Quarkyonic matter was postulated by McLerran and Pisarski in Ref. [11]. The conjectured existence of this novel form of matter is based on the QCD analysis in the so-called $'$t Hooft limit, where number of colors approaches infinity at gN_c^2 fixed [72]. At the constant number of flavors N_f, quark loops do not contribute to the Debye screening of the color potential until baryon densities reach the chemical potential of order $\sqrt{N_c}T$. This happens because the Debye mass is equal $m_D^2 = (N_c/3 + N_f/6)g^2T^2 + (N_f/(2\pi)^2)g^2\mu^2$ [11]. Thus in the large N_c limit, temperature of deconfinement transition is constant in a wide range of μ. This assumption allows us to postulate some general properties of the QCD phase diagram.

Number of effective degrees of freedom can serve as an indicator for different phases. The conjectured QCD phase diagram is usually divided into the two regions separated by the confinement-deconfinement border. These are the quark gluon plasma with $2(N_c^2-1)$ gluons plus $2N_fN_c$ quarks and hadronic matter with N_f^2-1 degrees of freedom. It turns however, that in the $'$t Hooft limit, one can distinguish one more area. This new phase is expected to exists to the right of the hadronic sector and below the deconfinement transition. Conjectured QCD phase diagarm at large N_c is presented in Fig.5.11. This implies the two consequences. Firstly, deep in the Fermi sea the dominant degrees of freedom are N_c quarks. Secondly, because of the confinement, near the edge of the Fermi surface, the baryon description is more appropriate. Hence comes the name quarkyonic matter. Summing up, quarkyonic matter is a phase with the Fermi sea of quarks and with confinement. The chiral symmetry is not involved in the above reasoning. However, it is natural that the restoration of chiral symmetry must occur somewhere inside the quarkyonic matter [71].

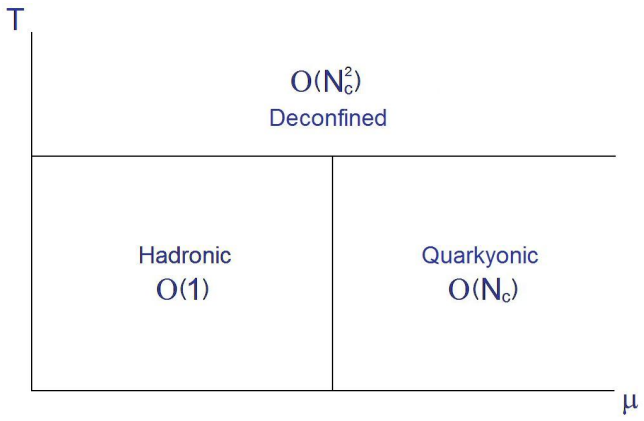

Figure 5.11: The cojectured phase diagram of QCD at large N_c; Figure based on Ref. [11].

Existence of the quarkyonic matter region in the phase diagram of the strongly interacting matter can have a direct connection with the inhomogeneous chiral phase. In the limit when number of colors goes to infinity, as was firstly shown in Ref. [23], Fermi surface is unstable against the creation of the chiral density waves (CDW) with momentum equal 2μ. However, analysis for the large, but finite N_c, proved that the region of aforementioned instability is restricted to the finite interval of baryon chemical potential [24]. Its width is narrowing with lowering N_c. For the physically relevant number of colors, another instability, leading to the color superconductivity (CSC), is more likely to occur. Above reasoning was true with the assumption that quarks form an ideal Fermi liquid. In the quarkyonic matter description, quarks persists confined, what essentially influence the Fermi surface phenomena, which are both the CDW and CSC. The estimated CDW quarkyonic gap turns to be larger then previously suggested [77]. Consequently, the inhomogeneous phase of chiral density waves is one of the possible candidate for the quarkyonic matter [78].

Presented arguments hold for the large N_c limit. That is why, any conclusions on the real QCD diagram, should be taken with a great caution. There are, however, some experimental results that might confirm such a scenario. For instance, close to the T and μ values at which the chemical freeze-out curve bends down (Fig.5.10), this is where the separation of the deconfinement and chiral transition curves is expected, the anomalies in the particle ratios was observed [79]. Experimentally measured abundances of hadrons differ from those obtained in the Statistical Thermal Model. This in turn might indicate the existence of the triple point, that is in agreement with the quarkyonic matter scenario [80]. We decided that from the above perspective, it is an interesting problem to check how the inhomogeneous phase of chiral density waves is influenced by the presence of the Polyakov loop fields [68].

5.3.2 Results and diagrams

We move to the description of the PNJL model phase diagrams in the full T - μ plane. As results from the previous sections, outcomes of the PNJL theory depend, at least quantitatively, on the specific details of the model. That is why, also in this section, we show the influence of parameters on the phase diagram. At present, one can not definitively decide, which of the presented diagrams are closer to reproduce the real QCD phase diagram. Nevertheless, we expect that these diagrams that are in agreement with the lattice results at small μ and high temperature region, should be strongly considered as a good reference at high μ and low temperature region. The important observation is that moderate baryon density part of the PNJL phase diagram is less susceptible to changes in parameters than the high temperature region. In the presentation below the Reader can gradually follow the metamorphosis of the phase diagram, starting from these rather conceptual, to these more realistic.

5.3.2.1 3d cut-off regularization

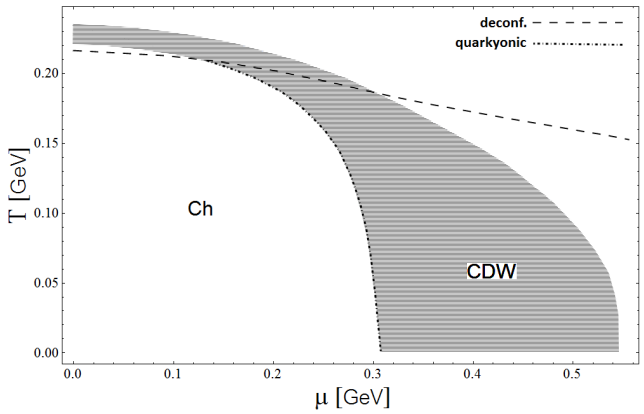

Figure 5.12: 3d cut-off regularization, $T_0 = 270$ MeV, integration limit=∞, logarithmic form of the Polyakov loop potential, constant G.

Lattice results suggest that the deconfinement and chiral transitions coincide at zero baryon density and that the above coincidence holds in the high temperature - low μ region [81]. In the PNJL model, the better agreement between mentioned transitions is achieved when integration limit, in the temperature dependent part of the grand thermodynamic potential Ω_{PNJL}, is sent to infinity (5.2.2). Now, we draw the Reader's attention to the diagram shown in Fig.5.12. If the possible existence of the spatially inhomogeneous phase is included, an unexpected result appears. The area in which the chiral density wave ansatz is favorable extends up to the zero baryon density. We do not regard above effect as physically relevant. Our results have been obtained at the mean field level and with this approximation, the thermal fluctuations are neglected. Probably, calculation

including finite temperature corrections would destroy the CDW phase at low μ region. However, it is worth mentioning, that similar effect was also observed in Refs. [40, 82].

In the PNJL model phase diagram, quarkyonic matter phase can be identified with the region below the long-dashed line (deconfinement transition) and to the right of the dotted-dashed line (this line marks the moment when quark chemical potential exceeds the value of the constituent quark mass). In this region, the baryon number density is non-zero but quarks are confined. For the large N_c limit, baryon number density grows rapidly at $\mu_B > M_B$ indicating a phase transition [83]. For $N_c = 3$ baryon number density has a discontinuity at $\mu_B = M_B$.

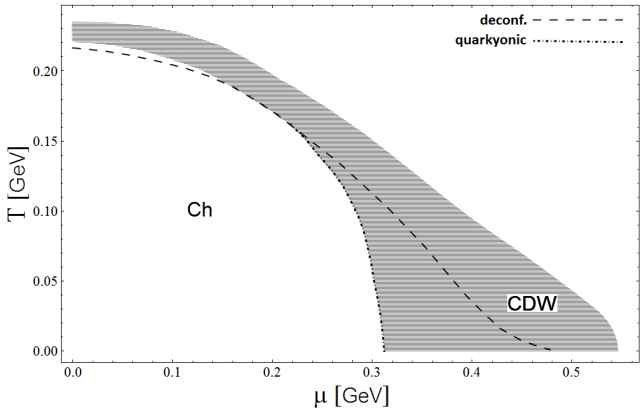

Figure 5.13: 3d cut-off regularization, $T_0 = 270$ MeV, integration limit=∞, logarithmic form of the Polyakov loop potential, constant G.

In the diagram shown in Fig.5.12, transition to the CDW phase coincides with the dotted-dashed line. The CDW phase exists in the supposed quarkyonic matter domain in a vast range of temperature and density. However, if the μ dependence of the critical temperature T_0 is introduced (5.2.4), the situation changes essentially. As one can see in Fig.5.13 restoration of the chiral symmetry always follows the deconfinement transition. Due to this fact, the existence of the supposed quarkyonic matter domain is limited to the small island in the phase diagram.

Diagrams shown in Figs.5.12 and 5.13 do not settle on the relation between the nonuniform condensate and the quarkyonic matter phase. Both of these diagrams are presented for parameter $T_0 = 270$ MeV (at $\mu = 0$). Deconfinement temperature resulting from this choice is around 220 MeV, what is above expected temperature near 170 MeV and does not coincide with the lattice simulations. We mentioned earlier (5.2.2) that for the model with two degenerate flavors the more appropriate choice is $T_0 = 208$ MeV. As it is presented in Fig.5.14, the lower value of T_0 induces the lower temperatures of the chiral and deconfinement transitions. However, the split between those two is even greater than before, and the chiral density wave domain at $\mu = 0$ is even wider (than for $T_0 = 270$ MeV). Again the CDW appear to be a possible candidate for the quarkyonic matter. But, with the above mentioned reasons, diagram shown in Fig.5.14 can not be a good candidate for the real QCD phase diagram.

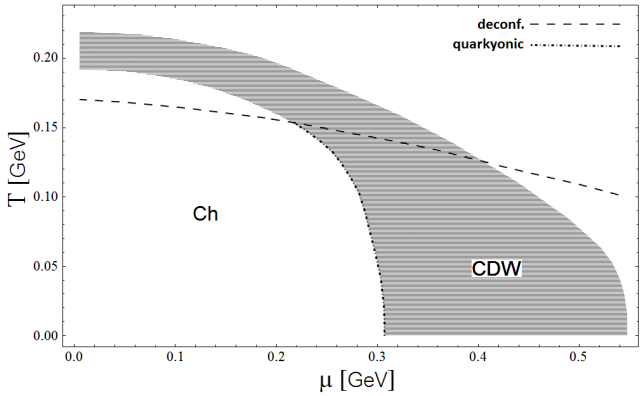

Figure 5.14: 3d cut-off regularization, $T_0 = 208$ MeV, integration limit=∞, logarithmic form of the Polyakov loop potential, constant G.

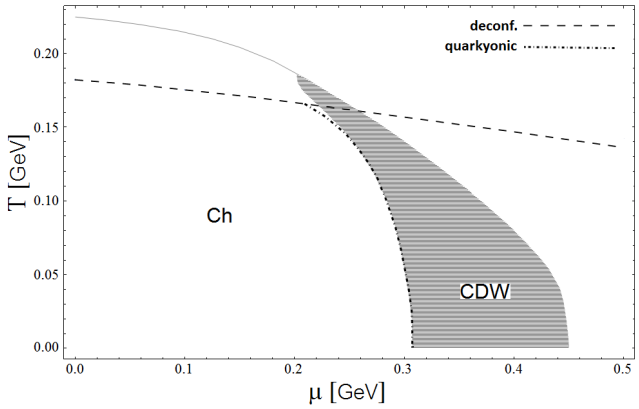

Figure 5.15: 3d cut-off regularization, $T_0 = 208$ MeV, integration limit=Λ, logarithmic form of the Polyakov loop potential, constatnt G.

As can be seen in Fig.5.14, for $T_0 = 208$ MeV, chiral and deconfinement transitions are separated and nonuniform chiral phase occurs even at zero density. If we hold the integration limit equal to the finite cut-off Λ in the all terms of the grand thermodynamic potential Ω_{PNJL} (5.1.24), the resulting phase diagram changes significantly. Such a diagram is shown in Fig.5.15. In the range of μ form 0 up to around 200 MeV, the chiral uniform sector is separated from the quark-gluon plasma by a continuous transition line. At a point (T, μ)=(186, 203) MeV, transition line divides into the two first order boarders. One divides the uniform chiral sector from the CDW region, the other divides the CDW region from the quark matter. As can be seen, the chiral uniform, inhomogeneous chiral and quark-gluon phases meet at one point. Existence of the triple point, where the hadronic, quarkyonic and quark-gluon phases meet is especially important from the quarkyonic matter scenario perspective [80]. As can be seen in Fig.5.15, the moment at which chiral transition changes its order lies surprisingly close to the point at which the quarkyonic (dotted-dashed) line crosses the deconfinement (long-dashed) line. In this

case, not only the CDW border coincides with the quarkyonic matter border, but also the quarkyonic triple point almost coincide with the point at which the Ch, the CDW and the QGP meet. It turns however, that if we consistently keep the integration limit equal Λ, the CDW area gets shrunk. At zero temperature it exists from μ equal 310 MeV up to 450 MeV.

In the all previously presented diagrams, temperatures of the chiral symmetry restoration and deconfinement transition (at zero μ) are separated. Until now we do not take ino account the dependence of the effective coupling G on temperature (5.2.2). In Fig.5.16, diagram obtained with $G(T)$ dependence is shown. In fact, at zero density, both transitions occur at the same temperature of around 167 MeV. Unfortunately, the another effect is that even though we consistently keep the integration limit equal Λ, the CDW domain reaches down to $\mu \approx 50$ MeV (see Fig. 5.16). From the other hand, the conjectured quarkyonic matter island opens already at zero baryon density, where the dotted-dashed line meets deconfinement transition line. We expect quarkyonic matter to appears at larger densities. It means that our estimation of the phase boundary between hadronic and quarkyonic matter is not meaningful at high temperature, where thermal fluctuations (neglected by us) play an important role.

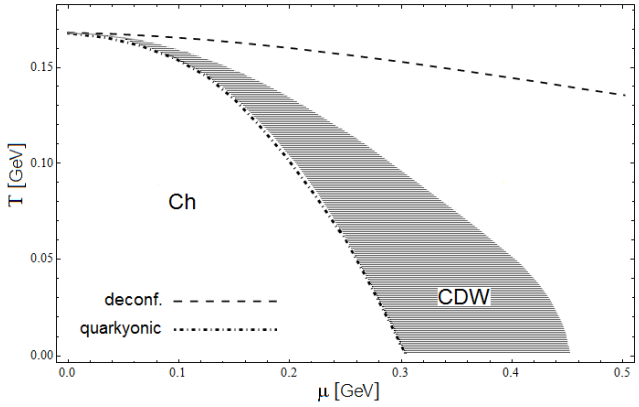

Figure 5.16: 3d cut-off regularization, $T_0 = 208$ MeV, integration limit=Λ, logarithmic form of the Polyakov loop potential, $G(T)$ dependence, CDW phase vanishes for $\mu \leq 50$ MeV

Finally, we present two diagrams that can provide a good summary of the earlier discussion. These diagrams include all the intermediate changes. The improved value of the Polyakov loop potential parameter $T_0 = 208$ (at $\mu = 0$), suggested by the freeze-out curve dependence of T_0 on μ and temperature dependence of the coupling constant G. Diagram in the left panel of Fig.5.17 is shown only for the uniform chiral phase, while diagram in the right panel of Fig.5.17 contains the nonuniform chiral condensate. Particularly important is the dependence of T_0 on μ. If deconfinement transition decreases with the relation $T_0(\mu)$, and if we consider only the chiral uniform phase, there is no space for the quarkyonic matter in the PNJL model phase diagram (left panel Fig.5.17). On the other hand, the chiral density waves open up the possibility of existence of the

quarkyonic matter (right panel Fig.5.17). Consequently, the phase of chiral density waves can be regarded as a possible realization of the quarkyonic matter.

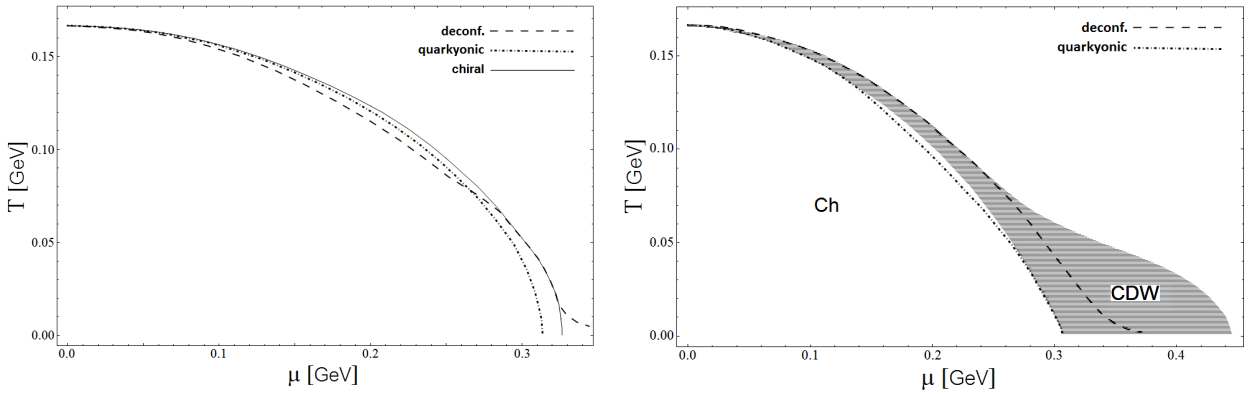

Figure 5.17: Left panel: phase diagram of the PNJL model with the homogeneous phase only. Right panel: phase diagram with the inhomogeneous chiral phase. The Polyakov loop potential parameter $T_0(\mu)$ is given by (5.2.8) with $T_0 = 208$ MeV. The finite 3-dim momentum cut-off $\Lambda = 0.653$ GeV regularized the thermodynamic potential and the NJL coupling constant $G(T)$ depends on temperature through the eq. (5.2.2).

5.3.2.2 Schwinger regularization

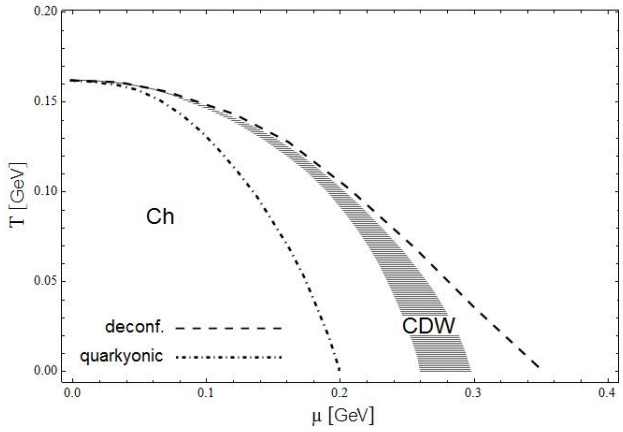

Figure 5.18: Schwinger regularization, $T_0(\mu_B) = 208\times(1-0.0278\left(\frac{\mu_B}{208}\right)^2)$ MeV, integration limit=Λ, logarithmic form of the Polyakov loop potential, $G(T) = 3.205(1 - T/162) + 2.985(T/162)$ GeV^{-2}, $\Lambda = 1086$ MeV.

Let us now apply the Schwinger regularization scheme to the analysis of the phase diagram of the PNJL model. For this scheme we do not present the Reader the subsequent stages of improvements. They follows similarly as for the 3d cut-off method. The final

diagram is presented in Fig.5.18. It incorporates both the dependence of T_0 on chemical potential and the dependence of coupling G on temperature.

The first observation is that the dotted-dashed line (this line marks the moment when quark chemical potential exceeds the value of the constituent quark mass) does not coincide with the transition line from the uniform chiral phase into the chiral density waves domain. The distance is of the order of 50 MeV (at $T = 0$). It turns, that the almost perfect coincidence between these lines within the 3d cut-off regularization, was only accidental. The moment of the appearance of the inhomogeneous phase is the consequence of the competition between the Dirac and Fermi seas contributions. The contribution due to the Dirac sea is substantially sensitive on the specific choice of the regularization scheme.

As can be seen in Fig.5.18, in the Schwinger scheme, the region of chiral density waves is much narrower than in the 3d cut-off scheme (this is in agreement with the results of chapter 3). Spatially nonuniform condensate covers only the small fragment of the conjectured quarkyonic matter region. On the other hand, the right border of the nonuniform phase is close to the deconfinement transition.

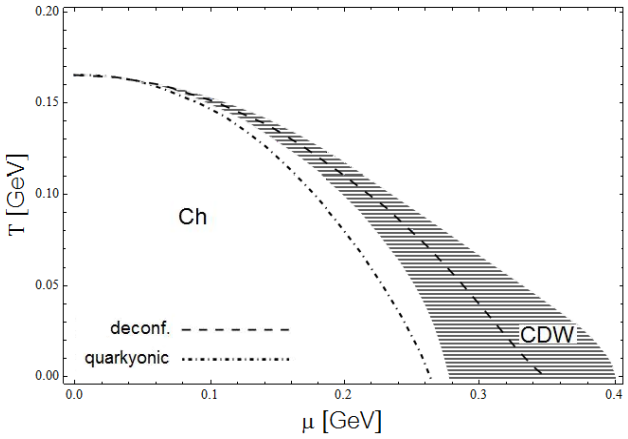

Figure 5.19: Schwinger regularization, $T_0(\mu_B) = 208\times(1-0.0278\left(\frac{\mu_B}{208}\right)^2)$ MeV, integration limit=Λ, logarithmic form of the Polyakov loop potential, $G(T) = 8.414(1 - T/165) + 6.579(T/165)$ GeV^{-2}, $\Lambda = 760$ MeV.

Here again, the question of the correct choice of the Schwinger regularization parameters appears. The parameters that we use (Table 3.1) reproduce the values of the pion decay constant and the quark condensate density. The problem is that simultaneously, the constituent quark mass at zero density is only 200 MeV. If we choose another set of parameters, for example: $\Lambda = 760$ MeV, $G\Lambda^2 = 4.85$; then the f_π value is well reproduced, quark condensate density is equal $-(200\text{ MeV})^3$ and the constituent quark mass at zero density is equal 265 MeV. Let us notice that with such parameters, the coincidence between the transition line to the CDW phase and the moment at which $\mu > M$, is almost recovered (see Fig.5.19). Moreover, the critical temperature of deconfinement at $\mu = 0$ is 165 MeV and the CDW phase reaches down to $\mu \approx 90$ MeV, what coincide with the

recent lattice estimations for the location of deconfinement transition and critical point [84, 85]. This requires further studies, but it seems that the above set of parameters is more reasonable and there is clear resemblance between the phase diagrams in the 3d cut-off and Schwinger reguarizations. The final conclusion is that the correspondence between the inhomogeneous chiral phase and the quarkyonic matter phase can be achieved in the Schwinger scheme.

5.3.2.3 Order parameters

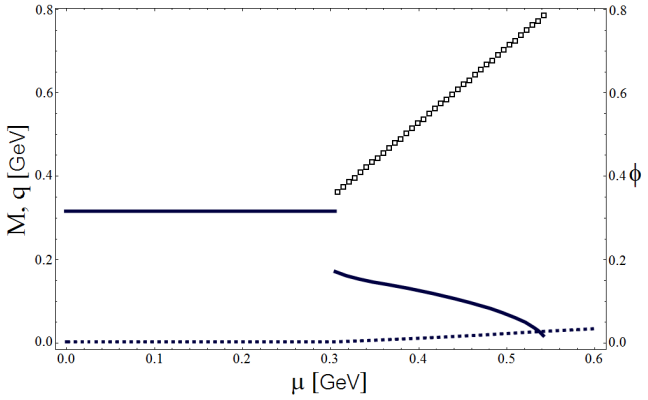

Figure 5.20: Dependence of the constituent mass M (solid line), the absolute value of vector q (open boxes) and the traced Polyakov loop Φ (dotted line) on μ, at one plot in the 3d cut-off regularization scheme. T=20 MeV, the Polyakov loop potential parameter $T_0 = 270$ MeV, integration limit=∞, logarithmic form of the Polyakov loop potential.

In the present paragraph we aim to investigate the behavior of the order parameters. The constituent quark mass M, the absolute value of wave vector q and the traced Polyakov loop Φ are examined as a function of temperature or quark chemical potential. First of all, comparing both panels of Fig.5.12, one can see that the size of the CDW area at zero temperature is independent on the behaviour of Φ. From this we can conclude that the CDW area at zero temperature is the same in the PNJL model as in the NJL model. In our opinion this is not quite obvious result. One can assume, that the value of Φ is zero at zero temperature. On the other hand, the original NJL model is reproduced from the PNJL theory if Φ is fixed to be equal one. Intuition suggests that the outcomes of these models should differ at zero temperature and draw together for growing temperature. However, it is not like that. It turns, that at zero temperature limit, temperature dependent contribution to the potential Ω_0 (5.1.24) takes the form of the Fermi sea term both for $\Phi = 0$ and $\Phi = 1$. This can be viewed as below:

$$-2T\sum_{s=\pm}\int\frac{d^3k}{(2\pi)^3}\left[\ln\left(1+\exp^{-\frac{E_s-\mu}{T}}\right)^3\right]\overset{T\to 0}{\longrightarrow}6\sum_{s=\pm}\int_{E_s\leq\mu}\frac{d^3k}{(2\pi)^3}\left(E_s-\mu\right):\quad\Phi=1,$$
$$-2T\sum_{s=\pm}\int\frac{d^3k}{(2\pi)^3}\left[\ln\left(1+\exp^{-3\frac{E_s-\mu}{T}}\right)\right]\overset{T\to 0}{\longrightarrow}6\sum_{s=\pm}\int_{E_s\leq\mu}\frac{d^3k}{(2\pi)^3}\left(E_s-\mu\right):\quad\Phi=0. \tag{5.3.1}$$

Consequently, at low temperatures, as is shown in Fig.5.20, dependences of M and q on μ resemble these obtained earlier in the NJL theory (Fig.3.1). Both transition from the uniform chiral to the nonuniform chiral, and transition from the nonuniform chiral phase to the quark matter phase are of the first order. The absolute value of the wave vector q steeply increases over the nonuniform region, while the constituent quark mass decreases gradually in the same range of μ.

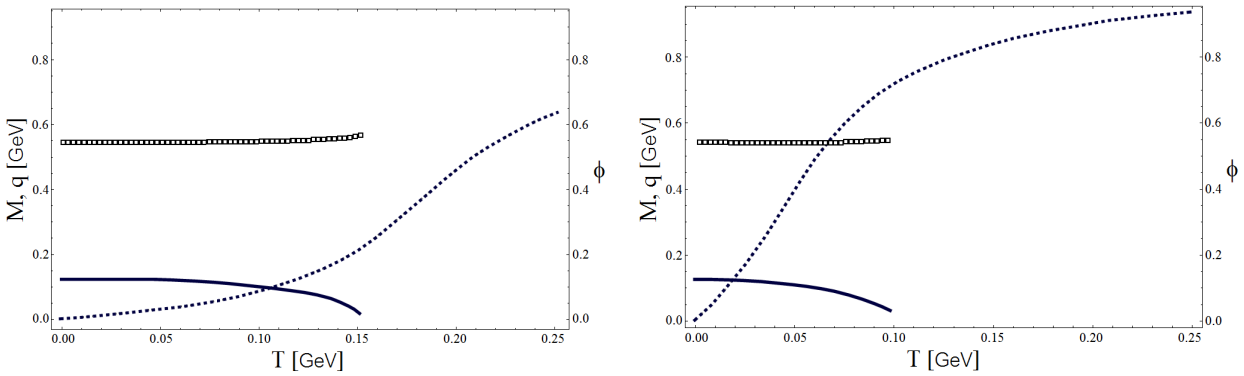

Figure 5.21: Dependence of the constituent mass M (solid line), the absolute value of wave vector q (open boxes) and the traced Polyakov loop Φ (dotted line) on T, at one plot in the 3d cut-off regularization scheme. Left panel: $\mu = 400$ MeV, Polyakov loop potential parameter $T_0 = 270$ MeV, integration limit=∞. Right panel: $\mu = 400$ MeV, $T_0(\mu_B) = 270 \times (1 - 0.0278\left(\frac{\mu_B}{270}\right)^2)$ MeV, integration limit=∞.

At higher temperatures, the influence of the value of Φ on the chiral density waves phase becomes significant. This observations is illustrated in Fig.5.21. In the left panel, the Polyakov loop potential parameter T_0 is constant and the value of the traced Polyakov loop is relatively small in a large range of temperatures. Thereby, the CDW phase reaches up to the higher temperature than in the right panel of the same figure. In the right panel of Fig.5.21 parameter T_0 depends on μ. As a result, Φ grows rapidly with temperature. Growing value of Φ affects the position of the minimum of the temperature dependent part of the thermodynamic potential Ω_0 (5.1.24). For example, the depth of the minimum corresponding to the inhomogeneous chiral phase is greater for the fixed value $\Phi = 0.1$ than for the fixed value $\Phi = 1$. At this point, predictions of the PNJL model are remarkably consistent with the general argumentation concerning the nonuniform chiral phases.

As mentioned earlier (5.3.1), instability of the Fermi surface leading to the CDW phase is more probable to occur in the confined phase (that in the PNJL model corresponds to the small values of Φ) than in the phase where quarks form an ideal Fermi liquid. To sum up, comparing the PNJL and the NJL models, there are two effects. At temperatures in the vicinity of zero, both theories give similar results. However, with growing temperature, chiral density waves are more favored by the PNJL theory. The range of this second mechanism depends intensively on the behaviour of the traced Polyakov loop. This in turn is governed by the Polyakov loop potential. For the constant parameter T_0, broadening of the inhomogeneous phase is significant. But if the parameter T_0 decreases as a function of μ, mentioned effect is only marginal.

5.4 Conclusions

We have shown that the phase of chiral density waves should be considered as a strong candidate for the quarkyonic matter. Quarkyonic matter is the phase where dominant degrees of freedom are quarks within the Fermi sea, but because of confinement, excitations above the Fermi sea are colorless baryons or mesons. The possibility of existence of quarkyonic matter is constrained by the deconfinement transition. Dependence of the temperature of deconfinement transition on baryon density can be extracted from the chemical freeze-out points (5.2.4). We recall that if this dependence is included in the Polyakov NJL model analysis, then, deconfinement and chiral transitions coincide and there is no region of the quarkyonic matter. However, if the spatially nonuniform chiral phase is taken into consideration, then, space for the quarkyonic matter in the phase diagram is opened.

We have examined the Polyakov NJL model regularized with the two different schemes. Next, guided by the QCD lattice computations, we have assumed that the effective coupling constant in the quark-quark channel interpolates between its vacuum value and its value at deconfinement transition. Final diagrams obtained in the 3d cut-off and Schwinger schemes appear to be consistent with each other (Figs.5.17, 5.19). From this follows, that at least at the mean field level, correspondence between the quarkyonic matter and the inhomogeneous phase of chiral density waves can be justified.

Chapter 6

Summary and outlook

The leading theme of this study was the spatially nonuniform chiral condensate. In contrast to the conventional quark condensate, which is the non-vanishing vacuum expectation value of the quark and antiquark fields, the nonuniform condensate is a pair of the quark and quark hole from the opposite sides of the Fermi surface. Such a pair possesses a non-zero total momentum and thus the condensate is spatially variable.

Existence of the nonuniform chiral phase is of the great importance for the phase diagram of the strongly interacting matter. Most of all, in the presence of the nonuniform phase, the chiral symmetry restores at larger baryon densities. In the zero temperature limit, critical quark chemical potential of the chiral transition is shifted by up to 100 MeV towards the growing density (e.g. Fig. 4.2).

We have studied the nonuniform condensate in the form of the so-called dual standing chiral density wave. With this ansatz, condensate undergoes periodic modulation in the scalar and pseudoscalar channels, but its amplitude is constant. The moderate baryon density region of the phase diagram, where the spatially nonuniform condensate presumably exists, is unaccessible with *ab initio* calculations. Therefore, natural question was to consider how do the fine details of the Nambu Jona-Lasinio model affect the nonuniform phase.

The first part of this work is the analysis of the NJL model at the mean field level and in the chiral limit. At zero temperature, nonuniform phase exists irrespectively to the choice of the regularization scheme. Differences between the four discussed regularization schemes are on the quantitative level. It is worth to mention that the coexistence of quark and diquark condensates is preferable in this limit.

The quarks are massive, thus it is interesting to consider the influence of the non-zero bare mass on the nonuniform condensate. In the fourth chapter we evaluate the correction to the grand thermodynamic potential due to the non-zero bare quark mas. This evaluation includes the existence of the diquark condensate. For the non-zero values of the wave vector, the correction works against the existence of the nonuniform chiral condensate. Results are presented for the two chosen methods of regularization. In the 3d cut-off scheme nonuniform phase exists, but in the Schwinger scheme, its existence depends on the choice of parameters.

The last part is the analysis of the phase diagram in the temperature - baryon density plane. Our calculations are based on the Polyakov Nambu Jona-Lasinio model that allows study of the chiral and deconfinement transitions. Motivation is to compare the inhomogeneous chiral phase scenario with the quarkyonic matter scenario, as possible candidates for the new phase of matter at moderate density. The main result is that the μ-dependence of the deconfinement temperature causes that the quarkyonic matter exists only provided the existence of the nonuniform condensate.

Summarizing, this study indicates that it is possible that the spatially nonuniform chiral condensate is the real-world phase of the strongly interacting matter. Our analysis was done at the mean field level. Thus, it would be instructive to extend this study and examine the inhomogeneous phase also beyond the mean field. But probably, low temperature predictions would not be much affected by the thermal fluctuations. Another interesting direction is to look for the different ansatz of the nonuniform chiral condensate, which could provide the ground state of lower energy. But again, dual chiral density wave ansatz is motivated by the condensed matter phenomena, like spin density waves in metals. Therefore, it is non-trivial to suggest a better ansatz. Finally, it is an open question, if one can confirm existence of the nonuniform chiral phase. Hopefully, experimental studies of the QCD phase diagram are under intensive progress, and for sure, coming years will bring us the new results.

Appendix A

Numerical calculations

Phases of the strongly interacting matter are determined by solving the mean field equations. By use of the standard Nelder - Mead algorithm [86], minima of the grand thermodynamic potential are found numerically. To gain a satisfactory control over a computational process, we decided to implement this algorithm in the *Wolfram Mathematica.* The Nelder - Mead algorithm (also known as a downhill simplex algorithm) is dedicated to finding extrema of multivariable, scalar valued functions. Because the optimization procedure does not involve the calculation of derivatives, this method is very practical. The values of the n-real variable function are calculated at $n+1$ points (which form the n-simplex in the n-dimensional space). Next, this $n+1$ values are sorted ascendingly, and then, compared with the function values calculated at some test points. In the each following step of the iteration, the vertices of the n-simplex are modified in the direction of decreasing values of a given function. The Nelder - Mead algorithm allows to determine only the local minima. Consequently, to be sure that the global minimum of a system was found, the procedure must be initiated from the different starting points - corresponding to the different phases. The basic code of the Nelder - Mead algorithm, in the case of a 3-variable function, written in the *Wolfram Mathematica*, is attached to this manuscript.

Bibliography

[1] R. Hagedorn, Suppl. Nuovo Cim. **3**, 147, (1965).

[2] M. Gell-Mann, Phys. Lett. **8**, 214, (1964).

[3] W. Broniowski, W. Florkowski and L. Ya. Glozman, Phys.Rev. **D70**, 117503, (2004).

[4] P. Castorina, K. Redlich and H. Satz, Eur.Phys.J. **C59**, 67, (2009).

[5] N. Cabibbo and G. Parisi, Phys. Lett. **B59**, 67, (1975).

[6] G. Baym, Prog. in Part. and Nucl. Phys. **8**, 73, (1982).

[7] J. Kogut, M. Stone, H.W. Wyld , W.R. Gibbs, J. Shigemitsu, S.H. Shenker and D.K. Sinclair, Phys. Rev. Lett. **50**, 393, (1983).

[8] B. C. Barrois, Nucl. Phys. **B129**, 390, (1977).

[9] M. Alford, K. Rajagopal and F. Wilczek, Nucl.Phys. **B537**, 443, (1999).

[10] R. Rapp, T. Schafer, E. V. Shuryak, and M. Velkovsky, Phys. Rev. Lett. **81**, 53, (1998).

[11] L. McLerran, R. D. Pisarski, Nucl.Phys. **A796**, 83, (2007).

[12] K. Fukushima and T. Hatsuda, Rept.Prog.Phys. **74**, 01401, (2011).

[13] P. Castorina, R. V. Gavai and H. Satz, Eur.Phys.J. **C69**, 169, (2010).

[14] S. Hands, Contemp.Phys. **42**, 209, (2001).

[15] J.M. Lattimer and M. Prakash, Science **304**, 536, (2004).

[16] J. Bardeen, L. N. Cooper and J. R. Schrieffer, Phys. Rev. **106**, 162, (1957).

[17] M. Alford, K. Rajagopal, T. Schaefer and A. Schmitt, Rev. Mod. Phys. **80**, 1455, (2008).

[18] R. E. Peierls, Quantum Theory of Solids (Oxford University Press, London, 1955).

[19] G. Grüner, Rev. Mod. Phys. **60**, 1129, (1988).

[20] A.W. Overhauser, Phys. Rev. Lett. **4**, 462, (1960).

[21] A.W. Overhauser, Phys. Rev. **128**, 1437, (1962).

[22] G. Grüner, Rev. Mod. Phys. **66**, 1, (1994).

[23] D.V. Deryagin, D.Yu. Grigoriev, and V.A. Rubakov, Int. J. Mod. Phys. **A7**, 659, (1992).

[24] E. Shuster and D. T. Son, Nucl.Phys. **B573**, 434, (2000).

[25] T. Tatsumi, Prog. Teor. Phys. **63**, 114006, (1980).

[26] E. Nakano and T. Tatsumi, Phys. Rev **D71**, 114006, (2005).

[27] E. Nakano and T. Tatsumi, arXiv:hep-ph/0408294v1 (2004).

[28] F. Dautry, E. M. Nyman, Nucl. Phys. **A319**, 323, (1979).

[29] M. Kutschera, W. Broniowski and A. Kotlorz, Phys. Lett. **B237**, 159, (1990).

[30] M. Buballa, Physics Reports **407**, 205, (2005).

[31] Y. Nambu and G. Jona-Lasinio, Phys. Rev. **122**, 345, (1961).

[32] Y. Nambu and G. Jona-Lasinio, Phys. Rev. **124**, 246, (1961).

[33] S. P. Klevansky, Rev. Mod. Phys. **64**, 649, (1992).

[34] W. Broniowski and M. Kutschera, Phys. Lett. **B242**, 133, (1990).

[35] M. Kutschera, W. Broniowski and A. Kotlorz, Nucl. Phys. **A516**, 566, (1990).

[36] T. Tatsumi, T. Maruyama, K. Nawa and E. Nakano, arXiv:hep-ph/0502201v3 (2005)

[37] D. Nickel, Phys. Rev. **D80**, 074025, (2009).

[38] M. Sadzikowski, Phys. Lett. **B642**, 238, (2006).

[39] M. Sadzikowski, Phys. Lett. **B553**, 45, (2003).

[40] M. Sadzikowski and W. Broniowski, Phys. Lett. **B488**, 63, (2000).

[41] M. Buballa and M. Oertel, Nucl. Phys. **A703**, 770, (2002).

[42] E. N. Nikolov, W. Broniowski, C. V. Christov, G. Ripka and K. Goeke, Nucl.Phys. **A608**, 411, (1996).

[43] M. Huang, P. Zhuang and W. Chao, Phys. Rev. **D65**, 076012, (2002).

[44] T. Partyka, Mod.Phys.Lett. **A26**, 543, (2011).

[45] S. Maedan, Prog. Theor. Phys. **123**, 285, (2009).

[46] S. Maedan, Prog. Theor. Phys. **118**, 729, (2007).

[47] J. Berges and K. Rajagopal, Nucl.Phys. **B538**, 215, (1999).

[48] T. Partyka and M. Sadzikowski, J. Phys. **G36**, 025004, (2009).

[49] J. Engels, J. Fingberg, M. Weber, Nucl. Phys. **B332**, 737, (1990).

[50] M. Fukugita, M. Okawa, A. Ukawa, Phys. Rev. Lett. **63**, 1768, (1989).

[51] B. Lucini, M. Teper, U. Wenger, Phys. Lett. **B545**, 197, (2002).

[52] L. McLerran, B. Svetitsky, Phys. Rev **D24**, 450, (1981).

[53] J. I. Kapusta, *Finite-Temperature Field Theory* (Cambridge University Press, Cambridge, England, 1989).

[54] R.D. Pisarski, Phys. Rev. **D62**, 034021, (2000).

[55] S. Roessner, C. Ratti and W. Weise, Phys. Rev. **D75**, 034007, (2007).

[56] C. Ratti, M. A. Thaler and W. Weise, Phys. Rev. **D73**, 014019, (2006).

[57] G. Boyd et al., Nucl. Phys. **B469**, 419, (1996).

[58] M. Quandt, H. Reinhardt and A. Schafke, Phys.Lett. **B446**, 290, (1999).

[59] P. N. Meisinger, M. C. Ogilvie and T. R. Miller, Phys. Lett. **B585**, 149, (2004).

[60] S. Roessner, T. Hell, C. Ratti, and W. Weise, Nucl.Phys. **A814**, 118, (2008).

[61] O. Kaczmarek, F. Karsch, P. Petreczky and F. Zantow,Phys. Lett. **B543**, 41, (2002).

[62] O. Kaczmarek and F. Zantow, Phys.Rev. **D71**, 114510, (2005).

[63] W. Florkowski and B.L. Friman, Acta. Phys. Pol. **B25**, 49, (1994).

[64] P. Costa, H. Hansen, M. C. Ruivo and C. A. de Sousa, Phys.Rev. **D81**, 016007, (2010).

[65] B.J. Schaefer, J. M. Pawlowski and J. Wambach, Phys.Rev. **D76**, 074023, (2007).

[66] A. Casher, Phys. Lett. **B83**, 395, (1979).

[67] T. Banks and A. Casher, Nucl. Phys. **B169**, 103, (1980).

[68] T. Partyka and M. Sadzikowski, Acta Phys. Polon. **B42**, 1305, (2011).

[69] T. Partyka, arXiv:1005.5688 (2010).

[70] F. Karsh and E. Laermann, Phys.Rev. **D50**, 6954, (1994).

[71] L. Ya. Glozman, Phys.Rev. **D80**, 037701, (2009).

[72] G. 't Hooft, Nucl. Phys. **B72**, 461, (1974).

[73] J. Cleymans, H. Oeschler, K. Redlich, S. Wheaton, Phys.Rev. **C73**, 034905, (2006).

[74] A. Andronic, P. Braun-Munzinger, J. Stachel, Nucl.Phys. **A772**, 167, (2006).

[75] K. Fukushima, arXiv:1008.4322v1 (2010).

[76] L. Ya. Glozman, arXiv:0803.1636v2 (2008).

[77] T. Kojo, Y. Hidaka, L. McLerran, R.D. Pisarski, arXiv:0912.3800v2 (2010).

[78] L. McLerran, Acta Phys. Pol. **B41**, 2799, (2010).

[79] A. Andronic and P. Braun-Munzinger, J. Stachel, Acta Phys. Pol. **B40**, 1005, (2009).

[80] A. Andronic et al., Nucl. Phys. **A837**, 65, (2010).

[81] F. Karsch and E. Laermann, Phys. Rev. **D50**, 86, (1994).

[82] D. Nickel, Phys. Rev. Lett. **103**, 072301, (2009).

[83] L. McLerran, K. Redlich, C. Sasaki, Nucl.Phys. **A824**, 86, (2009).

[84] F. Karsch, J. Phys. **G31**, 633, (2005).

[85] Z. Fodor and S.D. Katz, JHEP **404**, 50, (2004).

[86] J.A. Nelder and R. Mead, Computer Journal **7**, 308, (1965).